

An Investigation into the Detection of Seafloor Massive Sulphides  
through Sonar  
Masters Report

Michael Mitchley

December 13, 2011

# Abstract

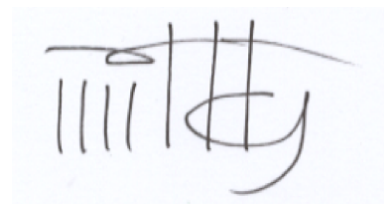
Seafloor massive sulphides are deep sea mineral deposits currently being examined as a potential mining resource. Locating these deposits, which occur at depths in the order of  $2km$ , is currently performed by expensive submersible sonar platforms as conventional sonar bathymetry products gathered by sea surface platforms do not achieve adequate spatial resolution.

This document examines the use of so-called *high resolution* beamforming methods (such as MUSIC and ESPRIT) for sonar bathymetry, together with combinations of parameter estimation techniques, including techniques for full rank covariance matrix estimation and signal enumeration. These methods are tested for bathymetric profile accuracy using simulated data, and compared to conventional bathymetric methods.

It was found that high resolution methods achieved greater bathymetric accuracy and higher resolution than conventional beamforming. These methods were also robust in the presence of unwanted persistent signals and low signal to noise ratios.

# Declaration

I, Michael Mitchley, hereby declare the contents of this dissertation to be my own work. This document is submitted for the degree of Master of Science at the University of the Witwatersrand, and has not been submitted to any other university, or for any other degree

A handwritten signature in black ink on a light blue background. The signature is stylized and appears to read 'M. Mitchley'.

# Contents

<b>Abstract</b>	<b>i</b>
<b>Declaration</b>	<b>ii</b>
<b>1 Introduction</b>	<b>1</b>
<b>2 Background</b>	<b>3</b>
2.1 Introduction . . . . .	3
2.2 Sonar . . . . .	3
2.2.1 The Physics of Sound in Water . . . . .	3
2.2.2 The Development of Sonar . . . . .	4
2.2.3 Multibeam Sonar . . . . .	6
2.2.4 Sidescan Sonar . . . . .	10
2.2.5 Sonar Bathymetry . . . . .	12
2.3 Sonar Signal Processing . . . . .	13
2.3.1 Noise . . . . .	13
2.3.2 Error . . . . .	14
2.3.3 Beamforming . . . . .	15
2.3.4 Bathymetry Calculation in Multibeam Systems . . . . .	16
2.3.5 Visualisation . . . . .	18
2.4 Beamforming and Phased Arrays . . . . .	20
2.4.1 Time-Delay Beamforming . . . . .	20
2.4.2 Phase Delays and Fourier Transforms . . . . .	20
2.4.3 Interferometry . . . . .	22
2.5 High Resolution Beamforming . . . . .	23
2.5.1 The Signal Model . . . . .	23
2.5.2 Conventional Beamforming . . . . .	25
2.5.3 The High Resolution Approach . . . . .	26
2.5.4 MUSIC . . . . .	27
2.5.5 Subspace Fitting . . . . .	28
2.5.6 ESPRIT . . . . .	30
2.5.7 Signal Enumeration . . . . .	30
2.5.8 Covariance Matrix Estimation . . . . .	32
2.6 Overview . . . . .	33

<b>3</b>	<b>Methodology</b>	<b>34</b>
3.1	Introduction . . . . .	34
3.2	Problem Definition . . . . .	34
3.3	Research Hypothesis . . . . .	34
3.4	Methodology . . . . .	35
3.4.1	Covariance Estimation . . . . .	35
3.4.2	Noise Field Estimation . . . . .	35
3.4.3	Signal Enumeration . . . . .	36
3.4.4	Beamforming . . . . .	36
3.4.5	Depth Profiling . . . . .	37
3.4.6	Data Sets and Simulation . . . . .	37
3.4.7	Parameter Variation . . . . .	37
3.5	Contributions . . . . .	38
<b>4</b>	<b>Simulator</b>	<b>39</b>
4.1	Introduction . . . . .	39
4.2	Simulator Function . . . . .	39
4.2.1	Wavefront Modelling . . . . .	39
4.2.2	Seafloor and Ocean Modelling . . . . .	40
4.2.3	Range Calculation . . . . .	41
4.2.4	Hydrophone Array Signal Calculation . . . . .	42
4.2.5	Continuous Signal Model . . . . .	43
4.2.6	Noise . . . . .	44
4.3	Simulator Scope . . . . .	44
4.3.1	Parameters . . . . .	44
4.3.2	Limitations . . . . .	45
4.4	Design Issues and Testing . . . . .	45
4.4.1	Implementation and Usage . . . . .	45
4.4.2	Testing . . . . .	45
4.5	Ideal Ping Simulator . . . . .	46
4.5.1	Model . . . . .	46
4.5.2	Limitations and Usage . . . . .	46
4.6	Description of Data Sets . . . . .	47
4.6.1	Flat Seafloor Data Sets . . . . .	47
4.6.2	Rough Seafloor Data Sets . . . . .	49
<b>5</b>	<b>Results</b>	<b>53</b>
5.1	Introduction . . . . .	53
5.2	Signal Enumeration Experiment . . . . .	53
5.2.1	Results . . . . .	53
5.2.2	Discussion . . . . .	58
5.3	Depth Profile Experiment . . . . .	59
5.3.1	Results . . . . .	59
5.3.2	Discussion . . . . .	63
5.4	Profile Density Experiment . . . . .	65
5.4.1	Results . . . . .	65

5.4.2	Discussion . . . . .	67
5.5	Further Investigation . . . . .	69
5.6	Discussion . . . . .	75
5.7	Relation to Other Work . . . . .	76
<b>6</b>	<b>Conclusion</b>	<b>77</b>
<b>A</b>	<b>Full Depth Profile Results</b>	<b>79</b>
<b>B</b>	<b>Full Sounding Density Results</b>	<b>92</b>

# List of Figures

1.1	A robotic claw grasps a black smoker chimney. Image ©Nautilus Minerals Inc. . . .	2
2.1	A pattern of interference created by two projectors . . . . .	6
2.2	A typical projection pattern . . . . .	7
2.3	The energy of the projector array, showing sidelobes . . . . .	8
2.4	The beamwidth of the array, plotted against the number of sensors. . . . .	8
2.5	The formation of a swath . . . . .	9
2.6	The formation of a single beam . . . . .	10
2.7	The formation of multiple beams along the swath . . . . .	11
2.8	Roll, pitch and yaw of a ship . . . . .	14
2.9	A wavefront returns at an angle of $\theta$ . . . . .	15
2.10	A non-specular return to the hydrophone array . . . . .	17
2.11	A specular return to the hydrophone array . . . . .	18
2.12	A ray refracts as it passes between layers with differing sound velocities . . . . .	19
4.1	A ray from the projector strikes the seafloor and returns to the hydrophone array . .	40
4.2	A ray from the projector reflects off a seafloor element and returns to the hydrophone array . . . . .	41
4.3	A hydrophone obtains a signal from a region of interest . . . . .	42
4.4	The spectral output for data set 1 . . . . .	48
4.5	The spectral output for data set 2 . . . . .	48
4.6	The spectral output for data set 3 . . . . .	49
4.7	The spectral output for data set 4 . . . . .	50
4.8	The spectral output for data set 5 . . . . .	50
4.9	The spectral output for data set 6 . . . . .	51
4.10	Depth profile for data sets 5 and 6 . . . . .	51
4.11	The spectral output for data set 7 . . . . .	51
4.12	The spectral output for data set 8 . . . . .	52
4.13	Depth profile for data sets 7 and 8 . . . . .	52
5.1	Mean depth errors for selected beamforming methods on data set 7 . . . . .	70
5.2	Mean depth errors for selected beamforming methods on data set 8 . . . . .	70
5.3	Mean depth errors for selected beamforming methods on data set 7 using a fixed grid	72
5.4	Mean depth errors for selected beamforming methods on data set 8 using a fixed grid	72
5.5	Bottom profile obtained by the Bartlett beamformer on data set 8 using a fixed grid	73
5.6	Bottom profile obtained by the Capon beamformer on data set 8 using a fixed grid .	74

5.7 Bottom profile obtained by the MUSIC beamformer on data set 8 using a fixed grid 74



# List of Tables

2.1	The angles of beams formed by an FFT for $L = 10$ . . . . .	22
4.1	Attenuation Figures for $10^{\circ}C$ salt water . . . . .	41
4.2	Summary of data set properties . . . . .	47
5.1	Signal enumeration results for data set 1 . . . . .	54
5.2	Signal enumeration results for data set 2 . . . . .	55
5.3	Signal enumeration results for data set 3 . . . . .	56
5.4	Signal enumeration results for data set 4 . . . . .	57
5.5	Mean depth errors for FB-smoothed R-estimation and structured noise correction applied to data sets 1 & 2 . . . . .	60
5.6	Mean depth errors for FB-smoothed R-estimation and structured noise correction applied to data sets 3 & 4 . . . . .	61
5.7	Mean depth errors for FB-smoothed R-estimation and structured noise correction applied to data sets 5 & 6 . . . . .	62
5.8	Mean depth errors for FB-smoothed R-estimation and structured noise correction applied to data sets 7 & 8 . . . . .	63
5.9	Number of soundings for FB-smoothed R-estimation and structured noise correction applied to data sets 1 & 2 . . . . .	66
5.10	Number of soundings for FB-smoothed R-estimation and structured noise correction applied to data sets 3 & 4 . . . . .	66
5.11	Number of soundings for FB-smoothed R-estimation and structured noise correction applied to data sets 5 & 6 . . . . .	67
5.12	Number of soundings for FB-smoothed R-estimation and structured noise correction applied to data sets 7 & 8 . . . . .	68
5.13	Mean depth errors for five selected methods performed on data sets 7 and 8 . . . . .	71
5.14	Mean depth error results on a fixed grid of 7000 points . . . . .	71
A.1	Mean depth errors for F-smoothed R-estimation, AIC signal enumeration and coherent noise correction performed on data set 1 . . . . .	79
A.2	Mean depth errors for F-smoothed R-estimation, MDL signal enumeration and coherent noise correction performed on data set 1 . . . . .	80
A.3	Mean depth errors for F-smoothed R-estimation, KN signal enumeration and coherent noise correction performed on data set 1 . . . . .	80
A.4	Mean depth errors for F-smoothed R-estimation, AIC signal enumeration and coherent noise correction performed on data set 2 . . . . .	81

A.5	Mean depth errors for F-smoothed R-estimation, MDL signal enumeration and coherent noise correction performed on data set 2 . . . . .	81
A.6	Mean depth errors for F-smoothed R-estimation, KN signal enumeration and coherent noise correction performed on data set 2 . . . . .	82
A.7	Mean depth errors for F-smoothed R-estimation, AIC signal enumeration and coherent noise correction performed on data set 3 . . . . .	82
A.8	Mean depth errors for F-smoothed R-estimation, MDL signal enumeration and coherent noise correction performed on data set 3 . . . . .	83
A.9	Mean depth errors for F-smoothed R-estimation, KN signal enumeration and coherent noise correction performed on data set 3 . . . . .	83
A.10	Mean depth errors for F-smoothed R-estimation, AIC signal enumeration and coherent noise correction performed on data set 4 . . . . .	84
A.11	Mean depth errors for F-smoothed R-estimation, MDL signal enumeration and coherent noise correction performed on data set 4 . . . . .	84
A.12	Mean depth errors for F-smoothed R-estimation, KN signal enumeration and coherent noise correction performed on data set 4 . . . . .	85
A.13	Mean depth errors for FB-smoothed R-estimation, AIC signal enumeration and structured noise correction performed on data set 5 . . . . .	85
A.14	Mean depth errors for FB-smoothed R-estimation, MDL signal enumeration and structured noise correction performed on data set 5 . . . . .	86
A.15	Mean depth errors for FB-smoothed R-estimation, KN signal enumeration and structured noise correction performed on data set 5 . . . . .	86
A.16	Mean depth errors for FB-smoothed R-estimation, AIC signal enumeration and structured noise correction performed on data set 6 . . . . .	87
A.17	Mean depth errors for FB-smoothed R-estimation, MDL signal enumeration and structured noise correction performed on data set 6 . . . . .	87
A.18	Mean depth errors for FB-smoothed R-estimation, KN signal enumeration and structured noise correction performed on data set 6 . . . . .	88
A.19	Mean depth errors for FB-smoothed R-estimation, AIC signal enumeration and structured noise correction performed on data set 7 . . . . .	88
A.20	Mean depth errors for FB-smoothed R-estimation, MDL signal enumeration and structured noise correction performed on data set 7 . . . . .	89
A.21	Mean depth errors for FB-smoothed R-estimation, KN signal enumeration and structured noise correction performed on data set 7 . . . . .	89
A.22	Mean depth errors for FB-smoothed R-estimation, AIC signal enumeration and structured noise correction performed on data set 8 . . . . .	90
A.23	Mean depth errors for FB-smoothed R-estimation, MDL signal enumeration and structured noise correction performed on data set 8 . . . . .	90
A.24	Mean depth errors for FB-smoothed R-estimation, KN signal enumeration and structured noise correction performed on data set 8 . . . . .	91
B.1	Number of soundings for F-smoothed R-estimation, AIC signal enumeration and coherent noise correction performed on data set 1 . . . . .	92
B.2	Number of soundings for F-smoothed R-estimation, MDL signal enumeration and coherent noise correction performed on data set 1 . . . . .	93

B.3	Number of soundings for F-smoothed R-estimation, KN signal enumeration and coherent noise correction performed on data set 1 . . . . .	93
B.4	Number of soundings for F-smoothed R-estimation, AIC signal enumeration and coherent noise correction performed on data set 2 . . . . .	94
B.5	Number of soundings for F-smoothed R-estimation, MDL signal enumeration and coherent noise correction performed on data set 2 . . . . .	94
B.6	Number of soundings for F-smoothed R-estimation, KN signal enumeration and coherent noise correction performed on data set 2 . . . . .	95
B.7	Number of soundings for F-smoothed R-estimation, AIC signal enumeration and coherent noise correction performed on data set 3 . . . . .	95
B.8	Number of soundings for F-smoothed R-estimation, MDL signal enumeration and coherent noise correction performed on data set 3 . . . . .	96
B.9	Number of soundings for F-smoothed R-estimation, KN signal enumeration and coherent noise correction performed on data set 3 . . . . .	96
B.10	Number of soundings for F-smoothed R-estimation, AIC signal enumeration and coherent noise correction performed on data set 4 . . . . .	97
B.11	Number of soundings for F-smoothed R-estimation, MDL signal enumeration and coherent noise correction performed on data set 4 . . . . .	97
B.12	Number of soundings for F-smoothed R-estimation, KN signal enumeration and coherent noise correction performed on data set 4 . . . . .	98
B.13	Number of soundings for FB-smoothed R-estimation, AIC signal enumeration and structured noise correction performed on data set 5 . . . . .	98
B.14	Number of soundings for FB-smoothed R-estimation, MDL signal enumeration and structured noise correction performed on data set 5 . . . . .	99
B.15	Number of soundings for FB-smoothed R-estimation, KN signal enumeration and structured noise correction performed on data set 5 . . . . .	99
B.16	Number of soundings for FB-smoothed R-estimation, AIC signal enumeration and structured noise correction performed on data set 6 . . . . .	100
B.17	Number of soundings for FB-smoothed R-estimation, MDL signal enumeration and structured noise correction performed on data set 6 . . . . .	100
B.18	Number of soundings for FB-smoothed R-estimation, KN signal enumeration and structured noise correction performed on data set 6 . . . . .	101
B.19	Number of soundings for FB-smoothed R-estimation, AIC signal enumeration and structured noise correction performed on data set 7 . . . . .	101
B.20	Number of soundings for FB-smoothed R-estimation, MDL signal enumeration and structured noise correction performed on data set 7 . . . . .	102
B.21	Number of soundings for FB-smoothed R-estimation, KN signal enumeration and structured noise correction performed on data set 7 . . . . .	102
B.22	Number of soundings for FB-smoothed R-estimation, AIC signal enumeration and structured noise correction performed on data set 8 . . . . .	103
B.23	Number of soundings for FB-smoothed R-estimation, MDL signal enumeration and structured noise correction performed on data set 8 . . . . .	103
B.24	Number of soundings for FB-smoothed R-estimation, KN signal enumeration and structured noise correction performed on data set 8 . . . . .	104

# Chapter 1

## Introduction

Many traditional mines face diminishing returns and growing expenses due to mineral scarcity [Diederer 2009]. Falling ore grades, the high cost of deeper mining, and the growing cost associated with locating and sampling new ore veins are factors prompting a number of companies to look to the deep ocean as a new frontier in resource exploitation [Birney *et al.* 2008]. Two companies in particular, Nautilus Minerals Inc. and Neptune Minerals, are exploring seafloor massive sulphide (SMS) deposits. These deposits occur around deep sea hydrothermal vents, where upwellings of mineral-laden water from faults in the earth's crust form chimney-like structures known as *black smokers*, and sulphide mounds [Helene *et al.* 2009]. One such black smoker is shown in Figure 1.1. One can see several shells affixed to the structure, as well as the robotic claw of the ROV exploring the seafloor.

It is found that such deposits are rich in metals such as copper, zinc, gold and silver [Lipton 2008]. SMS deposits have been found in the deep ocean at depths greater than one kilometre. Black smokers are also active hydrothermal vents, which results in acidic water at high temperatures. In the Solwara region surveyed by Nautilus Minerals, the water temperature around the vents was in the neighbourhood of 150° Celsius. These factors, combined with the total darkness of the mining site imply that the mining is necessarily robotic. Such robotic platforms must be robust to extreme pressures and changes in temperature. It has been found that deep sea mining (DSM) has less environmental impact than traditional mining, and may be cheaper [Birney *et al.* 2008].

Currently, only extinct black smokers (that is, those vents that no longer support exotic ecosystems, and are no longer volcanically active) are considered for mining purposes by Nautilus Minerals. In order to find these inactive vents, Nautilus Minerals first locates active vent sites, which can be found along fault lines through an examination of the geomorphology of the ocean floor via sonar, and by sampling the water for indicator minerals [Birney *et al.* 2008]. Inactive vents are found in the vicinity of active vents through deep sea exploration via remotely operated vehicles (ROVs) and autonomous underwater vehicles (AUVs), a costly exercise.

Sonar data gathered by systems mounted on ship hulls are inexpensive, and can be gathered continuously while the ship is in motion. Currently, the sonar systems employed by Nautilus Minerals produce bathymetric maps at a resolution of 25m at depths of 2km. This is too coarse to detect SMS chimneys, which are approximately 1m across. The aim of this research is then to



Figure 1.1: A robotic claw grasps a black smoker chimney. Image ©Nautilus Minerals Inc.

improve the resolution of the sonar data such that one may detect an SMS chimney at  $2km$  depth, reliably.

As the focus of this project is on improving the resolution of an existing sonar system, we will examine sonar in depth in Chapter 2, with attention paid to the processing of data produced by multibeam bathymetric systems, particularly the so-called high resolution approach.

By examining the literature, relevant techniques are identified. A focussed research problem, hypothesis and methodology are outlined in Chapter 3. The core contribution of this research is an in-depth testing of various method combinations aimed at improving the resolution of sonar-derived bathymetric data. To aid in this testing, two simulators were created. These simulators are discussed in Chapter 4, together with the data sets created.

Summaries of the results of performing the research methodology on the various data sets are presented in Chapter 5, and are discussed with reference to the hypotheses of Chapter 3. The data used in the summaries are relegated to the appendix, for completeness. Finally, the research is summarised and concluded in Chapter 6.

## Chapter 2

# Background

### 2.1 Introduction

The primary tool of ocean floor remote sensing is sonar. Sonar is an acronym, standing for SOund Navigation and Ranging, and refers to the specific use of sound as a remote sensing tool. In this Chapter, the mathematics and usage of sonar will be explored with a focus on the context of deep sea *bathymetry*, or depth measurement.

In Section 2.2, an overview of sonar will be presented, focussing on the concepts at the heart of sonar rather than engineering challenges. We will briefly introduce the ideas behind beamforming and multibeam sonar technologies, as well as their applications. Other technologies, such as sidescan sonar, will also be discussed. Section 2.4 will introduce the mathematics behind conventional beamforming in multibeam systems, with a focus on the problems encountered in conventional systems. Section 2.5 introduces high resolution beamforming, rephrasing the conventional beamformers under the assumed signal model of the high resolution approach. Estimation of the various parameters required for high resolution beamforming is discussed.

### 2.2 Sonar

#### 2.2.1 The Physics of Sound in Water

Sound travels through a medium as a series of moving compression fronts in a wave form. Sound can travel through any medium, but travels faster through a denser medium. Sound waves are typically sinusoidal, and are thus complex signals, possessing both amplitude and phase. The amplitude of a sound wave is the peak power of the wave measured as deviation from standard pressure. The phase is the position of the wave in its fluctuating cycle. The wavelength is the distance between peaks, while the period is the time taken for a single phase of the wave to pass a stationary point. The frequency of the sound is the number of waves that can pass a point in a single second.

The wavelength, frequency and speed of the sound are related by the equation [Waite 2002][pg 1]

$$c = \lambda f,$$

where  $c$  is the speed of sound in the medium,  $\lambda$  is the wavelength and  $f$  is the frequency. The speed of sound in sea water is dependent on a number of factors, increasing as the water temperature, salinity and pressure increase. The salinity of sea water varies geographically, but is constant with depth (provided no fresh water mixing takes place [Kammerer *et al.* 1998]). Pressure increases with depth in a predictable way, but temperature varies with time, depth and location [L-3 2000], introducing nonlinearity to the speed of sound. When a sound wave traveling through water changes its speed, the frequency of the wave remains constant, while its wavelength changes. The sound wave is also refracted, meaning that a hypothetical sound ray would not follow a straight line as it moves through the ocean.

When a sound wave moves through a medium, it is said to *propagate*. Propagation loss (the reduction in sound intensity between source and receiver) occurs through a number of mechanisms. Spreading losses occur as the sound wave expands through the medium. This loss depends on the propagation pattern, but can be characterised by the power present in the wave being constant and equal to the intensity of the sound wave per unit area multiplied by its area [Waite 2002][pg 44]. Absorption loss (or attenuation) occurs through friction, and chemical changes to the medium. An approximation of the *attenuation* coefficient  $\alpha$  in sea water, given by Waite [2002][pg 47] is  $\alpha = 0.05f^{1.4} \text{ dB/km}$ .

The use of sound for remote sensing underwater is motivated by a number of factors. Firstly, sound travels further and faster in water than in air. This is due to the fact that sound propagates in water with little attenuation. In contrast, light waves and radar (two common tools in remote sensing) propagate only a few meters in water. The attenuation coefficient  $\alpha_{EM}$  of radar in typical sea water is given by  $\alpha_{EM} = 1400f^{0.5} \text{ dB/km}$ , meaning that at  $30\text{kHz}$ , radar will attenuate at  $7500\text{dB}$  per kilometer [Waite 2002][pg 49]. This makes it useless in most underwater remote sensing applications, where ocean depths may be in the order of hundreds or thousands of meters, and the energy emitted by a projector is limited by cavitation (the creation of bubbles due to rapid movement of a projector, or sea water boiling) [Waite 2002][pg 6].

When a sound wave strikes a solid object, some of the energy of the wave is reflected off the object in the form of an echo, a sound wave of decreased amplitude but identical frequency. The rest of the energy is scattered, or absorbed into the object. The *acoustic impedance* and roughness of the sea floor may be of interest, and can be estimated using the *backscatter* strength, which is the strength of the returning signal [Fonseca and Mayer 2007; Kammerer *et al.* 1998]. Backscatter can be used to indicate the material makeup of the seabed [Brown *et al.* 2010]. Backscatter is discussed further in Section 2.2.4.

## 2.2.2 The Development of Sonar

The first recorded description of the use of sound as a remote sensing tool in water was by Leonardo da Vinci, as a method for detecting approaching ships. As with many of his inventions, it would be centuries before the technology was actualised [Pujol 2007][pg 6].

The first practical sonar devices were developed following the sinking of the Titanic, and the use of submarines in the first world war [Pujol 2007][pg 7]. These devices were based on piezoelectric transducers, capable of converting electrical energy into acoustic energy in order to produce a sound wave to function as a projector, and measuring acoustic energy as an electrical signal to act as a hydrophone [Pujol 2007][pg 7]. As is the case with speakers and microphones, the principle differences between the two devices are in the associated circuitry, with hydrophones including (for example) digitisers and fast Fourier transform circuitry.

Early sonar systems consisted of a single projector and hydrophone. A ping from the projector produced a spherical wavefront, expanding in all directions equally (ignoring differences in velocities). Likewise, the hydrophone measured in all directions equally. Thus, when an echo was detected, it was not possible to say from which direction the echo came from. However, from the time taken for the echo to return to the ship, a range could be estimated (assuming knowledge of the speed of sound in water). It was also now possible for ships to continuously record depths as they travelled. These gave way to precision depth sounder and recorders (PDRs) in the 1950s, which had a beamwidth of between  $30^\circ$  and  $60^\circ$ , allowing accurate measurement of depths [de Moustier 1988].

This led to sparse bathymetric maps, which were interpreted by hydrographers to produce contour maps. These maps aided ships in safe navigation as it was then known that, at that point, the nearest obstacle was some distance from the ship (although the location of that obstacle was still unknown).

Narrow beam echosounders were the next development, using arrays of projectors and hydrophones to measure depths within a  $2^\circ$  beam. With the increase in computational power in the 1970's, these gave way to commercially available multibeam echosounders, which were able to produce dense bathymetric maps [de Moustier 1988], discussed further in Section 2.2.3. The low cost of multibeam surveys has led to widespread imaging of the sea floor [Brown *et al.* 2010].

New sidescan and multibeam sonar systems are incorporating pulse frequency modulation, to increase the energy (and thus signal to noise ratio) in the pulse [Pujol 2007][pg 15]. These are also known as ‘chirp’ systems, leading to increased seabed penetration in shallow water subsurface imaging systems [Savini and Corselli 2010] as well as making the signal robust to doppler shifting [Tarlet *et al.* 2007]. Frequency modulation allows multiple pings to enter the water column at once (or even continuously, as is the case with continuous active sonar [van Vossen *et al.* 2009]), increasing the along-track resolution [Mayer 2006]. As the use of frequency modulation typically leads to a broadband system [Mayer 2006], it will not be the focus of this document. Instead, we will focus solely on narrowband sonar most commonly used by current multibeam systems, particularly multibeam echosounders operating in deep sea environments, such as those used to locate SMS deposits.



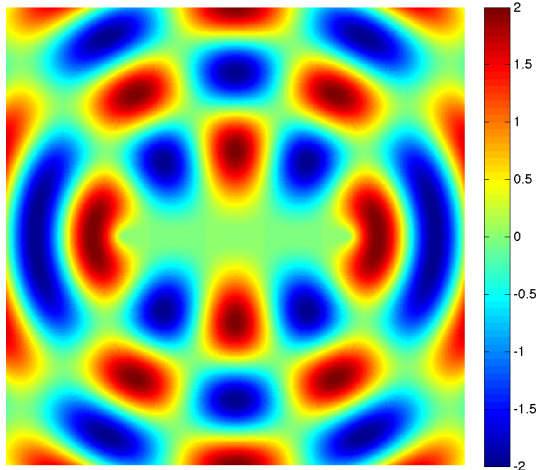


Figure 2.1: A pattern of interference created by two projectors

### 2.2.3 Multibeam Sonar

A problem with a single projector system is that a single ping expands spherically, *ensonifying* (or exposing to sound) the entire ocean floor surrounding the vessel. Returning soundwaves could be echoes from any direction within the ensonified region (although the range can be accurately computed). To overcome this problem, an array of projectors is used to create a wavefront shaped by creative and destructive interference wherein the most energy lies perpendicular to the array. Such interference is demonstrated in Figure 2.1. Here, two projectors emit a sinusoidal wave of unit amplitude in a two dimensional plane. One can see a pattern of constructive interference, wherein the amplitude increases to a magnitude of two, and destructive interference, wherein both waves cancel each other.

The end result of this process is a ping with energy projected in a lobed, torus-like shape (shown in Figure 2.2), rather than a sphere. The most energy is within the main lobe (and so we can expect stronger returns from this area) while outside of the main lobe, there is very little energy, leading to negligible returns from areas not ensonified by the main lobe. We can quantify this using a result from Nielsen [1991][pg 55], which states that if a complex sinusoid plane wave  $s(t) = e^{\frac{2\pi i f t}{f_s}}$  (where  $f$  and  $f_s$  are the signal and sampling frequencies respectively) strikes a uniform linear array of  $L$  hydrophones at an angle of  $\theta$ , the beam power pattern measured at  $\theta$ ,  $\|b(f, \theta)\|^2$ , is given by equation 2.1. By the principle of reciprocity, this result also applies to the power transmitted by a uniform linear array of  $L$  projectors each separated by a distance of  $d$ .

$$\|b(f, \theta)\|^2 = \left\| \frac{\sin \frac{\pi f L d \sin \theta}{c}}{\sin \frac{\pi f d \sin \theta}{c}} \right\|^2 \quad (2.1)$$

We should note the appearance of the side lobes though, shown in Figure 2.3. Side lobes are an inevitable consequence of the swath-forming procedure [L-3 2000], and lead to small returns from

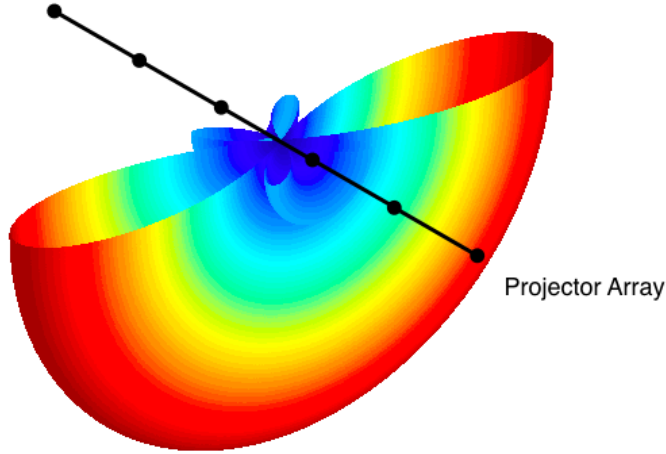


Figure 2.2: A typical projection pattern

outside the swath, appearing as noise or inconsistent data. The energy within the side lobes can be reduced through schemes such as Dolph-Chebyshev shading at the cost of widening the main lobe. Our trade-off is thus between array size (and thus cost), noise and resolution. Likewise, shading can be used to increase hydrophone array sensitivity by weighting elements to maximise signal to noise ratio (SNR) [Chen and Gershman 2008].

Using this equation, [Nielsen 1991][pg 59] examines the  $3 - dB$  beamwidth, the width of the portion of the main lobe such that the power is greater than or equal to  $-3dB$ , where the maximum output of the lobe (at  $\theta = 0$ ) is taken as  $0dB$ . Assuming we are projecting a swath directly below the vessel, and taking the small angle approximation  $\sin \theta \approx \theta$ , we can solve equation 2.1 to obtain

$$\sin \theta_{3-dB} \approx \pm \frac{0.44c}{Lfd}$$

where as before  $f$  is the signal frequency,  $L$  is the number of array elements and  $d$  is the uniform spacing between them, and so taking the difference between these two answers, we obtain the  $3 - dB$  beamwidth (for projection directly below the platform) as

$$\delta\theta_{3-dB} \approx 2\sin^{-1} \left[ \frac{0.44c}{Lfd} \right].$$

If we assume a sensor spacing of  $d = \lambda/2$ , this reduces to

$$\delta\theta_{3-dB} \approx 2\sin^{-1} \left[ \frac{0.88}{L} \right]$$

which is plotted in Figure 2.4.

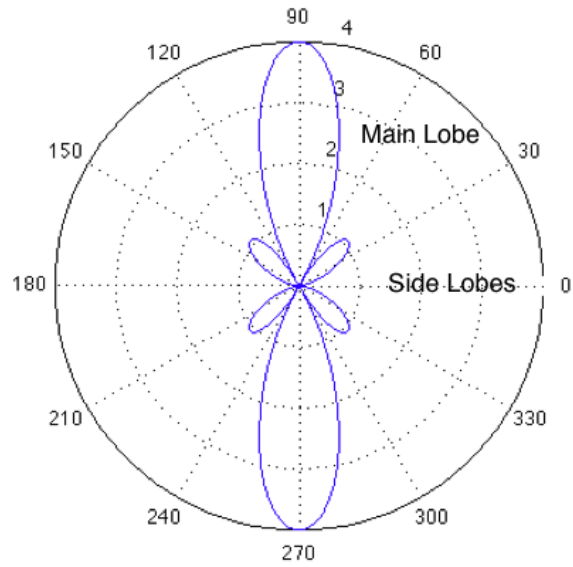


Figure 2.3: The energy of the projector array, showing sidelobes

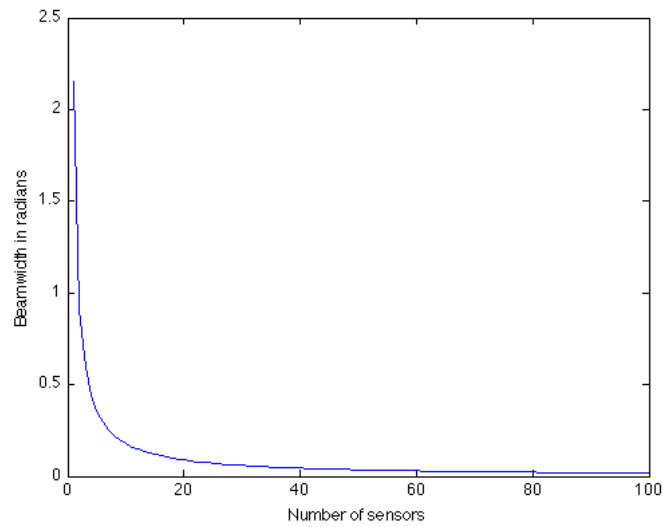


Figure 2.4: The beamwidth of the array, plotted against the number of sensors.

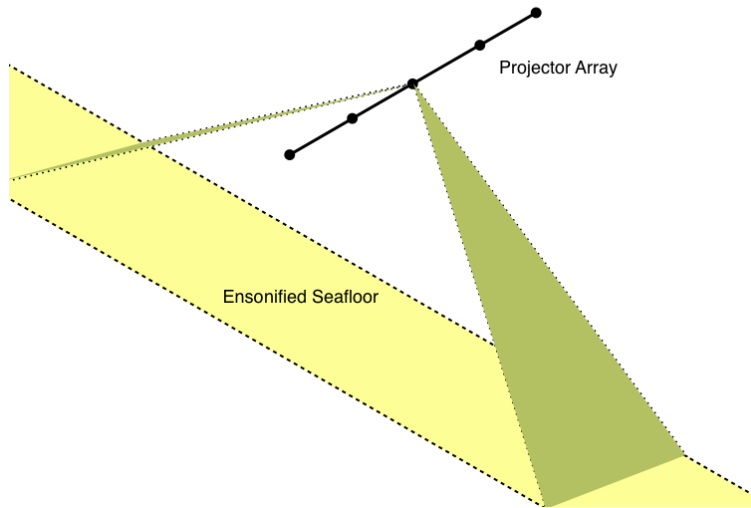


Figure 2.5: The formation of a swath

This shows that, all else being equal, the width of the swath formed is a function of the number of projectors in the array only. To form an unshaded swath of width  $1^\circ$ , we require at least 101 projector elements.

The torus-shaped sound wave emitted by the projector array strikes the ocean floor, ensonifying a narrow strip on the ocean floor called a *swath*. Those parts of the swath closest to the projector array (and thus the ship) will be struck by the sound wave first. This is illustrated in Figure 2.5.

Typically, the projector array is mounted along the track of the ship, producing a swath that is perpendicular to the direction of the ship.

Just as we can maximise the energy expended in a particular direction, so we can maximise the sensitivity of the hydrophone array to energy from a particular direction. Mounting the projector and hydrophone arrays perpendicular to each other (with the projector array along the track of the ship and the hydrophone array mounted athwartship) produces a Mills cross [L-3 2000]. In this scheme, an athwartship swath is ensonified, and an alongtrack swath is monitored. The intersection of the two swaths is an area both ensonified and monitored, as illustrated in Figure 2.6. This intersection is known as a beam (although, Chrisofilakis *et al.* [2008] call the preferential transmission of a signal in a specific direction beamforming). The techniques used to form beams in different directions will be discussed in detail in Sections 2.3.3 and 2.4.

In a single ping cycle, many beams can be formed simultaneously (as beamforming is a data processing technique). Typically, beams are formed all along the swath, as illustrated in Figure 2.7. For each beam, we will attempt to detect the moment of return of the echo of the projected ping. From this moment of return, we can estimate the range, and thus the depth of the ocean floor within that beam. Thus, bathymetric information consisting of depth estimates and locations can be obtained for the entire swath in each ping cycle. This gives rich, dense bathymetric data

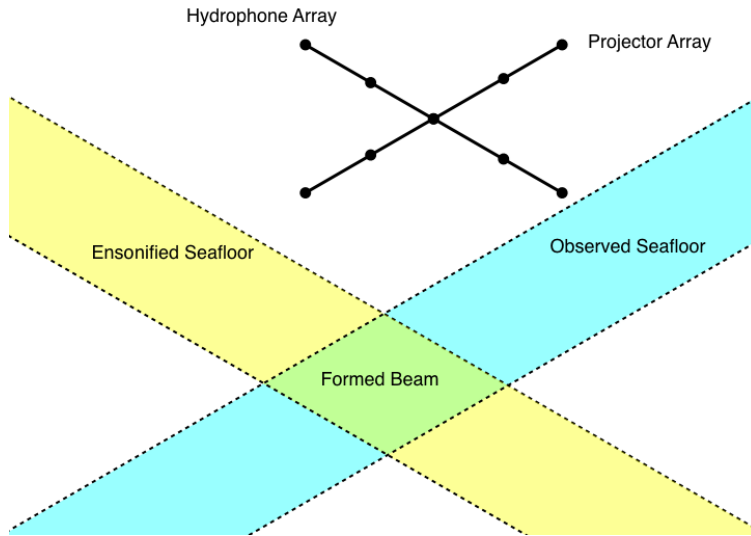


Figure 2.6: The formation of a single beam

(upwards of one million points per hour [Canepa *et al.* 2003]), offering advantages over the sparse bathymetric data of single beam systems, but posing greater challenges too. The density of the data makes human operator intervention more difficult [Calder and Mayer 2001].

The product of a multibeam bathymetric system is a series of depth measurements (one for each beam), together with the backscatter, or amplitude of the return for that beam. It is interesting to compare and contrast the backscatter generated by multibeam systems with those generated by sidescan systems, which shall be done in the following Section.

#### 2.2.4 Sidescan Sonar

Sidescan sonar is a sonar technology focussing on accurate backscatter strength mapping rather than bathymetry. As sidescan sonar is not used in this application due to its inferior bathymetric accuracy [Yang and Taxt 1997], we will focus chiefly on the differences between it and multibeam systems, and the data products obtained from each. Sidescan sonar has a different array geometry to multibeam systems, typically using a towed linear array of hydrophone elements arranged along the ship's track, or hull-mounted arrays pointing in different angles.

Sidescan sonar works by ensonifying successive strips of the seafloor athwartships, producing an image of the seafloor by plotting backscatter intensity against return time [Pujol 2007][pg 18]. Backscatter returns are those returns generated by signal scattering, as opposed to echoes, returns generated by a reflection of the ping signal. The backscatter map relies on micro-scale relief to be accurate. In the presence of macro-scale relief variation, there will be acoustic shadows, echoes and inaccurate return times [Pujol 2007][pg 18].

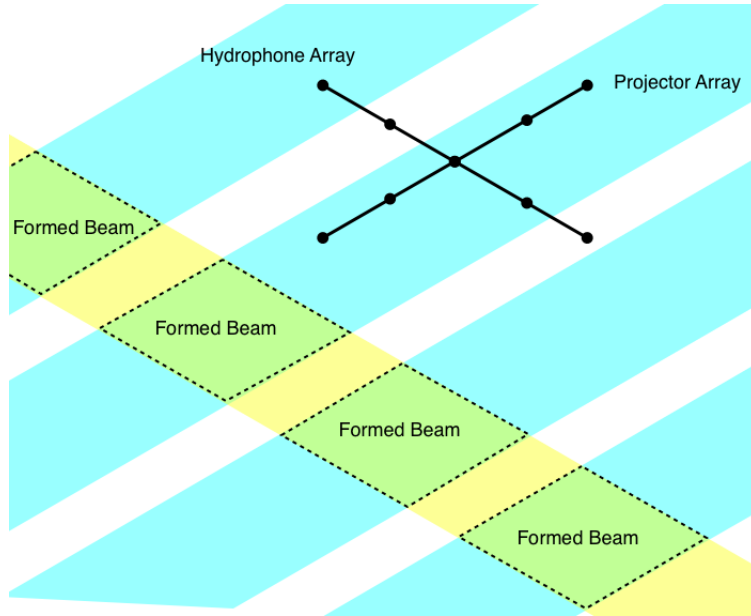


Figure 2.7: The formation of multiple beams along the swath

In contrast with a bathymetric map, which shows the reported depth at each point, a backscatter map will show the return intensity at each point. The hydrophone array of a sidescan system is typically a uniform linear array in the direction of motion, similar to that of a radar system, and indeed techniques such as Synthetic Aperture Radar (SAR) can be used to simulate a larger array. In sonar, this is known as Synthetic Aperture Sonar (SAS). In this system, a synthetic array is produced by moving the sonar array and ensonifying the same seafloor swath repeatedly, from different angles. The length of the synthetic array is equal to the distance travelled [Pujol 2007][pg 19].

Asada and Yabuki [2001] demonstrated the use of SAS in a multibeam sonar system, where the hydrophone array is mounted athwartship. Here, extremely precise localisation of the platform was required. For each ping cycle the beams formed were shifted to known lines through an interpolation technique. Once the data had been motion corrected, the beams were combined using the SAS technique, drastically decreasing the angular beamwidth of the system, thereby increasing the resolution.

In shallow water applications, sidescan sonar can also be used to obtain surficial and subsurficial information about the seabed, which can be used in materials analysis [Magoon *et al.* 2009; Fonseca and Mayer 2007]. Pan *et al.* [2009] discuss the use of SAS in the detection of small seafloor objects. Here, SAS is used to reduce reverberations as well as increase resolution. Correcting path ambiguity caused by reverberations between the seafloor and surface through SAS is demonstrated by Pinto *et al.* [2004]. This paper also illustrates a number of interesting problems encountered in shallow water sonar applications. de Paulis *et al.* [2009] introduce a technique for focussing SAS data. The development of SAS is succinctly reviewed in Gough and Hayes [2008].

Bathymetric multibeam systems also produce a backscatter strength map. Until recently, these maps have been of inferior quality to those produced by sidescan sonar systems due to a larger beamwidth. Technological improvements over the last decade have led to hull-mounted multibeam systems producing backscatter maps of equal or greater quality than those of sidescan systems [Brown *et al.* 2010]. Seafloor characterisation using backscatter amplitude maps, and problems associated with it, is the topic of a number of papers [Hellequin *et al.* 2003; Preston and Biffard 2007; Karoui *et al.* 2009].

### 2.2.5 Sonar Bathymetry

Historically, bathymetry was accomplished through physical probing of the water, through plumb-lines or poles, continuing until the 1920's. Physical measurements resulted in sparse bathymetric maps [de Moustier 1988], focussing only on bays, reefs and shores. Physical measurements were slow, difficult and prone to errors [Mayer 2006].

As described in Sections 2.2.2 and 2.2.3, bathymetric measurement was revolutionised by the invention of sonar. Physical measurements gave way to remote sensing through acoustics, leading to sparse bathymetric maps through early single-sounder and single-beam systems, and later to dense data through multibeam systems.

Shallow water bathymetry (such as in bays) leads to vastly different challenges from deep water bathymetry. In shallow water, the curvature of the wavefront bouncing off the seafloor must be taken into account in calculations, introducing the problem of knowing how curved the wavefront will be (itself dependent on the depth one is trying to estimate), requiring a dynamic focussing of the beam [Mayer 2006]. Additional problems are encountered through multiple paths, whereby waves reflect between the ocean surface and the floor, leading to uncertainty in the location of the received echoes [Pinto *et al.* 2004]. Despite these challenges, rich information can be obtained at a very high resolution.

Deep water bathymetry faces different challenges. The wavefront curvature is negligible (discussed further in Section 2.3.3), and attenuation in the deep water means multiple path echoes fall below the level of noise. Attenuation leads to a lower signal-to-noise ratio (SNR). Sound velocity profiles (discussed further in Section 2.3.4) are harder to estimate for deep water, and can introduce significant georeferencing errors in the soundings.

Many deep-sea bathymetric surveys have been performed in recent years ([Birney *et al.* 2008; Caress *et al.* 2008; Cazenave *et al.* 2008; Marsh and Brown 2009; Helene *et al.* 2009; Savini and Corselli 2010]), leading to a renewed interest in improving the resolution of deep-sea bathymetric mapping [Pujol 2007; Church and Warren 2008]. A review of advances in sonar bathymetry is given in Ranade [2006].

## 2.3 Sonar Signal Processing

### 2.3.1 Noise

In this Section we will examine three sources of noise in sonar systems, namely thermal noise, ambient noise and vessel noise [Waite 2002][pg 83]. Thermal noise is noise from the electrical impulses of the sonar system itself. Thermal noise is below the level of any other noise, and can only be observed in the absence of other noise sources, at the level of  $N_{therm} = -15 + 20 \log f \text{ dB}$ , taking the force of  $1\mu Pa$  as a reference, where  $f$  is the frequency of the sonar system in kilohertz. [Waite 2002][pg 85]. It is thus assumed that this noise is accounted for and minimised at a hardware level.

Ambient noise is the noise of the ocean itself. This noise can be great in shallow water, close to the surface [Waite 2002][pg 86]. Consider, for example, the roar of breaking waves. Other sources contributing to ambient noise are shipping, marine life, rain, thermal agitation of the ocean and agitation due to wind [Waite 2002][pg 88]. While Waite [2002][pg 90] states that ‘nothing can be done about the ambient noise of the sea’ from a hardware engineering perspective, it is the focus of many techniques to predict and correct for this noise.

In hull-mounted sonar systems, additional noise may enter through the hull [Nielsen 1991][pg 52]. This is the vessel noise arising from shipboard machinery, the flow of water around the ship, and the noise of the propellers [Waite 2002][pg 89]. This noise is system-dependent, persistent and predictable. Another source of noise is bubble masking from bubbles slipping under the hull through ship motion or rough seas [de Moustier 1988]. It will be assumed for this project that hull noise is accounted for at a hardware level.

We are thus left considering ambient noise. This noise is incoherent and assumed to be spatially white (that is, the distribution of the noise is independent of direction), independent for all sensors, and Gaussian. Consider a hydrophone array  $\vec{x}$  measuring a pure Gaussian noise field of variance  $\sigma^2$ . We define the spatial autocovariance matrix  $\mathbf{R}$  (discussed further in Section 2.5) as

$$\mathbf{R} = E \{ \vec{x}(t) \vec{x}^H(t) \} = \lim_{T \rightarrow \infty} \frac{1}{T} \sum_{t=0}^T \vec{x}(t) \vec{x}^H(t).$$

If we perform an eigenanalysis on  $\mathbf{R}$ , then with probability one the eigenvalues will converge to  $\sigma^2$  (that is, the noise variance) as the number of samples tends to infinity [Kritchman and Nadler 2008].

As this project focusses on active sonar, we will define another form of noise: coherent, persistent signals that do not correspond to a ping event. This noise may take the form of noise from an underwater vessel, or any similar noise source that will result in a signal continuously emanating from a stationary location. In passive sonar, this would be considered a signal. Ronhovde *et al.* [1999] refers to this noise as ‘structured noise’. We will adopt this terminology in this document.



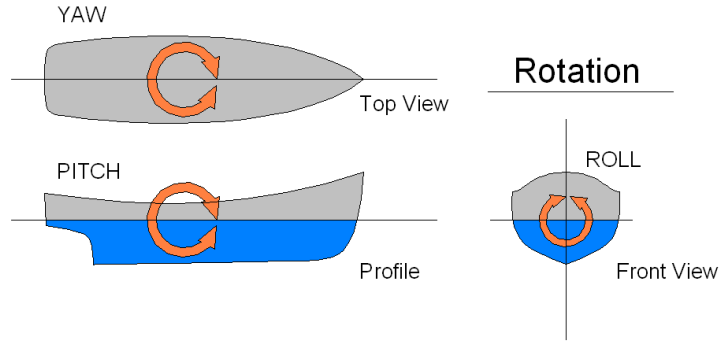


Figure 2.8: Roll, pitch and yaw of a ship

### 2.3.2 Error

Errors can be introduced to sonar data in a number of different ways. Array miscalibration is due to imperfect construction and correction of hydrophone arrays. Kammerer *et al.* [1998] discusses a problem found with an incorrectly calibrated EM1000 sonar system, wherein beam angles were not correctly computed, and had to be calibrated manually. The array elements used by Ronhovde [1999][pg 43] were slightly further apart than half a wavelength, leading to aliasing problems.

Errors can be introduced due to ship attitude (roll, pitch and yaw, as shown in Figure 2.8) which must be measured accurately in order to correct beam steering angles. Heave (the upward motion of a ship) due to rough sea conditions, and tidal fluctuations in sea level will introduce errors in depth mapping [Canepa *et al.* 2003].

GPS navigation errors can also interfere with data accuracy, especially for rough seafloors, where coordinate errors can overcome the sonar accuracy [Canepa *et al.* 2003]. Such errors can be guarded against through the use of high-accuracy GPS systems, such as the kinematic system used by Asada and Yabuki [2001], which can provide an accuracy of  $5cm$  in latitude, longitude and altitude [Mayer 2006].

Sound waves refract as they pass through the ocean due to variations in the speed of sound. Correcting for these refractions through the use of sound velocity profiles is discussed further in Section 2.3.4, although these corrections are approximate, and so the georeferencing of soundings may only be estimated.

In compensated systems, Canepa *et al.* [2003] states that the residual errors can be treated as white noise in the data. [Marks and Smith 2008] defines an uncertainty measure  $\sigma_e^2$  for multibeam data collected after 1968 as

$$\sigma_e^2 = 1 + (0.5d)^2 + (0.2s),$$

where  $d$  is the depth of the sounding and  $s$  the slope of the area when smoothed by a  $5km$  cosine bell.

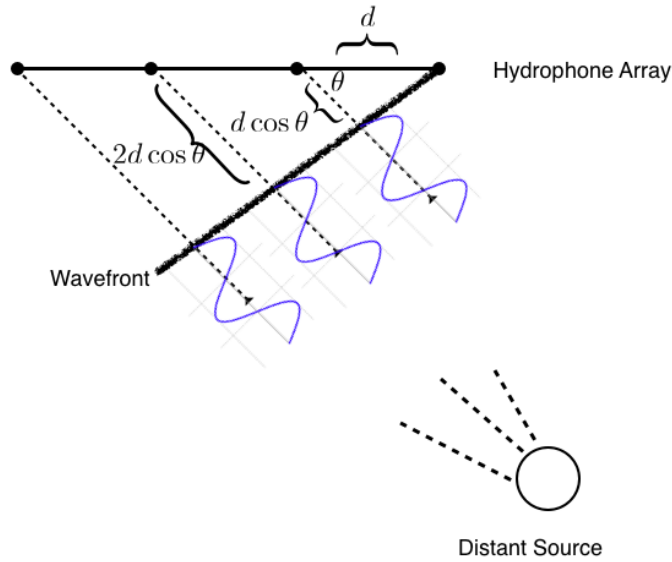


Figure 2.9: A wavefront returns at an angle of  $\theta$

### 2.3.3 Beamforming

We will cover conventional beamforming techniques briefly in this Section, as we will examine several beamforming methodologies in Section 2.4. As mentioned before in Section 2.2.3, the output of the projector array is shaped by creative and destructive interference into a narrow fan shape. This is done by introducing appropriate time delays between projector elements. By the principle of reciprocity, we may do the same thing to the hydrophone array, increasing sensitivity in a fan shape below the ship, and decreasing sensitivity outside of this main lobe.

Since the projector and hydrophone arrays are mounted perpendicular to each other, only a small Section of the ocean floor is both ensonified and subject to hydrophone scrutiny. This is known as the Mills cross technique. The intersection of hydrophone and projector patterns is called a beam, while the entire ensonified strip of seafloor is called the swath. The swath represents the Section of the seafloor about which we can obtain information by *steering* the hydrophone beam pattern, as shown in Figure 2.6.

We shall use the mechanism of time-delay beamforming to illustrate this process. Consider Figure 2.9, which shows an echo returning from the ocean floor at an angle of  $\theta$  perpendicular to the hydrophone array. We see that this echo will reach each hydrophone element at a different time. If the *scatterer* (or, point on the ocean floor from which the echo originates) is sufficiently far away, we may consider the wavefront of that echo to be approximately linear. This is known as the *far-field assumption*, which is appropriate in the context of deep-sea sonar. We then expect that the wavefront will strike each element of the hydrophone array with a delay of  $\frac{dk \sin \theta}{c}$ , where  $d$  is the distance between array elements (assumed uniform),  $k$  is the hydrophone element index and  $c$  is the speed of the wavefront.

If we introduce an appropriate time delay between the sampling of each element, we would then sample the echo as it passes each element. Summing the contributions of each element with this delay would then creatively amplify the in-phase signal from direction  $\theta$ , while destructively reducing the out-of-phase signals from every other direction. Thus, by changing the value  $\theta$  in the time delay  $\frac{dk \sin \theta}{c}$ , we change the direction of sensitivity of the hydrophone array. It is important to note that this is a data processing method, implying many beams can be formed at once with the same data. This is the most basic beamformer possible, and it suffers from interesting technical limitations discussed in Section 2.4.1. In practice, many sonar systems use a Fast Fourier Transform (FFT) beamformer to introduce phase delays L-3 [2000].

The beams we form translate the complex signal of each hydrophone element  $x_k(t)$  into some measure of the power of the signal originating from a direction  $\theta_i$ . This is called the return. Due to background noise, we can expect nonzero returns at all angles, at all times. We must then select only those returns that correspond to echoes from the ocean bottom. This may be done through thresholding of the return amplitudes, or through subspace analysis methods (described further in Section 2.5).

Another method at our disposal is start and stop gates [L-3 2000]. While we may not know the exact topology of the ocean floor, we do have some estimate of the depth *a priori*. Thus, for some fixed  $\theta$ , we need only listen for a return between specific times corresponding to the maximum and minimum expected depth. Equivalently, at any particular time instant, we can expect returning echoes along a specific range of angles [Yang and Taxt 1997].

### 2.3.4 Bathymetry Calculation in Multibeam Systems

At each sampling instant of the hydrophone array, we may potentially obtain a number of returns across the swath. Each return will have associated with it a Direction of Arrival (DOA) and Time of Arrival (TOA). We may obtain a number of returns for each beam, at different TOAs and (if measured accurately), at different DOAs. L-3 [2000] describes two methods for estimating DOA and TOA using the amplitudes of beams formed by an FFT. We examine these two methods to highlight the issues at play.

The first method, Bearing Direction Indicator (BDI), seeks to accurately compute the DOA, and then average across the range of TOAs. In this method we consider the information across all the beams, for each individual time slice. The DOA of an echo is estimated by fitting a model to the amplitude of the returns across neighbouring beams, as the beams from the FFT beamformer overlap. The model used by L-3 [2000] is a parabola, with the turning point centred at the DOA. The valid returns (after thresholding and application of start and stop gates) are then grouped into beams, and the DOA and TOA for that beam are computed as the amplitude-weighted means of the DOAs and TOAs of the returns. Thus, the final DOA for a beam need not coincide with the beam axis. At each individual time slice, we expect two echoes, although for rough sea floors there may be more [Yang and Taxt 1997].

This method is found to perform best when the echo is *non-specular*, corresponding to low grazing angles typically seen towards the outer edges of the swath as shown in Figure 2.10. In this

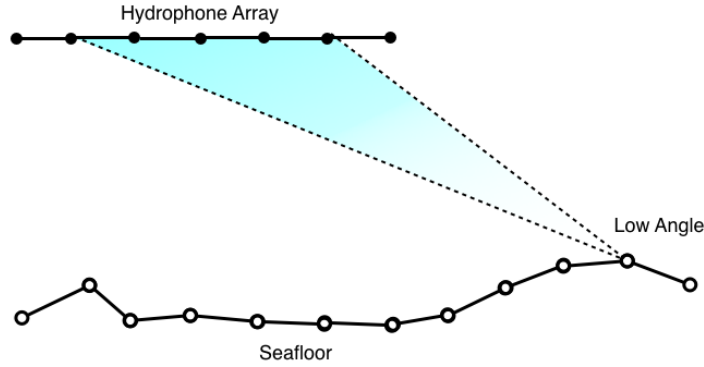


Figure 2.10: A non-specular return to the hydrophone array

case, we obtain low-amplitude returns over a long time period, with the angular difference between the first and last returns for that beam easily differentiated by the difference in time between the returns.

The second method, Weighted Mean Time (WMT), attempts to first fix the TOA of the return accurately for a specific DOA. In this method we consider the information across all time slices within the ping cycle for each beam. Again, we apply thresholding and start and stop gates to the amplitude of the returns obtained using the FFT beamformer. Motion correction between time slices is applied by interpolating the shifting beam axes to obtain beams fixed across all time slices. The DOA is then taken as the beam axis, and the TOA is again computed as the amplitude-weighted mean of the valid returns for that beam. We can think of this as expecting a single return in each beam direction, and finding the TOA [Yang and Taxt 1997].

This method performs best when the echo is *specular*, implying a return from near to the nadir as shown in Figure 2.11. These returns will have high amplitudes, but there will be very little difference in the TOA across each beam. The returns generated by both methods can be computed simultaneously for each beam, and selected between based on the grazing angle of the beam.

Once we have a DOA and a TOA for each beam, we can compute a *sounding* (a depth estimate at a georeferenced location). We first translate the ship-centred DOA into an earth-referenced bearing by correcting for the ship’s attitude. Intuitively, we may expect that the TOA (the delay between the ping and the return) will give us the range, and we can simply combine the DOA and TOA to calculate a sounding. However, the velocity of sound in water varies with salinity, temperature and pressure (discussed in Section 2.2.1).

While we may sample the ocean to arbitrary depths at a single point, it is clearly impossible to know the velocity of sound at every point in the volume of interest. We thus assume that the point sample is representative of the area of interest, and use it to construct a Sound Velocity Profile (SVP), an estimated model of how the speed of sound varies with depth. A common method for using the SVP to calculate a sounding is ray tracing. The SVP is first discretised into layers of constant sound velocity. Soundwaves, represented as rays, are traced from a known DOA through

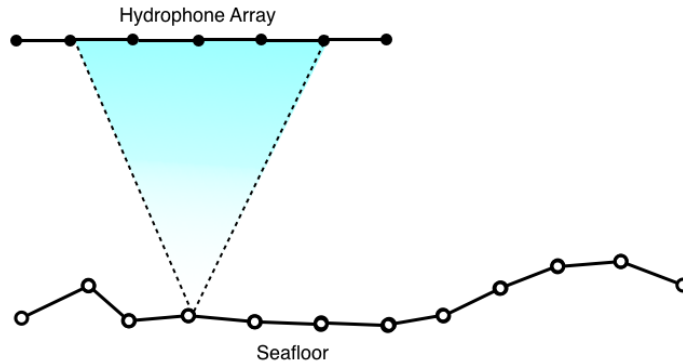


Figure 2.11: A specular return to the hydrophone array

the various layers of the SVP, undergoing refractions calculated using Snell's law for each layer encountered [Waite 2002][pg 59]. Snell's law,

$$\frac{\cos \theta_1}{c_1} = \frac{\cos \theta_2}{c_2} = \frac{\cos \theta_3}{c_3},$$

and its relation to ray tracing, is illustrated in Figure 2.12, where a ray is traced through three layers of an SVP.

The ray is traced from the ship, refracting through the layers until a depth is reached that accounts for the TOA (taking into account the changes in velocity between each layer). The changes to the DOA are now turned into a bearing offset. This bearing offset can be georeferenced using the GPS coordinates of the ship, and a sounding is thus obtained.

Geng and Zielinski [1999] showed that continuous SVPs could be well-estimated by linear profiles, and in fact the bearing offset of echoes is similar for families of linear profiles. Thus, while an exact echo location may not be computed, a system with a fairly accurate estimation of the sound velocity profile will produce a robust bearing offset. Kammerer *et al.* [1998] presented an interesting problem wherein sonar measurements were taken in a mixture of fresh and sea water, creating refraction problems due to local variations in the sound speed. This was solved using empirical refraction correction coefficients.

### 2.3.5 Visualisation

Bathymetric data consisting of georeferenced soundings are ordinarily visualised as a bathymetric map (or seafloor chart). In single beam systems, while soundings could be dense along the track of the ship, the soundings produced were sparse across the tracks [de Moustier 1988], and depth maps were produced by estimating contour lines [Mayer 2006]. Human interaction was expected to inform the system. In multibeam systems, the central problem is the density of data [Calder and Mayer 2001], which may consist of contradictory soundings. It is unfeasible for a human operator to deal with every possible contradiction when a survey may consist of millions of soundings.

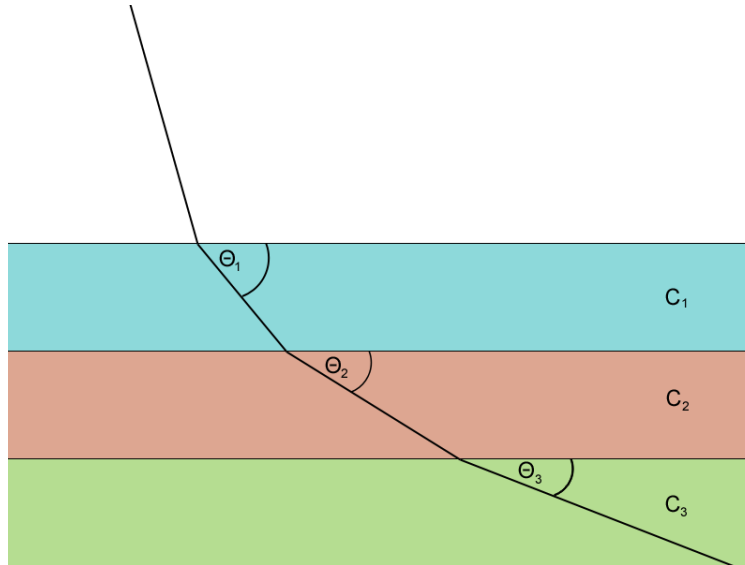


Figure 2.12: A ray refracts as it passes between layers with differing sound velocities

Ware *et al.* [1991] present statistical algorithms capable of filtering a bathymetric map based on a weighted average approach. Mitchell [1996] presents a system for the processing of Simrad multi-beam sonar data. This system incorporates data filtering and correction of backscatter strength for incidence angle, as well as computing a number of additional data products such as slope.

The Combined Uncertainty and Bathymetric Estimator (CUBE) system [Calder and Mayer 2001 2003; Calder 2003] provides a method for automatically gridding a collection of soundings, based on an estimated uncertainty. The error of each sounding is predicted based on the system's attitude, position and properties at the time of measurement. A grid is created whose nodes will be the estimation points of the final bathymetric map. The soundings, with their associated predicted errors are presented to the algorithm, which propagates soundings to neighbouring nodes in the grid. The depth hypotheses at each node are updated based on the information gathered from each sounding. Finally, the most likely depth hypothesis at each node is reported as the final estimated depth, together with its posterior variance. This approach is recommended for data fusion by Elmore and Steed [2008].

CUBE has another interesting use, which is cleaning and filtering soundings [Mallace and Robertson 2007] through user intervention. Yang *et al.* [2007] demonstrate a data cleaning technique utilising the density of soundings when seen 'side-on', and eliminating those soundings that contradict the bulk of the data.

## 2.4 Beamforming and Phased Arrays

### 2.4.1 Time-Delay Beamforming

We now examine time-delay beamforming in more detail. Recall from Section 2.3.3 that, if we take the far field assumption as valid, we can maximise the sensitivity of our hydrophone array to returns from the direction  $\theta$  by introducing a delay of  $\frac{d \sin \theta}{c}$  between array elements and summing the contributions across each array element. Thus, for a hydrophone array of  $L$  elements recording complex input signals  $x_k(t)$ , the total amplitude  $P_\theta(t)$  from direction  $\theta$  is

$$P_\theta(t) = \left| \sum_{k=1}^L x_k\left(t + k \frac{d \sin \theta}{c}\right) \right|.$$

An immediate limitation to this method can be shown by way of the sampling frequency. Suppose we sample our hydrophone at a rate  $f_s$ . Clearly, any delay we wish to introduce between array elements must be an integer multiple of the sampling period, otherwise we will sample the wavefront out of phase [Nielsen 1991][pg 71]. Thus, we obtain the following equation

$$\frac{d \sin \theta}{c} = \frac{m}{f_s} \tag{2.2}$$

for some  $m \in \mathbb{Z}$ . We can rearrange this equation to find those angles  $\theta$  for which this constraint holds as

$$\sin \theta = \frac{cm}{df_s}.$$

Taking as an example the speed of sound in water as  $1500ms^{-1}$ , a separation between hydrophone elements of  $10cm$  and a sampling frequency of  $10000hz$ , we see that we can only form beams where

$$\sin \theta = 1.5m$$

is satisfied by an integer  $m$ . Clearly this can only take place when  $m = 0$ , forming a beam directly below the ship. Intuitively this is a result of the sampling frequency not being high enough to catch the rapid propagation of the wave across the closely-spaced hydrophone elements in phase. We see that such time-delay beamformers are impractical even before taking into account issues of resolution and multiple signal estimation.

### 2.4.2 Phase Delays and Fourier Transforms

The next beamformer we shall examine avoids the sampling rate problem by introducing phase delays to the signal. Here, we assume that, given a single signal source, the same signal will impinge upon all elements of the hydrophone array with a difference in phase between each element. As before, we use the assumption that the source is sufficiently far away for the phase difference between hydrophone elements to be linear. If we express the complex signal  $x_k(t)$  recorded at

hydrophone element  $k$  as

$$x_k(t) = A_k(t)e^{i\Phi_k(t)},$$

where  $A_k(t)$  is the amplitude of the signal and  $\Phi_k(t)$  is a time-varying function giving the phase of the signal received by the hydrophone element, then we can express the expected phase difference between neighbouring hydrophone elements to be

$$\frac{2\pi}{\lambda}d \sin \theta$$

for a signal from direction  $\theta$ . Thus, the appropriately phase-shifted and summed signal for the hydrophone array is

$$P_\theta(t) = \sum_{k=1}^L A_k(t)e^{i(\Phi_k(t) + \frac{2\pi}{\lambda}kd \sin \theta)} = \sum_{k=1}^L x_k(t)e^{i\frac{2\pi}{\lambda}kd \sin \theta} \quad (2.3)$$

This type of delay-and-sum beamformer is also known as the *Bartlett* beamformer [Bartlett 1948] c.f. [Krim and Viberg 1996]. A fast implementation of this beamformer comes in the form of an FFT. We observe that equation 2.3 is similar in structure to that of the discrete Fourier Transform [L-3 2000]. If we equate the two, as in

$$\sum_{k=0}^N h_k e^{i\left(\frac{2\pi km}{N}\right)} = \sum_{k=1}^L x_k(t) e^{i\frac{2\pi}{\lambda}kd \sin \theta_m}$$

and take  $h_k = x_k$  and  $N = L$ , we see that a spatial FFT of the complex signals of the hydrophone array will result in beams formed at angles satisfying

$$\theta_m = \sin^{-1} \left( \frac{\lambda m}{dL} \right) \quad (2.4)$$

for some integer  $m$ .

This is used by L-3 [2000] and many other sonar systems as it provides realtime beamforming capability. Unlike the time delay beamformer, we are not limited by the hardware sampling rate, and can in fact steer beams to arbitrary angles using equation 2.3. The FFT beamformer, however, is limited to angles satisfying equation 2.4.

Taking as an example  $d = \frac{\lambda}{2}$ , and choosing  $L = 10$  we can form beams at the angles satisfying

$$\theta_m = \sin^{-1} \left( \frac{m}{5} \right)$$

which are given in Table 2.1.

An important limitation of this method comes in the form of its angular resolution. While it may appear that we can steer beams to arbitrary angles, and therefore should not encounter resolution difficulties, this beamformer cannot distinguish between signal sources spaced less than a beamwidth apart [Krim and Viberg 1996; Tian *et al.* 2009].



m	Angle
-5	-1.5708
-4	-0.9273
-3	-0.6435
-2	-0.4115
-1	-0.2014
0	0
1	0.2014
2	0.4115
3	0.6435
4	0.9273
5	1.5708

Table 2.1: The angles of beams formed by an FFT for  $L = 10$

### 2.4.3 Interferometry

Interferometry is another method for estimating DOAs using hydrophone arrays. Interferometric techniques were the focus of Pujol [2007] (with further work appearing in Pujol *et al.* [2008] and Pujol *et al.* [2010]), and form an interesting contrast to standard and high resolution beamforming techniques. The interferometric method relies on measuring the phase difference between two closely spaced receivers (or arrays) steered to a specific angle  $\theta_s$ , and detecting when that phase difference is zero, at which point we know the direction of arrival of the signal matches the steering angle. While many examples in the literature use two subarrays, Yang and Tait [1997] extend this to multiple subarrays.

One of the central problems of interferometry is phase difference disambiguation, since the phase difference is truncated between  $-\pi$  and  $\pi$  [Pujol 2007][pg 32]. While interferometry is a highly interesting technique, and the focus of much research, it will not form part of this project as interferometric sonar systems are said to produce higher quality backscatter imagery, but inferior bathymetry when compared to traditional multibeam systems [Mayer 2006].

## 2.5 High Resolution Beamforming

High resolution methods were created to address the problems encountered by conventional beamformers, whose angular resolution is directly linked to the number of elements in the hydrophone array. It is stated by Bienvenu and Kopp [1983] that the improvements in resolution of these methods are due to a more accurate estimation of the noise field.

We begin this discussion through an examination of the assumptions made in high resolution methods. This discussion will be limited to the context of uniform linear hydrophone arrays, although many of the concepts and beamformers are applicable to other contexts (such as radar) and arbitrary array geometries. We will also limit this discussion to narrowband beamformers. Chrisofidakis *et al.* [2008] characterises the difference between narrowband and broadband beamformers as follows: ‘If the performance of the beamformer, as expressed by the direction of transmission, remains unchanged for a broad range of frequencies then the beamformer is termed as broadband. On the contrary, if the direction of transmission changes with small variations of the frequency, the beamformer is called narrowband.’

As we saw in Section 2.4.2, the steering techniques used in sonar beamformers rely on phase shifts. Small variations in frequency will introduce changes into the steering vectors. Unless otherwise stated, material in this Section is derived from Krim and Viberg [1996], a survey of high resolution methods.

### 2.5.1 The Signal Model

Recall from Section 2.4.2 that if we wish to steer a uniform linear array of  $L$  hydrophone elements to maximise sensitivity in a specific direction  $\theta$  we should introduce a phase delay of  $\frac{2\pi}{\lambda}d \sin \theta$  between neighbouring hydrophone elements. Suppose a single signal  $s(t)$  impinges on the hydrophone array from direction of arrival  $\theta$ . Then, the output of the array,  $\vec{x}(t)$ , is given by

$$\vec{x}(t) = \vec{a}(\theta)s(t)$$

where

$$\vec{a}(\theta) = \left[ 1, e^{i\frac{2\pi}{\lambda}d \sin \theta}, \dots, e^{i(L-1)\frac{2\pi}{\lambda}d \sin \theta} \right]$$

is called the *steering vector*. The steering vector encodes the array geometry and thus wavefront shape [Bienvenu and Kopp 1983]. If  $M$  signals impinge on the linear array, then by the superposition principle the output of the array is given by

$$\vec{x}(t) = \sum_{m=1}^M \vec{a}(\theta_m)s_m(t) + n(t) = \mathbf{A}(\vec{\theta})s(t) + \vec{n}(t) \quad (2.5)$$

where

$$\mathbf{A}(\vec{\theta}) = \mathbf{A} = [\vec{a}(\theta_1), \dots, \vec{a}(\theta_M)]$$

and  $\vec{n}(t)$  is an additive ambient noise field assumed independent of the signals and their directions of arrival. We make the assumption that  $M < L$ , otherwise the noise field will not be solvable [Bienvenu and Kopp 1983]. In the sonar bathymetry context, this implies that at any given moment

the array is receiving fewer returns than there are array elements. This is a reasonable assumption to make, given that in a typical modern multibeam system,  $L > 50$  and typically (for a reasonably flat seafloor)  $M \sim 2$ .

We now define the spatial autocovariance matrix  $\mathbf{R}$ . If exact quantities and infinite observation times are used, this is defined as

$$\mathbf{R} = E \{ \vec{x}(t) \vec{x}^H(t) \} = \mathbf{A} E \{ \vec{s}(t) \vec{s}^H(t) \} \mathbf{A}^H + E \{ \vec{n}(t) \vec{n}^H(t) \} \quad (2.6)$$

where  $x^H$  denotes the conjugate transpose of  $x$ . We define the source covariance matrix  $\mathbf{P}$  as

$$E \{ \vec{s}(t) \vec{s}^H(t) \} = \mathbf{P}$$

and as the noise field is assumed to be incoherent and thus uncorrelated between sensors, the noise covariance matrix is given by

$$E \{ \vec{n}(t) \vec{n}^H(t) \} = \sigma^2 \mathbf{I}.$$

If the noise field is not spatially white, and is such that

$$E \{ \vec{n}(t) \vec{n}^H(t) \} = \sigma^2 \mathbf{J}$$

with  $\mathbf{J}$  known, we can find a transform matrix  $\mathbf{C}$  such that

$$\mathbf{C} \mathbf{J} \mathbf{C}^H = \mathbf{I}$$

to spatially whiten the noise field [Bienvenu and Kopp 1983].

Using the above, we can see that  $\mathbf{R}$  can be written as

$$\mathbf{R} = \mathbf{A} \mathbf{P} \mathbf{A}^H + \sigma^2 \mathbf{I}. \quad (2.7)$$

Typically,  $\mathbf{R}$  must be estimated using a finite number of samples. In the context of passive sonar, radio astronomy and others multiple samples are available, as stationarity is assumed [Bienvenu and Kopp 1983]. In the case of active sonar, the DOA of the received signals will be different from one time instant to the next, as the echoes originate from the moving ping wavefront bouncing off the ocean floor. Thus, we only have one observation to work with. In the remainder of this Section, we will use  $\mathbf{R}$  to denote the estimate of the spatial covariance matrix for one time sample, with discussion in Section 2.5.8 regarding how this estimate is obtained.

The dependence of each parameter on time will be taken as implied, as each parameter will be estimated for a specific time instant.

## 2.5.2 Conventional Beamforming

For some weighting vector  $\vec{w}$  we define the *power spectral estimation*  $P(\vec{w})$  of the array output under the weighting  $\vec{w}$  as

$$P(\vec{w}) = \vec{w}^H \mathbf{R} \vec{w} \quad (2.8)$$

If  $\vec{w}$  is chosen such that it is a normalised steering vector, then we may think of  $P$  as the power received by the array from the direction of the steering vector, to some constant factor.

Using equation 2.8 and taking

$$\vec{w}_B = \frac{\vec{a}(\theta)}{\sqrt{\vec{a}^H(\theta) \vec{a}(\theta)}}$$

we can rewrite the Bartlett beamformer as the power spectrum estimator

$$P_B(\theta) = \frac{\vec{a}^H(\theta) \mathbf{R} \vec{a}(\theta)}{\vec{a}^H(\theta) \vec{a}(\theta)},$$

which is the amplitude of the phase-shifted signal normalised by the direction gain.

To use this beamformer, we would compute  $\mathbf{R}$ , and find  $P_B(\theta)$  across a set grid of  $\theta$  values. The resolution achieved by this beamformer is still explicitly dependent on the number of elements within the array.

Capon's beamformer is another conventional beamformer, and is defined by the minimisation of the power spectrum

$$\min_w P(\vec{w}) \quad (2.9)$$

$$\text{subject to } \vec{w}^H \vec{a}(\theta) = 1$$

which can be interpreted as minimising the power contribution outside the look direction  $\theta$  caused by other signals and the noise field while fixing the gain in the look direction through the constraint [Capon 1969] c.f. [Krim and Viberg 1996]. The solution to equation 2.9 can be obtained through Lagrangian minimisation as

$$\vec{w}_{\text{capon}} = \frac{\mathbf{R}^{-1} \vec{a}(\theta)}{\vec{a}^H(\theta) \mathbf{R}^{-1} \vec{a}(\theta)}$$

giving

$$P_{\text{capon}}(\theta) = \frac{1}{\vec{a}^H(\theta) \mathbf{R}^{-1} \vec{a}(\theta)}.$$

This is an estimation of a true power spectrum with fixed gain. It provides better resolution than the Bartlett beamformer, but requires inversion of  $\mathbf{R}$  at each timestep. It should be noted that if  $\mathbf{R}$  is rank deficient due to coherent signals or a lack of samples, it will not be invertible. [Li *et al.* 2005] discusses the use of the Capon beamformer extensively in the context of a known DOA - here, the goal is to suppress interference from other signals impinging on the array.

### 2.5.3 The High Resolution Approach

Consider now the eigenstructure of  $\mathbf{R}$ ,

$$\mathbf{R} = \mathbf{A}\mathbf{P}\mathbf{A}^H + \sigma^2\mathbf{I} = \mathbf{U}\mathbf{\Lambda}\mathbf{U}^H.$$

Any vector orthogonal to  $\mathbf{A}$  will be an eigenvector of  $\mathbf{R}$  (and thus a column of  $\mathbf{U}$ ) with eigenvalue  $\sigma^2$ .

$$\mathbf{R} = \mathbf{A}\mathbf{P}\mathbf{A}^H + \sigma^2\mathbf{I} = \mathbf{U}_s\mathbf{\Lambda}_s\mathbf{U}_s^H + \sigma^2\mathbf{U}_n\mathbf{U}_n^H$$

where  $\mathbf{\Lambda}_s$  is a diagonal matrix containing the  $M$  largest eigenvalues of  $\mathbf{A}\mathbf{P}\mathbf{A}^H$ , and  $\mathbf{U}_s$  and  $\mathbf{U}_n$  are orthonormal eigenvectors spanning the signal and noise subspaces of  $\mathbf{R}$  respectively. In practice, given an estimate of the noise variance  $\sigma^2$ , the signal subspace will in fact contain both signal and noise (as the noise is present in all dimensions). The difference between the two subspaces is that the noise subspace contains *only* noise.

We also find in practice that noise eigenvalues are not identically  $\sigma^2$  for finite observation times, and so the eigenstructure of  $\mathbf{R}$  is in fact

$$\mathbf{R} = \mathbf{U}_s\lambda_s\mathbf{U}_s^H + \mathbf{U}_n\lambda_n\mathbf{U}_n^H$$

with  $\lambda_n$  tending to  $\sigma^2\mathbf{I}$ .

High resolution methods are so named as their resolution is not directly dependent on the number of elements within the hydrophone array. They take advantage of one of two properties of the eigenstructure of  $\mathbf{R}$ . The first property is that the columns of  $\mathbf{A}$  and the eigenvectors of the signal subspace  $\mathbf{U}_s$  span the same space, that is

$$\mathbf{Span}\{\vec{a}(\theta_1), \dots, \vec{a}(\theta_m)\} = \mathbf{Span}\{\vec{u}_1, \dots, \vec{u}_m\}$$

where

$$\mathbf{U}_s = [\vec{u}_1, \dots, \vec{u}_m].$$

The second property is a consequence of the first, and that is that the columns of  $\mathbf{A}$  span the nullspace of  $\mathbf{U}_n$ . That is,

$$\mathbf{U}_n^H \vec{a}(\theta) = 0$$

for any  $\theta$  satisfying equation 2.5. This comes about as the columns of  $\mathbf{U}_s$  form a basis for the signal subspace, and thus any column of  $\vec{a}(\theta)$  of  $\mathbf{A}$  is expressible as a linear combination of this basis. However, each of these basis vectors is orthogonal to the eigenvectors that make up  $\mathbf{U}_n$ .

### 2.5.4 MUSIC

The Multiple Signal Classification (MUSIC) algorithm relies on the projector  $\mathbf{\Pi}_n$  onto the noise subspace spanned by  $\mathbf{U}_n$ . This projector is

$$\mathbf{\Pi}_n = \mathbf{U}_n \mathbf{U}_n^H.$$

We may then define the MUSIC measure [Bienvenu and Kopp 1980; Schmidt 1981] c.f. [Krim and Viberg 1996] as

$$P_m(\theta) = \frac{\vec{a}^H(\theta) \vec{a}(\theta)}{\vec{a}^H(\theta) \mathbf{\Pi}_n \vec{a}(\theta)}. \quad (2.10)$$

While equation 2.10 has a form similar to that of the spectral power estimators of the Bartlett and Capon beamformers, it is not a spectrum. It is instead the inversion of the normalised length of the projection of  $\vec{a}(\theta)$  onto the subspace spanned by  $\mathbf{U}_n$ . It is interesting to note that the estimator does not rely on the signal subspace  $\mathbf{U}_s$ , as this subspace is spanned by the columns of  $\mathbf{A}$ . While this may be disconcerting, we may rest assured that, due to the columnar independence of  $\mathbf{A}$ , we may find  $\theta$  uniquely within a sensible domain.

Ellingson and Cazemier [2003] suggests using the projector  $\mathbf{\Pi}_n$  (which is in fact equivalent to  $\mathbf{I} - \mathbf{A}(\mathbf{A}^H \mathbf{A})^{-1} \mathbf{A}^H$ ) within the context of radio astronomy to prefilter the array data as

$$\vec{x}_F(t) = \mathbf{\Pi}_n \vec{x}(t)$$

in order to introduce *nulls*, suppressing interference between signal sources. In their application, it is assumed that the number of signals, and their directions of arrival, are known. What one wants to compute then is the signal itself. This is at odds with active sonar, wherein the signal is known (it is simply a reflection of the ping signal), but the number of signals and their directions of arrival are unknown.

The MUSIC beamformer works well in applications with long sample times (recall that in active sonar we may only sample once) or high SNR. It may still fail to distinguish closely spaced signals in other scenarios.

There are many variations on the MUSIC method, including Weighted MUSIC, with a weighting matrix  $\mathbf{W}$  introduced in place of the eigenvalues as in

$$P_{wm}(\theta) = \frac{\vec{a}^H(\theta) \vec{a}(\theta)}{\vec{a}^H(\theta) \mathbf{\Pi}_n \mathbf{W} \mathbf{\Pi}_n^H \vec{a}(\theta)}.$$

According to Krim and Viberg [1996], a careful choice of weight can yield high-resolution estimates even in cases with limited samples and low SNR.

MUSIC is not a parametric method - rather, like the spectral methods, we use it to generate a pseudospectrum on a fixed grid of look directions, from which we must estimate soundings. This

is not the case with root-MUSIC. Root-MUSIC makes the assumption of a uniform linear array, and uses a rooting procedure to find DOA estimates, as the values of  $\theta$  satisfying the MUSIC spectrum are the zeros of  $\mathbf{U}_n^H \vec{a}(\theta)$  [Barabell 1983] c.f. [Krim and Viberg 1996]. Suppose we define a polynomial  $p(z)$  as

$$p_l(z) = [1, z, \dots, z^{L-1}] \vec{u}_l$$

where  $\vec{u}_l$  is the  $l$ th eigenvector of  $\mathbf{U}_n$ . We observe that this polynomial has roots at  $z = e^{i\theta_m}$ . Let

$$v(z) = [1, z, \dots, z^{L-1}]^T$$

for notational convenience. We then define the MUSIC-like polynomial

$$p(z) = z^{L-1} v^T(z^{-1}) \mathbf{U}_n \mathbf{U}_n^H v(z).$$

$p(z)$  is a polynomial of degree  $2L-2$ , and the  $M$  roots with the greatest magnitude  $z_m, m = 1, \dots, M$  are related to the DOA estimates by

$$\theta_m = \cos^{-1} \frac{\lambda \arg(z_m)}{2\pi d}.$$

Krim and Viberg [1996] states that root-MUSIC has the same asymptotic properties as MUSIC, but performs better on small sample sizes in empirical tests.

### 2.5.5 Subspace Fitting

We now briefly examine the subspace fitting (SSF) approach. In this approach, we attempt to find model parameters  $\vec{\theta}$  and  $\sigma^2$  that give subspaces with the properties expected of the signal and noise subspaces [Stoica and Sharman 1990] c.f. [Krim and Viberg 1996]. We consider again the eigenanalysis of  $\mathbf{R}$  given by

$$\mathbf{R} = \mathbf{U}_s \lambda_s \mathbf{U}_s^H + \mathbf{U}_n \lambda_n \mathbf{U}_n^H.$$

We note that  $\mathbf{I} = \mathbf{U}_s \mathbf{U}_s^H + \mathbf{U}_n \mathbf{U}_n^H$  (since  $\mathbf{U} = \mathbf{U}_s + \mathbf{U}_n$  are orthonormal eigenvectors) and also that  $\mathbf{I} = \mathbf{U}_s^H \mathbf{U}_s$ . Thus,

$$\mathbf{R} = \mathbf{A} \mathbf{P} \mathbf{A}^H + \sigma^2 (\mathbf{U}_s \mathbf{U}_s^H + \mathbf{U}_n \mathbf{U}_n^H) = \mathbf{U}_s \mathbf{\Lambda}_s \mathbf{U}_s^H + \sigma^2 \mathbf{U}_n \mathbf{U}_n^H$$

and so

$$\mathbf{A} \mathbf{P} \mathbf{A}^H + \sigma^2 \mathbf{U}_s \mathbf{U}_s^H = \mathbf{U}_s \mathbf{\Lambda}_s \mathbf{U}_s^H.$$

Post-multiplying by  $\mathbf{U}_s$  yields

$$\mathbf{A} \mathbf{P} \mathbf{A}^H \mathbf{U}_s + \sigma^2 \mathbf{U}_s = \mathbf{U}_s \mathbf{\Lambda}_s$$

or

$$\mathbf{U}_s = \mathbf{A} \mathbf{T}$$

where  $\mathbf{T} = \mathbf{P}\mathbf{A}^H\mathbf{U}_s(\mathbf{\Lambda}_s - \sigma^2\mathbf{I})^{-1}$ . Since  $\mathbf{R}$  (and thus  $\mathbf{U}_s$ ) is an estimate, there is no  $\vec{\theta}$ ,  $\mathbf{T}$  that will solve this equation. We thus attempt to minimise the distance between  $\mathbf{U}_s$  and  $\mathbf{A}\mathbf{T}$  (with respect to the Frobenius norm)

$$\min_{\vec{\theta}, \mathbf{T}} \|\mathbf{U}_s - \mathbf{A}\mathbf{T}\|_F^2$$

For a fixed, unknown  $\mathbf{A}$ , we can solve  $\mathbf{T}$  as  $\mathbf{T} = \mathbf{A}^G\mathbf{U}_s$ , where  $\mathbf{A}^G = (\mathbf{A}^H\mathbf{A})^{-1}\mathbf{A}^H$  is the left pseudoinverse of  $\mathbf{A}$ , the existence of which is dependent on the columns of  $\mathbf{A}$  being linearly independent. This leads to the objective function

$$\min_{\vec{\theta}} \text{Tr}\{(\mathbf{I} - \mathbf{A}\mathbf{A}^G)\mathbf{U}_s\mathbf{\Lambda}_s\mathbf{U}_s^H\}.$$

Performing multidimensional optimisation of  $\vec{\theta}$  with respect to this function will lead to a simultaneous estimate of the DOAs of all the signals impinging on the array.

Several variations on the SSF method exist, such as the use of weighting matrices, or use of the noise subspace. In the Weighted Subspace Fitting (WSF) scheme, the eigenvalues  $\mathbf{\Lambda}_s$  are replaced with a weighting matrix  $\mathbf{W}$  giving

$$\vec{\theta} = \arg\{\min_{\vec{\theta}} \text{Tr}\{(\mathbf{I} - \mathbf{A}\mathbf{A}^G)\mathbf{U}_s\mathbf{W}\mathbf{U}_s^H\}\}.$$

It is then necessary to choose a weighting matrix that will increase the accuracy of the method. [Viberg *et al.* 1991] c.f. [Krim and Viberg 1996] gives

$$\mathbf{W} = (\mathbf{\Lambda}_s - \sigma^2\mathbf{I})^2\mathbf{\Lambda}_s^{-1}$$

where  $\sigma^2$  is an estimate of the noise power level as an appropriate weight. The maximum likelihood estimate of the noise power  $\sigma^2$  for finite samples is given by

$$\sigma^2 = \frac{1}{L - M} \sum_{i=M+1}^L \lambda_i,$$

that is, the average of the  $L - M$  smallest eigenvalues [Bienvenu and Kopp 1983]. In [Kritchman and Nadler 2008] this is referred to as the *real error function*.

This leads to the objective function

$$\min_{\vec{\theta}} \text{Tr}\{(\mathbf{I} - \mathbf{A}\mathbf{A}^G)\mathbf{U}_s(\mathbf{\Lambda}_s - \sigma^2\mathbf{I})^2\mathbf{\Lambda}_s^{-1}\mathbf{U}_s^H\}$$

which, as before, will yield the DOAs via optimisation.



### 2.5.6 ESPRIT

ESPRIT (Estimation of Signal Parameters via Rotational Invariance Techniques) is another subspace fitting algorithm [Roy and Kailath 1989] c.f. [Krim and Viberg 1996]. In contrast with SSF and WSF, ESPRIT is specifically for uniform linear arrays, and is more computationally efficient.

We note that, as in SSF,

$$\mathbf{U}_s = \mathbf{A}\mathbf{T}$$

with  $\mathbf{T}$  defined as in the previous Section. Now, define  $\mathbf{A}_1$  by removing the last row of  $\mathbf{A}$ , and similarly,  $\mathbf{A}_2$  by removing the first row of  $\mathbf{A}$ .  $\mathbf{A}_1$  and  $\mathbf{A}_2$  are related by

$$\mathbf{A}_2 = \mathbf{A}_1\mathbf{\Phi}$$

where  $\mathbf{\Phi}$  is a diagonal matrix with diagonal entries (and thus eigenvalues)  $e^{i\theta_m}$  for  $m = 1, \dots, M$ . Now,

$$\mathbf{U}_1 = \mathbf{A}_1\mathbf{T}$$

and

$$\mathbf{U}_2 = \mathbf{A}_2\mathbf{T}$$

where  $\mathbf{U}_1$  and  $\mathbf{U}_2$  are obtained from the signal subspace  $\mathbf{U}_s$  by deleting the last and first rows respectively. From these equations, we find that

$$\mathbf{U}_2 = \mathbf{A}_1\mathbf{\Phi}\mathbf{T}$$

and so by setting  $\mathbf{\Psi} = \mathbf{T}^{-1}\mathbf{\Phi}\mathbf{T}$ , we find that

$$\mathbf{U}_2 = \mathbf{U}_1\mathbf{\Psi}.$$

Since  $\mathbf{\Psi}$  and  $\mathbf{\Phi}$  are related by a similarity transform, they have the same eigenvalues. The problem of computing the DOAs thus reduces to computing  $\mathbf{U}_1$  and  $\mathbf{U}_2$ , finding  $\mathbf{\Psi}$ , and computing its eigenvalues. The eigenvalues (say,  $q_m$ ) are related to the DOAs via the formula

$$\theta_m = \cos^{-1} \frac{\lambda \arg(q_m)}{2\pi d}.$$

### 2.5.7 Signal Enumeration

Signal enumeration is the problem of estimating the number of signals impinging on the array. For high resolution beamforming methods, this is a crucial problem, as partitioning into signal and noise subspaces requires knowledge of the size of the signal subspace. Recall from Section 2.3.1 that as the number of samples used to estimate the covariance matrix  $\mathbf{R}$  tends to infinity, so the eigenvalues corresponding to the noise subspace will converge to  $\sigma^2$  with probability one [Kritchman and Nadler 2008]. For finite samples, these eigenvalues will be distinct, with a spread that grows as the sample size is reduced [Bienvenu and Kopp 1983].

It would seem then that all one has to do is find the set of eigenvalues ‘close to’ the noise power  $\sigma^2$ , and take any larger eigenvalue as belonging to the signal subspace. Kotanchek and Dzielski

[1996] warn against using ad-hoc criteria, mentioning two related information-theoretic signal enumeration approaches, namely Minimum Description Length (MDL) and the Akaike Information Criterion (AIC). There is a warning that within the context of sonar signal processing, the assumptions inherent in these criteria may not be applicable. These two methods are highly sensitive to the assumption of a spatially white noise field [Krim and Viberg 1996].

Formulae for AIC and MDL are given in [Pujol 2007][pg 217] for the case of zero-mean Gaussian processes. They are

$$AIC(k) = -2(L - k)N \log \left( \frac{\prod_{i=k+1}^L \lambda_i^{\frac{1}{L-k}}}{\frac{1}{L-k} \sum_{i=k+1}^L \lambda_i} \right) + 2k(2L - k) \quad (2.11)$$

where  $N$  is the number of samples used to estimate  $\mathbf{R}$ ,  $\lambda_i$  are the eigenvalues of  $\mathbf{R}$  in descending order and  $\mathbf{R}$  is of size  $L \times L$ . MDL is similarly given by

$$MDL(k) = -(L - k)N \log \left( \frac{\prod_{i=k+1}^L \lambda_i^{\frac{1}{L-k}}}{\frac{1}{L-k} \sum_{i=k+1}^L \lambda_i} \right) + \frac{k}{2}(2L - k) \log N. \quad (2.12)$$

The estimated number of signals  $M$  is then the value of  $k$  that minimises either equation, with  $0 \leq M < L$ .

Kritchman and Nadler [2008] gives a statistical method for determining  $M$ , based on Random Matrix Theory (RMT), wherein the distribution of the eigenvalues of random matrices are studied. The KN rank estimation method tests possible values of  $k$  by assuming  $\lambda_{k+1} \dots \lambda_L$  are noise eigenvalues and testing the possibility that  $\lambda_k$  arises from a signal by examining

$$\lambda_k > \sigma_{KN}^2(k) (\mu_{L-k} + s(\alpha)\sigma_{L-k})$$

where  $\sigma_{KN}^2(k)$  is an estimate of the noise power level and  $(\mu_{L-k} + s(\alpha)\sigma_{L-k})$  is an expression which converges to the complex-valued Tracy-Widom distribution with confidence  $\alpha$ . If we accept that  $\lambda_k$  is a signal eigenvalue, the number of signals  $M$  is increased by one.

Ronhovde [1999][pg 46] gives an engineering method for determining the number of signals. One computes the mean  $\mu$  and standard deviation  $\sigma$  of the six largest eigenvalues of  $\mathbf{R}$ . The estimated number of signals  $M$  starts as zero. One then compares the four largest eigenvalues to  $d$ , given by

$$d = 0.95\mu - 0.38\sigma.$$

$M$  is increased by one for each eigenvalue larger than  $d$ . Ronhovde [1999] states that this method is not based on a statistical procedure.

### 2.5.8 Covariance Matrix Estimation

In the event that we obtain multiple time samples  $\vec{x}(t_i)$  (say,  $N$  of them) from which we wish to estimate the autocovariance matrix  $\mathbf{R}$ , we may do so with

$$\mathbf{R} = \frac{1}{N} \sum_{i=1}^N \vec{x}(t_i) \vec{x}(t_i)^H.$$

In an active sonar system, the ping is typically only sampled once or twice [Pujol 2007][pg 200], precluding such time averaging. It would seem then that with one time sample  $\vec{x}$ , we may find

$$\mathbf{R} = \vec{x} \vec{x}^H.$$

However, this leaves  $\mathbf{R}$  rank deficient (specifically, of rank one), and so an eigendecomposition of  $\mathbf{R}$  would yield one distinct nonzero eigenvalue.  $\mathbf{R}$  would also not be invertible. This means we may not use any high-resolution methods, or even Capon's beamformer.

Both Pujol [2007] and Ronhovde [1999] suggest the use of spatial smoothing to increase the rank of  $\mathbf{R}$ . Here, the array data  $\vec{x}$  is split into  $K$  overlapping subarrays of size  $L - K + 1$ . A covariance matrix  $\mathbf{R}_k$  is computed for each subarray, and the final smoothed estimate is given by

$$\mathbf{R}_f = \frac{1}{K} \sum_{k=1}^K \mathbf{R}_k.$$

This is known as *forward smoothing*, as we take subarrays in the same direction. A second method known as *forward-backward smoothing* is given by first computing the forward estimate  $\mathbf{R}_f$ , and then computing the backward estimate  $\mathbf{R}_b$  given by

$$\mathbf{R}_b = \mathbf{J} \mathbf{R}_f^H \mathbf{J}$$

where  $\mathbf{J}$  is a reversing permutation matrix. The final estimate  $\mathbf{R}$  is given by

$$\mathbf{R} = \frac{\mathbf{R}_f + \mathbf{R}_b}{2}. \tag{2.13}$$

This estimate has the property that the rank of  $\mathbf{R}$  increases by one with probability one for each additional subarray used [Pujol 2007][pg 202]. Since each additional subarray also reduces the size of  $\mathbf{R}$  by one, the *rank deficiency* of  $\mathbf{R}$  is decreased by two. Using this technique,  $\mathbf{R}$  can be made full rank, even for a single time sample. The size of  $\mathbf{R}$  is decreased from  $L$  to  $L - K + 1$ , which will decrease the accuracy of techniques explicitly reliant on the array length, such as the Bartlett beamformer.

Working with a single time sample, we may then find the minimum  $K$  such that  $\mathbf{R}$  is brought to full rank. The rank of  $\mathbf{R}$  using  $K$  subarrays is  $K$ , while its size is  $L - K + 1$ . We require then  $K$  such that

$$K \geq L - K + 1$$

and so

$$K = \left\lceil \frac{L+1}{2} \right\rceil.$$

For  $L = 81$  in particular (as used in this project), we require  $K = 41$ .

## 2.6 Overview

Sonar is used as a remote sensing tool in water as radar and light do not propagate through deep seas, while sound can propagate through kilometers of water with little attenuation (see Section 2.2) [Waite 2002]. In order to produce a sounding, it is necessary to obtain an array response in a specific direction in a process known as beamforming (Section 2.3.3). The combination of direction of arrival and time of arrival can be used to produce a depth estimate.

Conventional beamforming via phase-shifting (such as the Bartlett and Capon methods of Section 2.5.2) produces a power spectrum estimate. The dependence on the array length of the resolution of conventional beamforming methods is considered a disadvantage [Krim and Viberg 1996].

The high resolution approach (Section 2.5.3) differs from conventional beamforming through the use of an eigenanalysis of the autocovariance matrix. This allows a resolution independent of the array length [Krim and Viberg 1996]. MUSIC, root-MUSIC, SSF, WSF and ESPRIT are all considered in this research, covering both noise and signal subspace-based methods.

In order to use the high resolution approach, one must obtain an estimate of the autocovariance matrix (Section 2.5.8). Due to issues with rank deficiency, this must be obtained via spatial smoothing of the hydrophone array data. In this research, forward- and forward backward-smoothing are considered. Signal enumeration must be used to split the eigenvalues into those corresponding to signal and noise (Section 2.5.7).

In addition to this, some beamforming methods require estimation of the noise power level. This may be obtained via the noise eigenvalues. It may then be possible to correct for noise using out-of-envelope measurements of the pure noise field.

The question of which method combinations provide the best bathymetric estimates (that is, the most accurate and highest resolution) for active sonar has not been fully addressed in the literature.

## Chapter 3

# Methodology

### 3.1 Introduction

In Chapter 2, sonar bathymetry using linear arrays was discussed. From this, conventional spectral beamforming (namely, the Bartlett and Capon beamformers) and high resolution pseudospectral (MUSIC) and parametric (root-MUSIC, SSF, WSF, ESPRIT) techniques were highlighted. Various parameter estimation techniques were also discussed.

In this Chapter, the research methodology will be discussed. The research problem discussed in Chapter 1 will be more formally defined in Section 3.2. Guided by the material presented in Chapter 2 and this problem definition, we then formulate hypotheses in Section 3.3. The methodology used to test these hypotheses is given in Section 3.4.

### 3.2 Problem Definition

We now precisely define the problem. Currently, a standard SIMRAD sonar system is employed by Nautilus to map possible SMS deposit sites in the Solwara region of Papua New Guinea at an approximate depth of  $2km$ . At this depth, the system generates bottom profiles with a roughly  $25m$  resolution. This is too large to find individual SMS chimneys, which indicate the presence of an SMS deposit. These chimneys are approximately  $1m$  across. Our aim then is to improve the accuracy and resolution of the sonar system through high resolution beamforming and noise cancellation to facilitate the detection of the SMS deposits.

### 3.3 Research Hypothesis

We delineate the scope of this research with the following hypotheses.

1. A model of the noise field can be estimated using out-of-envelope measurements. We can then correct incoming signals for both structured and incoherent noise to obtain more accurate soundings.

2. An appropriate signal subspace cutoff threshold can be chosen through information theoretic methods.
3. A bathymetric profile with a better resolution and higher accuracy than that of the Bartlett beamformer can be obtained through correction for noise and high resolution techniques.

## 3.4 Methodology

### 3.4.1 Covariance Estimation

The high resolution approach requires estimation of the covariance matrix. For  $N$  samples, the covariance matrix  $\mathbf{R}$  can be robustly estimated by  $\mathbf{R} = \frac{1}{N} \sum_{i=1}^N \vec{x}_i \vec{x}_i^H$ . As we are limited to one time sample by the nonstationary nature of active sonar, we must spatially smooth our estimate of the covariance matrix in order to bring it to full rank.

Two different covariance matrix spatial smoothing techniques were tested in this research, namely forward smoothing (F-smoothing) and forward-backward smoothing (FB-smoothing). As all the data sets involved in this research simulate a hydrophone array with 81 elements, it is necessary to use 41 subarrays (each then of size 41) to bring each covariance matrix estimate to full rank.

### 3.4.2 Noise Field Estimation

Before the first echo returns, our hydrophones sample the noise field in all directions for a number of time instants, outside of the envelope of interest [Ronhovde 1999][pg 27]. We intend to use these pure noise samples to estimate structured noise sources (that is, persistent signal sources that do not correspond to the ping event) as well as estimating the strength of the random environmental noise.

As structured noise is assumed to be persistent, we may use the entire out-of-envelope sampling period to cancel random noise and isolate persistent noise sources. This may be done using high resolution methods, estimating the number of persistent noise signals, the DOA of those signals and their strengths. We may then correct our in-envelope measurements to remove these persistent noise sources.

Persistent signal estimation will be accomplished by estimating the covariance matrix  $\mathbf{R}_N$  for all time instants outside of the envelope, and performing signal enumeration on it. If the number of signals is estimated as  $m = 0$ , then no persistent signals are present. A robust estimate for the noise power level  $\sigma^2$  may be obtained from  $\mathbf{R}_N$  either via the signal enumeration technique (in the case of KN), or by averaging the non-signal eigenvalues (that is, the eigenvalues of the noise subspace).

Three noise cancellation procedures will be tested in this research. The first will be to leave the noise as-is, for comparative purposes. The second noise cancellation procedure will correct subsequent covariance matrix estimates by the  $\mathbf{R}_N$  obtained outside the envelope. That is, we will subtract the entire noise estimate, containing both structured and incoherent noise. This is the

method used by Ronhovde [1999][pg 27].

The third noise cancellation procedure will be a novel structured noise cancellation method whereby an estimate of  $\mathbf{R}_c = \mathbf{U}_s \lambda_s \mathbf{U}_s^H$  will be obtained from  $\mathbf{R}_N$  for cases where  $m$  is greater than zero outside the envelope.  $\mathbf{R}_c$  will then be subtracted from all subsequent estimates of  $\mathbf{R}$  in an attempt to correct for the structured noise.

### 3.4.3 Signal Enumeration

Signal enumeration is central to the concept of high-resolution beamforming. A number of signal enumeration techniques were covered in Section 2.5.7, namely AIC, MDL, KN rank estimation and the method of Ronhovde [1999]. To accurately test the second hypothesis of Section 3.3, the signal enumeration estimates of all four methods will be tested against data for which the exact number of signal sources is known.

Beamforming with selected methods will also take place, to test the effect of the signal enumeration methods on depth estimation accuracy. AIC, MDL and Ronhovde's method were implemented as per the formulae given in Section 2.5.7, while the KN rank estimation Matlab code of Kritchman and Nadler [2008] was used.

### 3.4.4 Beamforming

Bartlett, Capon, MUSIC, SSF and WSF beamformers were implemented in Matlab using formulae discussed in Chapter 2. The implementations of root-MUSIC and ESPRIT were those of Moses [2005], and modified slightly to fit the data processing chain of this research. These implementations can both be found at <http://www2.ece.ohio-state.edu/~randy/SAtext/>.

Bartlett and Capon are both conventional beamformers producing a power spectrum estimate for each sample. MUSIC is a pseudospectral high resolution method that, like the spectral methods, must be run on a grid. These three methods were run on a grid of 210 equally spaced angles between  $-\frac{\pi}{3}$  and  $\frac{\pi}{3}$ , unless otherwise indicated. For each sample presented to these three methods, a spectrum is produced across the grid.

Root-MUSIC, SSF, WSF and ESPRIT are parametric high resolution methods, using either the noise or signal subspaces to estimate the DOAs of incoming signals. Unlike the spectral methods, these methods produce the estimated DOAs as output. As SSF and WSF both require a potentially computationally expensive multidimensional global optimisation procedure, these methods were optimised using the DOAs of root-MUSIC as initial values.

### 3.4.5 Depth Profiling

The beamformers that produce spectra as results (namely, Bartlett, Capon and MUSIC) were subjected to three different depth-estimation techniques. The first depth estimation technique tested was in-envelope amplitude weighted mean time (WMT) calculation as described in Section 2.3.4 and computing a sounding (referred to as mean-amplitude beamforming), while the second consisted of simply taking the maximum in-envelope amplitude for each DOA to estimate the TOA, and computing a sounding (maximum amplitude beamforming).

The third method (referred to as peaks) is a simple novel hybrid approach taking advantage of the signal enumeration estimates to find the number of peaks in the spectrum at each time instant in order to estimate DOAs. This was done by finding those parts of the spectrum with amplitudes greater than their neighbours (in a neighbourhood of three values to either side), and selecting  $m$  of these candidates as the DOAs, where  $m$  is the estimated number of signals in the sample. Such estimates are ordinarily not available for the Bartlett and Capon beamformers, but it is instructive to see how they respond when they are available. The DOA estimates were processed in the same manner as the parametric beamformers, described below.

The depth estimates for the parametric beamformers were obtained by converting each in-envelope DOA into a sounding, and discarding all those outside the envelope. The accuracy of the depth profiles produced from these soundings was tested by measuring the mean of the absolute difference between the sounding and the true depth, together with the number of in-envelope soundings obtained. This was applied to all the parametric methods (root-MUSIC, SSF, WSF, ESPRIT), as well as the three depth estimation techniques applied to the spectral methods (Bartlett, Capon, MUSIC) for a total of 13 methods.

### 3.4.6 Data Sets and Simulation

Eight data sets will be used in this research. Each data set consists of noise-free array data for an 81 element hydrophone array. The data sets are described fully in Section 4.6. The two simulators developed to produce these data sets are the subject of Chapter 4.

### 3.4.7 Parameter Variation

The two covariance estimation methods, three noise cancellation schemes and four signal estimation schemes form a parameter space with 24 possible combinations. It was quickly found that the KN signal enumeration method could not be used in conjunction with full noise correction due to the underlying assumptions of that method, reducing the parameter space to 22 possible combinations.

Each parameter combination must be applied to all 13 beamforming methods and the eight data sets, across a variety of SNRs. The results are averaged across 5 runs to reduce the influence of random variation. Due to the large parameter space, we will use the signal enumeration results to select parameter combinations to investigate further.



## 3.5 Contributions

The primary contribution of this research is an examination of method combinations with respect to signal enumeration accuracy and depth profile accuracy through the use of simulated data. Ronhovde [1999] performed a comparison of some of the methods featured in this research on real data with metrics such as peak width. The use of real data without known ground truth means that it is impossible to compare the accuracy of the obtained depth profile.

The two simulators used to create the simulated data are also novel, although both are far simpler than commercial sonar simulators. The structured noise correction method and the peak-finding depth estimation method are both novel.

# Chapter 4

## Simulator

### 4.1 Introduction

To aid in the testing of this research, two simulators were created modeling a single ping cycle. While there are many commercial and military sonar simulators (such as the Sonar Simulation Toolset created by Robert Goddard, or the Multi-everything Sonar Simulator by B. La Cour, C. Collins and J. Landry, or the military targeting simulation discussed in Zhu and Sala-Diakanda [2007] and Zhu *et al.* [2008]) capable of simulating multibeam systems, none were available for use for this research. Systems such as the SAS simulator of Tarlet *et al.* [2007] may not be appropriate for multibeam simulation.

In Section 4.2, the mathematics and functioning of the first simulator are described. Section 4.3 then describes the scope of the simulator, focussing on the parameters that can be changed, and on the limitations of the simulator. The design, implementation and usage of the first simulator are outlined in Section 4.4. The second simulator developed for this project is described fully in Section 4.5. This simulator is far simpler than the first, representing an ideal ping that conforms exactly to the assumed data model. With this simulator, one may test signal enumeration procedures. The data sets generated for use in this research are presented in Section 4.6.

### 4.2 Simulator Function

#### 4.2.1 Wavefront Modelling

The wavefront is modelled using a collection of rays, traced from the projector source to the seafloor (as shown in Figure 4.1), and back to the hydrophone array. This ray tracing procedure means the curvature of the wavefront is maintained, even when dealing with depths such that the farfield assumption is reasonable. The projector source is assumed to lie at position  $k = 0$  of the hydrophone array.

The ping signal is modelled as a rectangular pulse, of arbitrary amplitude (as noise is measured relative to the signal power) and finite length. The length of the ping is chosen to be an integer multiple of the period greater than the time needed for a signal to propagate across the hydrophone

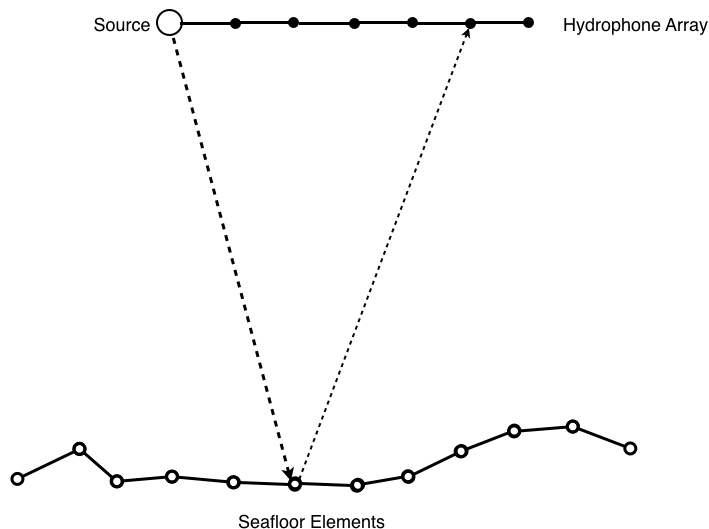


Figure 4.1: A ray from the projector strikes the seafloor and returns to the hydrophone array

array. The wavefront of the ping is two dimensional, travelling in the plane of the hydrophone array. We are thus distancing ourselves from the problem of projection.

#### 4.2.2 Seafloor and Ocean Modelling

The seafloor is modelled as a series of closely spaced point scatterers. The rays traced by the simulator are then from the source to a seafloor element, and back to a hydrophone element. Points between seafloor elements or hydrophone elements are not considered at all. It is assumed for this project that the seafloor is a perfect reflector.

The simulator allows for arbitrary seafloor profiles, but for the experiments the seafloor elements were equidistant (at a separation of  $dh$ ). The seafloor was simulated between  $-\frac{\pi}{3}$  and  $\frac{\pi}{3}$  to exclude extreme oblique beams. The simulator allows arbitrary depths for each seafloor element, but does not take into account occlusions - in order for the results to be physical, it must be possible for every element of seafloor to have a line of sight to every hydrophone.

The sea itself was modelled as having a constant sound velocity profile, with  $c$  taken as  $1500m/s$ . Arbitrary SVPs would complicate the ray tracing procedure, and were not considered as part of this project as we wish to test the effects of beamforming and associated procedures on depth estimation accuracy. The attenuation coefficient is a function of frequency, with Figures taken from Waite [2002][pg 47] as

$$\alpha = 0.05f^{1.4}$$

where  $f$  is a frequency between  $0.5kHz$  and  $100kHz$ . For frequencies greater than this, linear interpolation was used from the Table of Figures for attenuation in salt water at  $10^\circ C$  and a salinity of  $35ppt$ , also from Waite [2002][pg 47]. These are reproduced in Table 4.1.

Frequency	100 kHz	200 kHz	500 kHz
$\alpha$	35	60	125

Table 4.1: Attenuation Figures for 10°C salt water

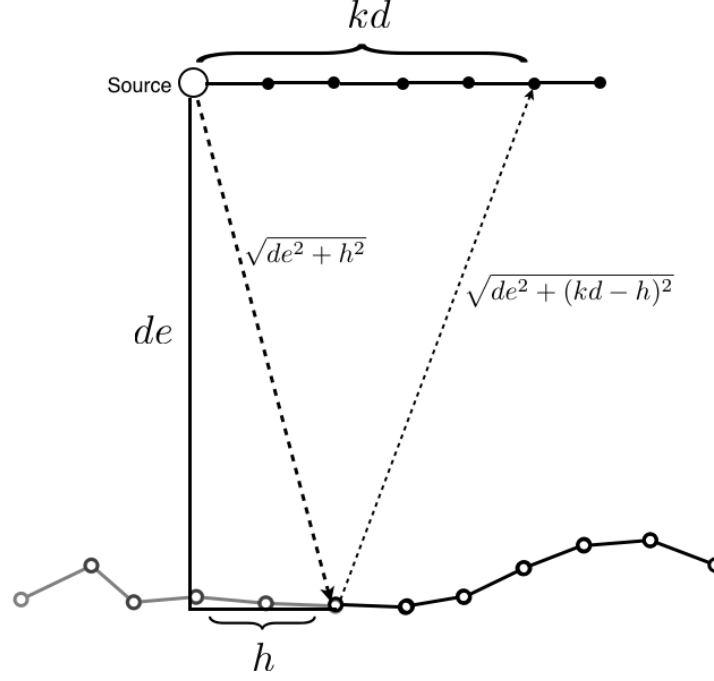


Figure 4.2: A ray from the projector reflects off a seafloor element and returns to the hydrophone array

### 4.2.3 Range Calculation

Assuming a constant sound velocity profile, the return time (or signal start time) of a single ray from the projector source to hydrophone  $k$  is given by

$$t_s(h) = \frac{\sqrt{de^2 + h^2}}{c} + \frac{\sqrt{de^2 + (kd - h)^2}}{c} \quad (4.1)$$

$$t_s(\theta) = \frac{de}{c \cos \theta} + \frac{\sqrt{de^2 + (kd - de \tan \theta)^2}}{c} \quad (4.2)$$

where  $h$  and  $\theta$  are the horizontal and angular offsets of the scattering point respectively,  $de$  is the depth,  $c$  is the speed of sound and  $d$  is the distance between hydrophone elements as shown in Figure 4.2. Note that a perfectly level uniform linear array of hydrophone elements is assumed. With this equation, the range (and thus return time of a ping) can be calculated for any part of the sea floor. We will identify each seafloor element by its offset  $h$ . We may also consider the depth to be a function of  $h$ .

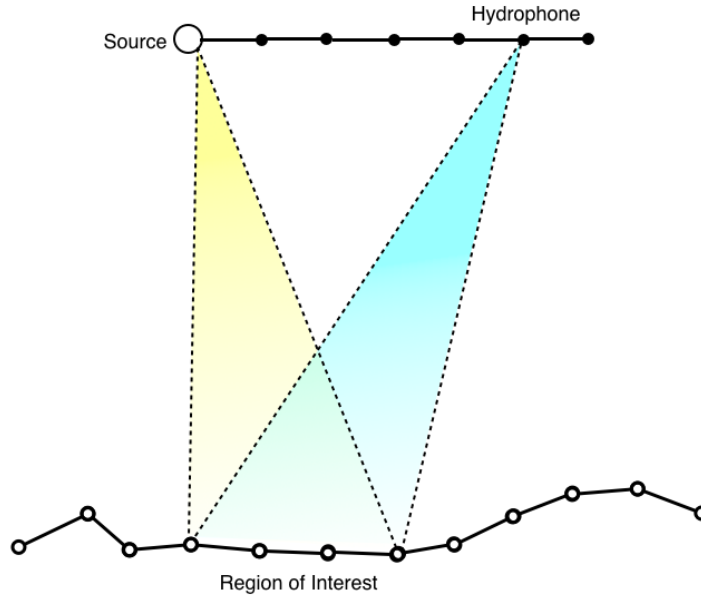


Figure 4.3: A hydrophone obtains a signal from a region of interest

Computing the range for each hydrophone and seafloor element pair, and dividing the results by  $c$  gives us the time at which a hydrophone  $k$  first receives a return from seafloor element  $h$ . These start times are stored in a matrix of start times, and form the basis of the simulator's computations.

#### 4.2.4 Hydrophone Array Signal Calculation

For each time instant (discretised by the hardware sampling frequency  $f_s$ ), and for each hydrophone  $k$ , we find the seafloor elements that hydrophone is receiving echoes from. This is done by isolating those seafloor elements where the current time is greater than the start time (read from the start time matrix), but less than the sum of the start time and ping length. The difference between the current time and the start time is the length of time the signal from that seafloor element has been received by hydrophone  $k$ . This time difference is used to compute the phase of the signal from each seafloor element in scope. The amplitude  $A$  of each element is computed as

$$A = I10^{-\alpha t_s c 10^{-4}}$$

where  $I$  is the initial intensity of the signal along that ray,  $\alpha$  is the attenuation coefficient for that frequency,  $t_s$  is the start time of that seafloor element, and  $c$  the speed of sound in water. This attenuation of amplitude does not take into account spreading losses. The amplitude and phase of each seafloor element in scope give the complex signal along that ray. The summation of all these signals gives the final signal recorded at that hydrophone element. This process is illustrated in Figure 4.3, wherein a single hydrophone obtains signals from a region of interest at a specific time.

This process is repeated for each hydrophone element, and for each time instant, until no more signals are received, which will take place at approximately  $t_s(\frac{\pi}{3}) + t_p$ . This gives a matrix of complex signals, for each time instant and hydrophone array element.

#### 4.2.5 Continuous Signal Model

In a real sonar system, the returns obtained from the ocean floor are continuous, rather than the product of discrete scatterers. We can model this by assuming that each hydrophone element  $k$  obtains a total signal  $s_k$  from some region of interest  $H$  at time  $t$  such that

$$s_k = \int_H A(h, k) (\cos \Psi(h, k) + i \sin \Psi(h, k)) dh$$

where

$$A(h, k) = I10^{-\alpha t_s c 10^{-4}}$$

is the amplitude of the signal received from the seafloor at  $h$  by hydrophone  $k$ ,

$$\Psi(h, k) = (t - t_s(h, k)) 2\pi f$$

is the phase of that signal, and

$$t_s(h, k) = \frac{\sqrt{de^2(h) + h^2}}{c} + \frac{\sqrt{de^2(h) + (kd - h)^2}}{c}$$

is the round trip time between the projection source, the seafloor at  $h$  and hydrophone  $k$ . The region of interest  $H$  is defined as all regions of the seafloor  $h$  such that  $t \geq t_s(h, k)$  and  $t \leq t_s(h, k) + t_p$ , where  $t_p$  is the duration of the ping.

If we approximate this integral with a discrete Riemann sum, we note that the discretisation obtained is (to a constant factor) equivalent to the ray tracing model of the simulator. We thus expect that as our seafloor discretisation parameter  $dh$  becomes smaller, so our simulator will better approximate the continuous model.

It is interesting to note that for a ping duration of sufficient length, the magnitude of the integral  $s_k$  may fall to approximately zero for a flat seafloor. We observe that for an appropriately chosen  $f$  (such that  $\alpha$  is small),  $A(h, k)$  is approximately constant across  $H$ , as the size of the region of interest is dependent on the ping duration  $t_p$ . Computing the change in  $A$  across  $H$ , we find that it is given by

$$\Delta A(h, k) = I10^{-\alpha t_s c 10^{-4}} \left( 1 - 10^{-\alpha t_p c 10^{-4}} \right).$$

As  $0.15\alpha t_p \ll 1$  (taking  $c$  as  $1500ms^{-1}$ ),  $\Delta A(h, k) \approx 0$ .

This implies that the signal  $s_k$  falls to approximately zero whenever  $\Psi(h, k)$  varies by  $2\pi$  across  $H$ , as  $A(h, k)$  may be considered approximately constant for small areas of  $H$  corresponding to a phase variation. To examine the size of such areas, let us suppose that the depth of the flat seafloor is  $2000m$ , the speed of sound  $c = 1500ms^{-1}$ , the frequency of the system  $10000kHz$  and  $k = 0$ . For a region of interest starting directly below the ship (at  $h = 0$ ), a

phase cycle will occur if the region of interest extends continuously to  $h = 17.32m$ . That is,  $\Psi(0, 0) - \Psi(17.32, 0) = 2\pi$ . Solving  $t_p \geq t_s(17.32, 0) - t_s(0, 0)$  (the ping duration), we are guaranteed a phase cycle if  $t_p \geq 9.9992 \times 10^{-5}s$ . We observe that this is approximately the period of the ping,  $1/f$ .

For oblique rays, taking the region of interest starting at  $h = 2000m$ , a phase cycle will occur if the region of interest extends continuously to  $h = 2000.11$ , a span of only  $11cm$ . The ping duration must similarly be  $t_p \geq 1.0371 \times 10^{-4}$  for this to happen.

Indeed, physically the ping duration should be an integer multiple of the period, as the projector will complete an integer number of pulsations per ping. Thus, we are always guaranteed a phase cycle in our measurement of the ocean floor. Setting the ping duration to less than the period is possible in the simulator, but corresponds to the unphysical case of the projector completing only a portion of its pulsation to produce a ping. It was also observed that the application of beamforming to such data resulted in a clear return at  $\theta = 0$ , with negligible returns elsewhere. This is due to an insufficient ping duration. Returns could only occupy a small portion of the phase range, and so phase differences between hydrophone elements became negligible, leading to a return at  $\theta = 0$ , the point at which we expect identical phasing across the array.

#### 4.2.6 Noise

Noise is added to the matrix of complex signals additively. *Random*, incoherent noise is computed by generating a matrix of Gaussian noise of power  $\sigma^2$ . This noise is independent of direction, and thus independent of  $k$ . *Persistent*, structured noise is added by computing the complex signal arriving at each hydrophone element at each time instant if the only incoming signal is from some direction  $\theta$  for all time instants. Both the structured and incoherent noise matrices are added to the signal matrix to produce the final output of the simulator.

### 4.3 Simulator Scope

#### 4.3.1 Parameters

The simulator has a number of parameters which may be altered to investigate different environments, but will remain hard-coded for this project. The seafloor area of interest was set in a  $\frac{2\pi}{3}$  arc, with discretisation to  $1cm$  for shallow water data and  $50cm$  for deep water data. The speed of sound was taken as  $1500ms^{-1}$ . The distance between hydrophone elements was set to half the wavelength to avoid aliasing. The intensity of each ray was arbitrarily chosen as 1000 divided by the number of seafloor elements, as the added noise is measured relative to the signal power. No claims are made that the measured ‘power’ corresponds to physical units.

The number of hydrophones, depth profile, frequency and sampling frequency were left as user inputs. The attenuation coefficient was chosen based on the user-defined frequency, and so care must be used when using high frequency signals, as they may not propagate to the required depths.

The SNR of the Gaussian noise, together with the direction(s) of arrival and SNR of the structured noise are user inputs in an optional program. All SNRs are measured relative to the mean amplitude of the pure signal matrix. For this research, the mean amplitude of the structured noise was taken as equal to the mean amplitude of the pure signal matrix. This is discussed further in Section 4.6.

### 4.3.2 Limitations

It is important to discuss what the simulator cannot model. The simulator models a single ping cycle under the assumption of perfect projection. Thus, we do not model noise from sidelobes, or reflections from a main lobe of measurable width. The swath is two dimensional.

The ray tracing model does not take into account multiple paths caused by refraction of signals due to changes in the speed of sound or reflections between seafloor elements. The speed of sound is assumed constant throughout the water column. The model doesn't account for signal interactions except at the hydrophone itself.

The hydrophone array is assumed uniform, linear and correctly calibrated and level. The simulator cannot model platform motion or error. While the simulator does allow arbitrary seafloor profiles, it is under the assumption that every seafloor element has an uninterrupted line of sight to every hydrophone in the array. Thus, we do not model acoustic shadowing. All seafloor elements are considered perfect reflectors. Scattering due to micro-relief is not modeled.

## 4.4 Design Issues and Testing

### 4.4.1 Implementation and Usage

The simulator was implemented in Matlab, using vectorised code to speed computation. The code, along with a demo file discussing its use, is available at <http://www.cs.wits.ac.za/~mitchley/research/>.

### 4.4.2 Testing

The correctness of the simulator was tested by beamforming over limited Sections of the seafloor. Signage and transformational errors were identified and corrected, and various issues such as the problematic case of a flat seafloor and insufficient ping duration were found.

The data output of the simulator has not, however, been compared to real deep sea data.



## 4.5 Ideal Ping Simulator

To facilitate testing of research hypotheses, a second simulator was created. This simulator (referred to as the ideal ping simulator, or IPS, in this document) creates an ideal clean ping of a flat ocean floor at arbitrary depths, sampling frequencies and signal frequencies.

### 4.5.1 Model

For each time instant  $t$  such that  $\frac{(ct)^2}{4} \geq de^2$ , the locations of current seafloor scatters were computed as

$$h = \pm \sqrt{\frac{(ct)^2}{4} - de^2}. \quad (4.3)$$

These scatterer locations were used to construct an ideal signal across the array using the signal model

$$x(t) = (a(\theta) + a(-\theta))s(t)$$

where

$$a(\theta) = \left[ 1, e^{ikd \sin \theta}, \dots, e^{-i(L-1)kd \sin \theta} \right]$$

and

$$\theta = \arctan \left( \frac{h}{de} \right).$$

The ping signal  $s(t)$  was computed as  $s(t) = A(h, 0)$ .

### 4.5.2 Limitations and Usage

The ideal ping simulator simulates a ping that is in perfect agreement with the signal model of Section 2.5.1. Such a situation cannot arise in reality, as we are expecting the ping to both propagate across the entire array (that is, be of a duration sufficient for a signal to propagate across the length of the array), and originate from a single point on the ocean floor (that is, be of infinitesimal duration so that  $H$  is a single point).

However, one knows precisely how many signals are in these simulated pings, and so we may test the accuracy of signal enumeration using this simulator. As before, the ideal simulator was implemented in Matlab, using vectorised code to speed computation. The code, along with a demo file discussing its use, is available at <http://www.cs.wits.ac.za/~mitchley/research/>.

## 4.6 Description of Data Sets

Before presenting the results, the data sets used will be presented. Each data set is a simulated input to a linear hydrophone array of 81 elements, each spaced  $d = \frac{\lambda}{2}m$  apart, and offset from the assumed projector source by  $kd$  meters for  $k = 0, 1, \dots, 80$ . The seafloor in each set was simulated between receive angles of  $-\frac{\pi}{3}$  and  $\frac{\pi}{3}$ .

For those data sets containing structured noise, it was added at the level of the average signal amplitude, with direction of arrival  $\theta = \frac{\pi}{4}$ . It should be noted that any reported SNR is measured between the pure signal and the additive Gaussian noise, and does not take into account the structured noise as either a noise or a signal component.

The properties of each data set are summarised in Table 4.2, and described in more detail in Sections 4.6.1 and 4.6.2.

	Depth	Frequency	Sampling	Ping Duration	Structured Noise	Envelope Size
Set 1	100m	300158Hz	14293Hz	IPS	No	10m
Set 2	100m	300158Hz	14293Hz	IPS	Yes	10m
Set 3	2000m	10000Hz	1000Hz	IPS	No	100m
Set 4	2000m	10000Hz	1000Hz	IPS	Yes	100m
Set 5	100m $\pm$ 10m	300158Hz	14293Hz	150 $\mu$ s	No	20m
Set 6	100m $\pm$ 10m	300158Hz	14293Hz	150 $\mu$ s	Yes	20m
Set 7	2000m $\pm$ 50m	10000Hz	1000Hz	5ms	No	100m
Set 8	2000m $\pm$ 50m	10000Hz	1000Hz	5ms	Yes	100m

Table 4.2: Summary of data set properties

### 4.6.1 Flat Seafloor Data Sets

Data sets 1-4 were created using the ideal ping simulator (IPS). These data sets simulate pings from flat seafloors under perfect conditions. Data set 1 is a shallow water set, simulated at 100m. Data set 2 is the same with added structured noise, at the same level as the average signal amplitude. Both sets simulate a system operating at 300158Hz, sampled at 14293Hz. Since the IPS simulates an ideal ping of infinitesimal length (yet reaching the entire array at different phases), there is no ping duration. The spectral outputs of a Bartlett beamformer applied to data sets 1 and 2 is shown in Figures 4.4 and 4.5, respectively. The resulting bottom profile for both is a perfectly flat sea floor at 100m depth. Data sets 1 and 2 were given a 10m envelope, and cover approximately 346m of seafloor.

Data set 3 is a deep water set, simulated at 2000m. Data set 4 is the same with added structured noise, at the same level as the average signal amplitude. Both sets simulate a system operating at 10000Hz, sampled at 1000Hz. The spectral outputs of a Bartlett beamformer applied to data sets 3 and 4 are shown in Figures 4.6 and 4.7, respectively. Again, the resulting bottom profile for both is a perfectly flat sea floor at 2000m depth. Data sets 3 and 4 were given a 100m envelope, and

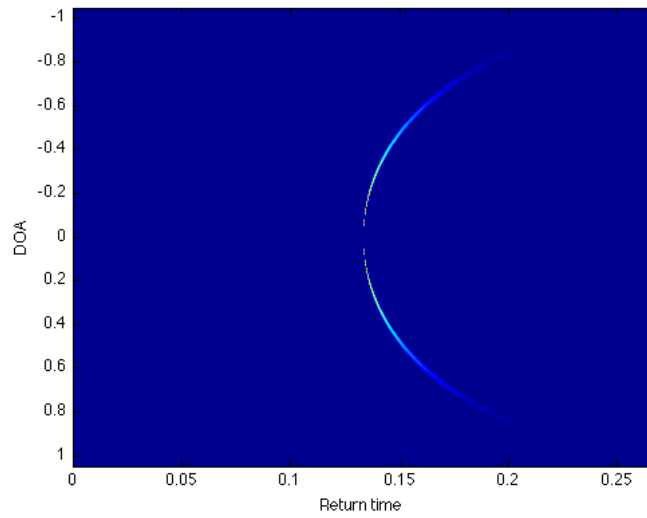


Figure 4.4: The spectral output for data set 1

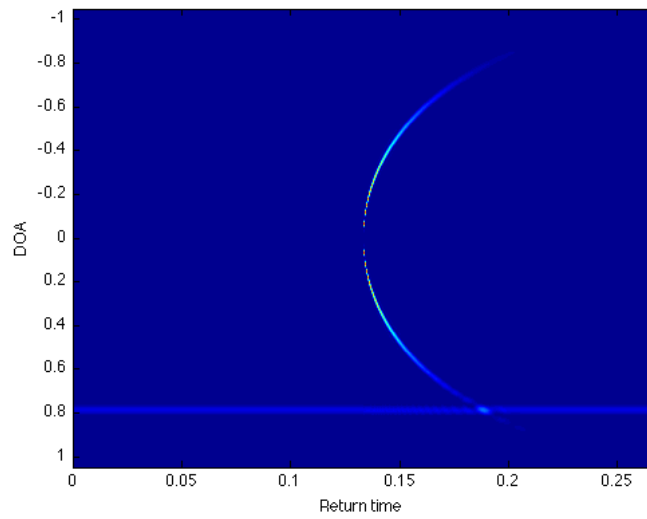


Figure 4.5: The spectral output for data set 2

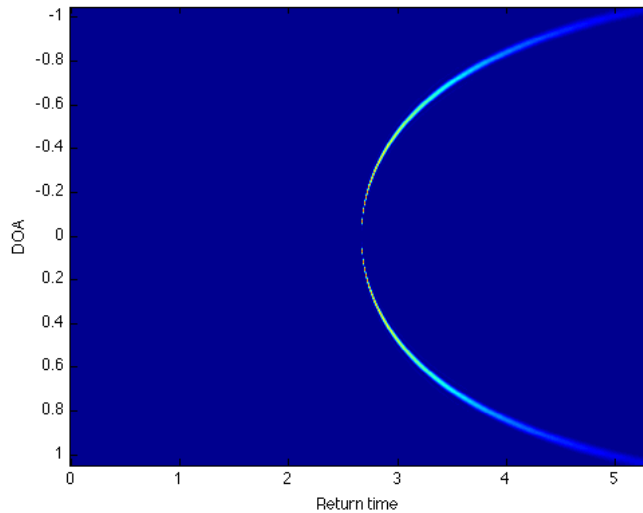


Figure 4.6: The spectral output for data set 3

cover approximately  $6928m$  of seafloor.

#### 4.6.2 Rough Seafloor Data Sets

Data sets 5-8 were created with the normal simulator. These data sets simulate pings of finite duration from seafloors exhibiting both macro-scale and micro-scale relief variation. Data set 5 is a shallow water set, simulated at  $100m$  with  $1cm$  random variation between seafloor elements and  $10m$  smooth variation over  $50m$  intervals. The seafloor elements are spaced  $1cm$  apart. Data set 6 is the same with added structured noise, at the same level as the average signal amplitude. Both sets simulate a system operating at  $300158Hz$ , sampled at  $14293Hz$ , with a ping duration of  $150$  microseconds. The spectral outputs of a Bartlett beamformer applied to data sets 5 and 6 are shown in Figures 4.8 and 4.9, respectively. The resulting bottom profile for both is shown in Figure 4.10. Data sets 5 and 6 were given a  $20m$  envelope, and cover approximately  $346m$  of seafloor.

Data set 7 is a deep water set, simulated at  $2000m$  with  $1cm$  random variation between seafloor elements and  $50m$  smooth variation over  $500m$  intervals. The seafloor elements are spaced  $50cm$  apart. Data set 8 is the same with added structured noise, at the same level as the average signal amplitude. Both sets simulate a system operating at  $10000Hz$ , sampled at  $1000Hz$ , with a ping duration of  $5$  milliseconds. The spectral outputs of a Bartlett beamformer applied to data sets 7 and 8 are shown in Figures 4.11 and 4.12, respectively. The resulting bottom profile for both is shown in Figure 4.13. Data sets 7 and 8 were given a  $100m$  envelope, and cover approximately  $6928m$  of seafloor.

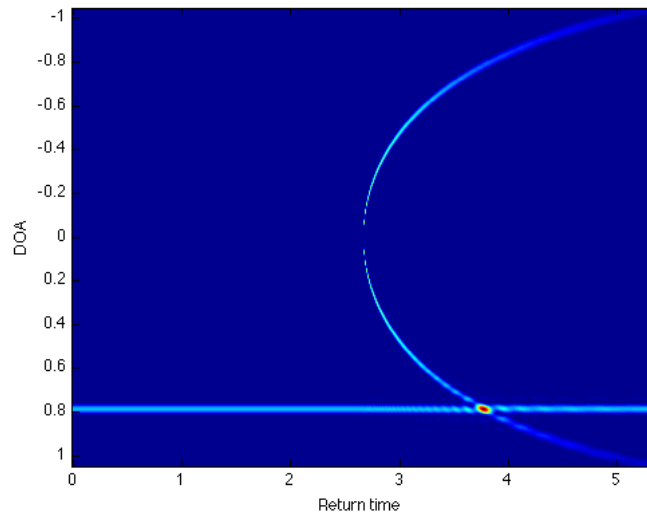


Figure 4.7: The spectral output for data set 4

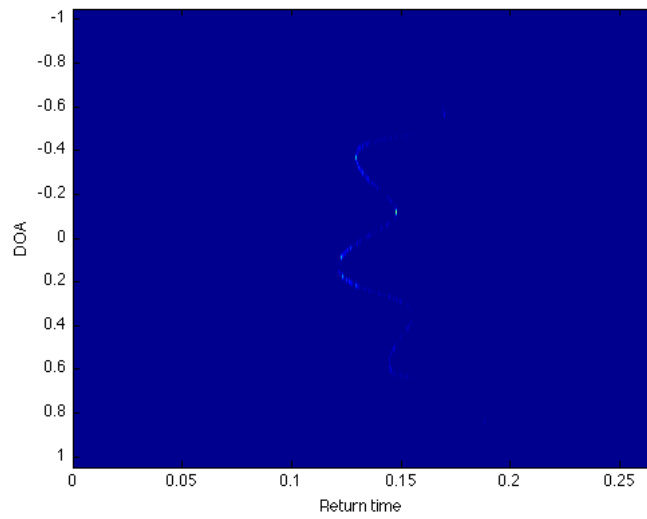


Figure 4.8: The spectral output for data set 5

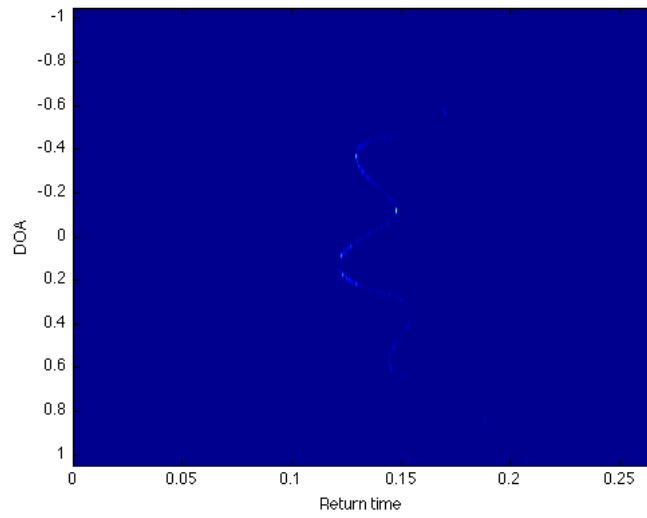


Figure 4.9: The spectral output for data set 6

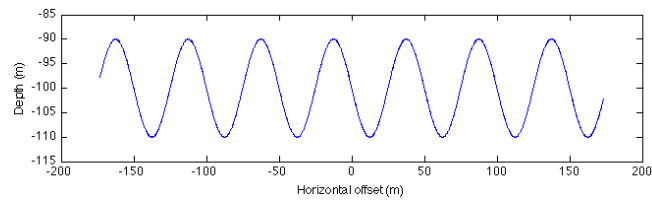


Figure 4.10: Depth profile for data sets 5 and 6

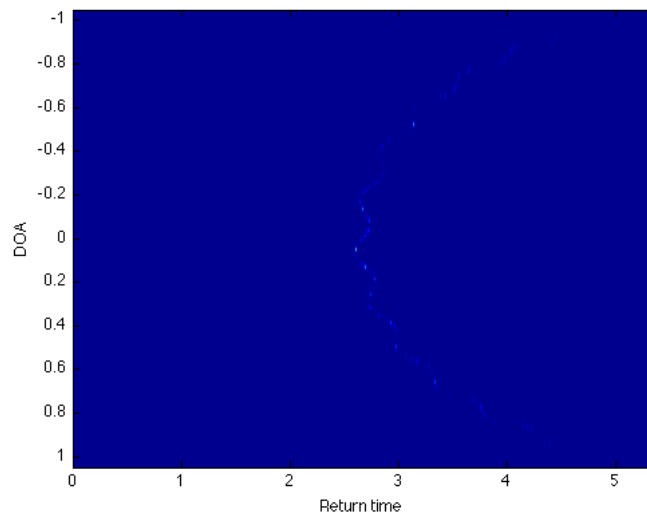


Figure 4.11: The spectral output for data set 7

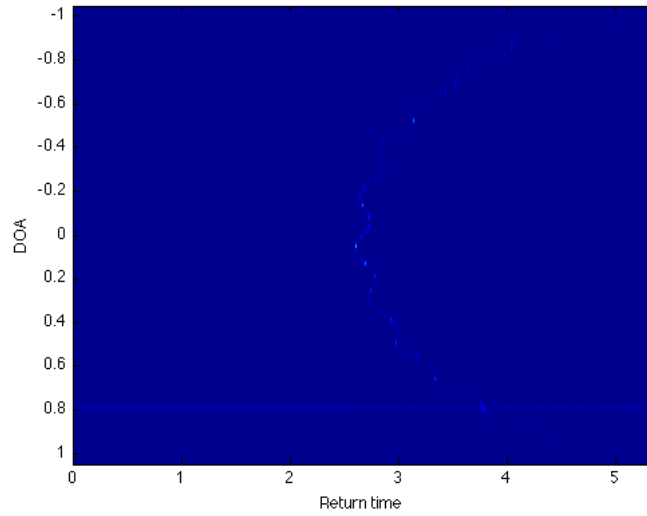


Figure 4.12: The spectral output for data set 8

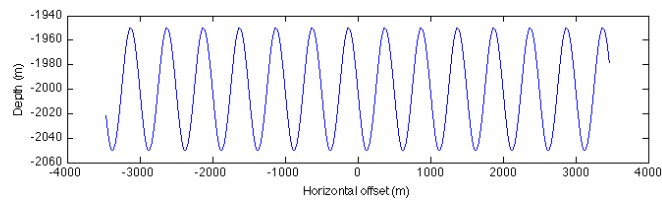


Figure 4.13: Depth profile for data sets 7 and 8

# Chapter 5

## Results

### 5.1 Introduction

In this Chapter, the results of the methodology discussed in Chapter 3 are presented. The first four data sets discussed in Section 4.6 are used to obtain signal enumeration results, presented in Section 5.2. These results are used to reduce the parameter space by selecting three parameter combinations to explore further. The depth profile results and sounding density results are discussed in Sections 5.3 and 5.4 respectively. These results are used to select three beamforming methods to compare in Section 5.5. Finally, we relate the results of this Chapter to the research hypotheses in Section 5.6.

### 5.2 Signal Enumeration Experiment

In this Section, we will examine the effect of combinations of the R-estimation, noise cancellation and signal enumeration schemes upon signal enumeration of ideal simulator data (data sets 1-4), since we know the ideal signal enumeration results for these data sets. As an examination of the full parameter space is infeasible within the context of this document, we will use the results of this Section to inform our search on subsequent data sets.

#### 5.2.1 Results

Table 5.1 shows the mean signal enumeration errors of each method combination applied to data set 1 with added Gaussian noise at the indicated SNR. Minimum values for each SNR are shown in bold. We see that the FB-smoothed KN method without noise correction produces the lowest errors for low SNR values, while F-smoothed MDL is best at SNRs of 5 and 10, and best on average. FB-smoothed AIC provides the best results only for an SNR of 20.

We should note that, as data set 1 contains no structured noise, the errors for no noise correction and structured noise correction should be identical - observed differences are due to random variation in the Gaussian noise. Recall from Section 3.4 that each result is averaged across 5 runs to minimise the effects of random variation.



Method Combination	SNR					
	-5	0	5	10	20	Mean
F-smoothing, AIC, None	1.1900	0.9191	0.6414	0.3654	0.0084	0.6249
F-smoothing, AIC, Structured	1.1942	0.9133	0.6425	0.3655	0.0055	0.6242
F-smoothing, AIC, Full	1.0982	0.9619	0.8133	0.6786	0.5263	0.8156
F-smoothing, MDL, None	1.1441	0.8715	0.5991	<b>0.3267</b>	0.0239	0.5931
F-smoothing, MDL, Structured	1.1440	0.8688	<b>0.5934</b>	0.3279	0.0248	<b>0.5918</b>
F-smoothing, MDL, Full	1.1065	0.9586	0.8333	0.6897	0.5229	0.8222
F-smoothing, KN, None	0.9642	0.8277	0.7007	0.5743	0.5160	0.7166
F-smoothing, KN, Structured	0.9701	0.8305	0.7725	0.5870	0.5703	0.7461
F-smoothing, Ronhovde, None	1.4483	1.1894	0.9415	0.6859	0.3544	0.9239
F-smoothing, Ronhovde, Structured	1.4418	1.1892	0.9359	0.6768	0.3558	0.9199
F-smoothing, Ronhovde, Full	1.3435	1.1153	0.8848	0.6505	0.3416	0.8672
FB-smoothing, AIC, None	1.2066	0.9273	0.6482	0.3746	0.0055	0.6324
FB-smoothing, AIC, Structured	1.2053	0.9227	0.6471	0.3811	<b>0.0041</b>	0.6321
FB-smoothing, AIC, Full	1.1684	1.0227	0.8955	0.7599	0.6370	0.8967
FB-smoothing, MDL, None	1.1520	0.8800	0.6062	0.3324	0.0192	0.5980
FB-smoothing, MDL, Structured	1.1544	0.8787	0.6072	0.3356	0.0184	0.5989
FB-smoothing, MDL, Full	1.1664	1.0358	0.8979	0.7732	0.6245	0.8996
FB-smoothing, KN, None	<b>0.9634</b>	<b>0.7950</b>	0.6143	0.4634	0.3585	0.6389
FB-smoothing, KN, Structured	0.9670	0.8083	0.6290	0.4815	0.4347	0.6641
FB-smoothing, Ronhovde, None	1.4214	1.1852	0.9260	0.6792	0.3510	0.9125
FB-smoothing, Ronhovde, Structured	1.4159	1.1690	0.9234	0.6686	0.3534	0.9061
FB-smoothing, Ronhovde, Full	1.3360	1.1035	0.8632	0.6422	0.3371	0.8564

Table 5.1: Signal enumeration results for data set 1

Table 5.2 shows the mean signal enumeration errors of each method combination applied to data set 2 with added Gaussian noise at the indicated SNR. Minimum values for each SNR are shown in bold. Unlike the previous data set, data set 2 contains structured noise. We observe that without noise correction, AIC and MDL errors tend to 1 as the SNR increases. This is because as the Gaussian noise vanishes, both MDL and AIC enumerate the signals more accurately, and the structured noise is a persistent extra signal. The fact that the error is below 1 for low SNR indicates that the MDL and AIC methods underestimated the number of signals, on average, for this data set.

It is interesting to note that the error of the FB-smoothed KN method without noise correction increases above 1.3 as the SNR increases, despite giving the best results at the lowest SNR. For higher SNRs, both F- and FB-smoothed KN methods benefit from structured noise correction. FB-smoothed MDL with structured noise correction is seen to provide the best results for an SNR of 5, as well as the best mean result. Interestingly, the results for full noise correction are dramatically worse for AIC and MDL as the SNR increases (going up to 4.7557 for F-smoothed MDL). This may indicate that the full noise correction procedure damages the expected eigenvalue distribution for these methods.

We see also that the Ronhovde method works best at high SNR, with full noise correction. This is perhaps unsurprising, as it is this noise correction procedure that is used in Ronhovde [1999].

Method Combination	SNR					
	-5	0	5	10	20	Mean
F-smoothing, AIC, None	1.0350	0.8859	0.8900	0.9031	0.9757	0.9379
F-smoothing, AIC, Structured	1.1501	0.9435	0.7997	0.7280	0.7580	0.8759
F-smoothing, AIC, Full	1.1037	0.9763	0.8353	0.7014	2.7607	1.2755
F-smoothing, MDL, None	0.9792	<b>0.8751</b>	0.8979	0.9159	0.9947	0.9325
F-smoothing, MDL, Structured	1.0986	0.9191	0.8033	0.7259	0.7958	0.8686
F-smoothing, MDL, Full	1.1214	0.9868	0.8535	0.7111	4.7557	1.6857
F-smoothing, KN, None	0.9988	1.0657	1.1757	1.3097	1.4357	1.1971
F-smoothing, KN, Structured	1.0514	1.0141	1.0018	0.8590	0.5507	0.8954
F-smoothing, Ronhovde, None	1.4041	1.1691	0.9433	0.8143	0.8508	1.0363
F-smoothing, Ronhovde, Structured	1.2909	1.0280	0.8785	0.7950	0.6628	0.9310
F-smoothing, Ronhovde, Full	1.3395	1.0634	0.8457	<b>0.6878</b>	0.4954	0.8864
FB-smoothing, AIC, None	1.0470	0.8944	0.9039	0.9211	0.9860	0.9505
FB-smoothing, AIC, Structured	1.1677	0.9607	0.7945	0.7275	0.6906	0.8682
FB-smoothing, AIC, Full	1.1615	1.0549	0.9422	0.8105	1.8983	1.1735
FB-smoothing, MDL, None	0.9924	0.8848	0.9058	0.9281	1.0015	0.9425
FB-smoothing, MDL, Structured	1.1269	0.9353	<b>0.7914</b>	0.7207	0.7145	<b>0.8578</b>
FB-smoothing, MDL, Full	1.1610	1.0510	0.9337	0.8066	3.5334	1.4971
FB-smoothing, KN, None	<b>0.9453</b>	0.9929	1.0857	1.1862	1.3023	1.1025
FB-smoothing, KN, Structured	0.9830	0.9237	0.9214	0.8729	0.6645	0.8731
FB-smoothing, Ronhovde, None	1.3860	1.1478	0.9504	0.8320	0.8697	1.0372
FB-smoothing, Ronhovde, Structured	1.2876	1.0273	0.8851	0.7814	0.6317	0.9226
FB-smoothing, Ronhovde, Full	1.3238	1.0821	0.8669	0.6902	<b>0.4803</b>	0.8887

Table 5.2: Signal enumeration results for data set 2

Table 5.3 shows the mean signal enumeration errors of each method combination applied to data set 3 with added Gaussian noise at the indicated SNR. Minimum values for each SNR are shown in bold. Surprisingly, for high SNRs, the AIC methods perform far better than any others, with an average signal enumeration error roughly equal to 0.005. As was the case with data set 1, the KN methods perform best at low SNR (specifically,  $-5$ ), while F-smoothed MDL with structured noise correction performs best at an SNR of 0, and on average. Similarly, due to data set 3 having no structured noise present, differences between the correction for structured noise and no noise correction may be attributed to random variation.

As before, the Ronhovde method performs at its best when used with full noise correction, although in contrast with data set 2 it never outperforms any other method. The MDL and AIC methods do not benefit from the full noise correction scheme.

Method Combination	SNR					
	-5	0	5	10	20	Mean
F-smoothing, AIC, None	1.1417	0.2747	0.0076	0.0055	0.0056	0.2870
F-smoothing, AIC, Structured	1.1384	0.2744	0.0064	0.0057	0.0059	0.2862
F-smoothing, AIC, Full	0.9899	0.6864	0.5055	0.5183	0.5352	0.6471
F-smoothing, MDL, None	0.9802	0.2014	0.0255	0.0265	0.0241	0.2515
F-smoothing, MDL, Structured	0.9691	<b>0.1921</b>	0.0250	0.0253	0.0267	<b>0.2476</b>
F-smoothing, MDL, Full	1.0036	0.6675	0.5210	0.5074	0.5353	0.6470
F-smoothing, KN, None	0.6900	0.4963	0.4937	0.5028	0.5089	0.5383
F-smoothing, KN, Structured	0.7167	0.5471	0.5180	0.5468	0.5282	0.5714
F-smoothing, Ronhovde, None	1.2366	0.4976	0.1974	0.1832	0.1826	0.4595
F-smoothing, Ronhovde, Structured	1.2266	0.4993	0.1967	0.1824	0.1842	0.4578
F-smoothing, Ronhovde, Full	1.1626	0.4689	0.1917	0.1757	0.1784	0.4355
FB-smoothing, AIC, None	1.1669	0.2998	<b>0.0053</b>	0.0051	0.0047	0.2964
FB-smoothing, AIC, Structured	1.1754	0.3002	0.0054	<b>0.0046</b>	<b>0.0043</b>	0.2980
FB-smoothing, AIC, Full	1.0733	0.7679	0.6211	0.6362	0.6348	0.7467
FB-smoothing, MDL, None	1.0137	0.2070	0.0194	0.0196	0.0191	0.2557
FB-smoothing, MDL, Structured	1.0100	0.2110	0.0207	0.0190	0.0174	0.2556
FB-smoothing, MDL, Full	1.0713	0.7796	0.6276	0.6404	0.6241	0.7486
FB-smoothing, KN, None	<b>0.6631</b>	0.3771	0.3527	0.3504	0.3629	0.4212
FB-smoothing, KN, Structured	0.6775	0.4164	0.3836	0.3787	0.3622	0.4437
FB-smoothing, Ronhovde, None	1.2195	0.4958	0.1939	0.1821	0.1824	0.4547
FB-smoothing, Ronhovde, Structured	1.2104	0.4933	0.1960	0.1819	0.1810	0.4525
FB-smoothing, Ronhovde, Full	1.1330	0.4649	0.1884	0.1737	0.1757	0.4271

Table 5.3: Signal enumeration results for data set 3

Table 5.4 shows the mean signal enumeration errors of each method combination applied to data set 4 with added Gaussian noise at the indicated SNR. Minimum values for each SNR are shown in bold. As is the case with data sets 1-3, we observe that the FB-smoothed KN method with structured noise correction performs best at an SNR of  $-5$ . FB-smoothed MDL and AIC perform best with structured noise correction at SNRs of 0 and 5 respectively.

We observe too that, as was the case with data set 2, the structured noise present in this data set causes the errors of the MDL and AIC methods to tend to 1 without structured noise correction, and to jump as high as 6.2756 with full noise correction. In addition, the FB-smoothed Ronhovde method performs best for high SNRs with full noise correction, and for this data set performs best overall.

In contrast with the previous three data sets, none of the methods using F-smoothing performed best, for any SNR.

Method Combination	SNR					
	-5	0	5	10	20	Mean
F-smoothing, AIC, None	0.9884	0.8212	0.9441	0.9579	0.9767	0.9377
F-smoothing, AIC, Structured	1.0798	0.4086	0.3787	0.4416	0.6772	0.5972
F-smoothing, AIC, Full	1.0267	0.7071	0.4863	0.3611	3.4124	1.1987
F-smoothing, MDL, None	0.8613	0.8605	0.9704	0.9831	1.0029	0.9356
F-smoothing, MDL, Structured	0.9280	0.4135	0.4450	0.4542	0.7152	0.5912
F-smoothing, MDL, Full	1.0157	0.7078	0.4947	0.3581	6.2756	1.7704
F-smoothing, KN, None	0.9974	1.3433	1.4007	1.4129	1.4364	1.3181
F-smoothing, KN, Structured	0.8996	0.8735	0.7562	0.5666	0.3417	0.6875
F-smoothing, Ronhovde, None	1.2596	1.0243	1.0061	0.9559	0.9298	1.0351
F-smoothing, Ronhovde, Structured	1.2610	0.8442	0.5881	0.3816	0.2001	0.6550
F-smoothing, Ronhovde, Full	1.1827	0.6257	0.3745	0.2836	0.1561	0.5245
FB-smoothing, AIC, None	1.0316	0.8286	0.9594	0.9731	0.9880	0.9561
FB-smoothing, AIC, Structured	1.1289	0.4066	<b>0.3184</b>	0.4287	0.5964	0.5758
FB-smoothing, AIC, Full	1.1165	0.8129	0.6316	0.5015	2.1301	1.0385
FB-smoothing, MDL, None	0.8935	0.8592	0.9803	0.9916	1.0038	0.9457
FB-smoothing, MDL, Structured	0.9851	<b>0.3839</b>	0.3682	0.4637	0.6193	0.5641
FB-smoothing, MDL, Full	1.1065	0.8136	0.6455	0.5000	4.2744	1.4680
FB-smoothing, KN, None	0.8975	1.2183	1.2730	1.2931	1.2992	1.1962
FB-smoothing, KN, Structured	<b>0.7692</b>	0.6884	0.6813	0.6295	0.4811	0.6499
FB-smoothing, Ronhovde, None	1.2419	1.0373	1.0169	0.9700	0.9457	1.0424
FB-smoothing, Ronhovde, Structured	1.2413	0.7889	0.5318	0.3373	0.1929	0.6184
FB-smoothing, Ronhovde, Full	1.1774	0.6160	0.3604	<b>0.2733</b>	<b>0.1559</b>	<b>0.5166</b>

Table 5.4: Signal enumeration results for data set 4

### 5.2.2 Discussion

It is interesting to note that of the 24 best methods (6 SNR values across 4 data sets), only 7 utilise the F-smoothing covariance estimation method. The results are not such that we can come to the conclusion that forward-backward smoothing is superior to forward smoothing, but we will rule out further investigation of the F-smoothing technique for subsequent tests, due to its lack of clearly superior results.

We observe that, in the absence of structured noise, there is (or, rather, should be) no difference between the results of the no noise correction and structured noise correction techniques. Indeed, the only way their results could be different (beyond the variances attributable to random noise) would be for the signal enumeration method to incorrectly enumerate the signals within the estimate of  $R$  obtained from thousands of samples outside the envelope. If a signal enumeration method cannot correctly enumerate the signals within an estimate of  $R$  obtained from thousands of samples, it is unlikely to do better on an estimate of  $R$  obtained from one.

We see also that the full noise correction method was of benefit to the Ronhovde enumeration method only. Indeed, this method could not be used in conjunction with the KN method, and resulted in higher errors for both MDL and AIC. It would seem that the full noise correction method, that is, the method whereby the out-of-envelope estimate of  $R$  is subtracted from all subsequent covariance matrices, damages the expected eigenvalue spread on which MDL and AIC rely.

For these reasons, we will only consider structured noise correction in subsequent tests, when used in conjunction with MDL, AIC or KN.

While the method of Ronhovde gave the best performance for two data sets, we observe that that performance was only at high SNR values (10 and 20 for both data sets), and indeed superior average performance was only observed in data set 4. We thus rule out this method in subsequent tests. Under the assumption that a more accurate enumeration of signals will result in a better depth profile, we will consider the AIC, MDL and KN signal enumeration methods, combined with FB-smoothed covariance estimation and structured noise correction only.

## 5.3 Depth Profile Experiment

In this Section, we examine the mean depth errors reported for a variety of beamformers, using the AIC, MDL and KN signal enumeration methods, combined with FB-smoothed covariance estimation and structured noise correction.

The Bartlett and Capon mean amplitude and maximum amplitude methods do not rely on the signal enumeration methods. Thus, any variation in the results for these four methods may be attributed to the random noise. As was the case with the results in the previous Section, these results have been averaged across 5 runs to minimise the effect of this random variation.

The spectral beamformers (Bartlett, Capon and MUSIC) were run on a uniform grid of 210 angles between  $-\frac{\pi}{3}$  and  $\frac{\pi}{3}$ .

The depth errors shown in this Section are the mean depth errors for accepted soundings, averaged across SNRs of  $-5$ ,  $0$ ,  $5$ ,  $10$  and  $20$ . The full results for each SNR value can be found in appendix A. A sounding is accepted if it is within the envelope of that data set, and is discarded if it is outside that envelope. The mean depth errors are computed as the mean absolute difference between the reported depth at a point, and the true depth. All results are rounded to the nearest *cm*.

### 5.3.1 Results

In Table 5.5, we observe that the best results are obtained for a combination of any parametric high resolution beamforming method and AIC for data set 1, and the Capon mean amplitude method for data set 2. It is worth noting again that the only difference between data sets 1 and 2 is the presence of a persistent signal emanating from a source with DOA  $\frac{\pi}{4}$ . The parametric high resolution beamformers give an average error  $15\text{cm}$  greater than that of the Capon beamformer in data set 2, at a depth of  $100\text{m}$ . Indeed, it should be noted that with the exception of the Bartlett and Capon peak-finding methods, all the methods in Table 5.5 produce errors less than 1% of the water depth.

We note that there is no difference between the results obtained by the root-MUSIC methods, and those obtained by either SSF or WSF. This is of interest, as the SSF and WSF methods used DOA estimates of root-MUSIC as initial values in their optimisation procedures. It would then appear that those starting values are in fact very close (and possibly identical to) the minimising values of SSF and WSF for these two data sets.

Table 5.6 shows the mean depth errors for data sets 3 and 4. Both these data sets are deep sea sets, with the only difference being the presence of structured noise in data set 4. We note that all the methods for both data sets produce errors less than 1% of the water depth of  $2000\text{m}$ . In the results of data set 3 we see that the AIC results are uniformly better than those of MDL and KN, but the parametric high resolution beamformers are outperformed by the conventional spectral beamformers, especially the Capon mean amplitude method.

	Methods	AIC	MDL	KN
Data set 1	Bartlett Peaks	0.26m	0.31m	0.78m
	Bartlett Mean Amp	0.43m	0.43m	0.43m
	Bartlett Max Amp	0.67m	0.69m	0.68m
	Capon Peaks	0.27m	0.30m	0.65m
	Capon Mean Amp	0.19m	0.19m	0.20m
	Capon Max Amp	0.32m	0.32m	0.40m
	MUSIC Peaks	0.26m	0.30m	0.64m
	MUSIC Mean Amp	0.86m	0.71m	0.34m
	MUSIC Max Amp	0.45m	0.39m	0.36m
	Root-MUSIC	<b>0.14m</b>	0.18m	0.49m
	SSF	<b>0.14m</b>	0.18m	0.49m
	WSF	<b>0.14m</b>	0.18m	0.49m
ESPRIT	<b>0.14m</b>	0.18m	0.51m	
Data set 2	Bartlett Peaks	0.66m	0.73m	1.03m
	Bartlett Mean Amp	0.45m	0.45m	0.45m
	Bartlett Max Amp	0.74m	0.72m	0.76m
	Capon Peaks	1.16m	1.22m	1.45m
	Capon Mean Amp	<b>0.27m</b>	<b>0.27m</b>	0.29m
	Capon Max Amp	0.71m	0.72m	0.78m
	MUSIC Peaks	0.52m	0.58m	0.83m
	MUSIC Mean Amp	0.55m	0.48m	0.32m
	MUSIC Max Amp	0.47m	0.39m	0.37m
	Root-MUSIC	0.42m	0.48m	0.72m
	SSF	0.42m	0.48m	0.72m
	WSF	0.42m	0.49m	0.72m
ESPRIT	0.47m	0.53m	0.78m	

Table 5.5: Mean depth errors for FB-smoothed R-estimation and structured noise correction applied to data sets 1 & 2

The results of data set 4 are similar, with AIC outperforming MDL and KN, but with the best results achieved by the Capon mean amplitude method. As with data sets 1 and 2, we see that for both data sets, SSF and WSF produce results that appear identical (or slightly worse) than those of their seeding method, root-MUSIC. It is also interesting to note that the results of ESPRIT are similar to those of root-MUSIC, with variations perhaps largely attributable to random noise for the MDL and AIC signal enumeration methods.

	Methods	AIC	MDL	KN
Data set 3	Bartlett Peaks	6.21m	6.57m	8.79m
	Bartlett Mean Amp	2.52m	2.54m	2.52m
	Bartlett Max Amp	7.88m	7.94m	7.90m
	Capon Peaks	6.28m	6.61m	8.24m
	Capon Mean Amp	<b>1.19m</b>	1.20m	1.41m
	Capon Max Amp	2.79m	2.85m	3.98m
	MUSIC Peaks	6.20m	6.55m	8.09m
	MUSIC Mean Amp	3.29m	3.07m	1.91m
	MUSIC Max Amp	2.58m	2.64m	2.76m
	Root-MUSIC	3.44m	3.79m	5.24m
	SSF	3.44m	3.79m	5.25m
	WSF	3.44m	3.79m	5.26m
ESPRIT	3.36m	3.76m	5.46m	
Data set 4	Bartlett Peaks	8.54m	9.03m	10.24m
	Bartlett Mean Amp	3.29m	3.28m	3.30m
	Bartlett Max Amp	8.97m	9.06m	9.13m
	Capon Peaks	9.33m	9.72m	10.93m
	Capon Mean Amp	2.18m	2.20m	2.40m
	Capon Max Amp	7.12m	7.03m	7.78m
	MUSIC Peaks	7.30m	7.71m	8.77m
	MUSIC Mean Amp	2.75m	2.56m	<b>1.94m</b>
	MUSIC Max Amp	3.09m	3.02m	3.40m
	Root-MUSIC	5.02m	5.49m	6.45m
	SSF	5.08m	5.54m	6.44m
	WSF	5.08m	5.55m	6.46m
ESPRIT	4.81m	5.33m	6.22m	

Table 5.6: Mean depth errors for FB-smoothed R-estimation and structured noise correction applied to data sets 3 & 4

Table 5.7 shows the mean depth errors for data sets 5 and 6. These data sets are shallow water sets with rough variation obtained from the normal simulator. We note that the mean errors reported in this Table are uniformly greater than those of Table 5.5, despite having the same mean depth. We propose that it is the violation of the signal model assumptions that causes the greater mean error, rather than the introduction of rough variation.

In contrast to the IPS data sets, we observe that the Capon maximum amplitude method produces the lowest error for data set 5, while the MUSIC maximum amplitude method produces the lowest errors for data set 6. For those methods that rely on signal enumeration, we observe that the KN method produces uniformly greater errors than AIC and MDL. AIC outperforms both MDL and KN, for both data sets.

As before, SSF and WSF appear to have not significantly improved the initial values supplied by root-MUSIC. Of the parametric high resolution beamformers, ESPRIT is seen to produce results



equivalent to or slightly better than the others.

	Methods	AIC	MDL	KN
Data set 5	Bartlett Peaks	2.34m	2.71m	4.03m
	Bartlett Mean Amp	3.56m	3.56m	3.56m
	Bartlett Max Amp	1.13m	1.22m	1.19m
	Capon Peaks	2.20m	2.52m	3.88m
	Capon Mean Amp	3.53m	3.52m	3.57m
	Capon Max Amp	<b>0.71m</b>	0.78m	1.10m
	MUSIC Peaks	2.14m	2.51m	3.87m
	MUSIC Mean Amp	3.16m	2.96m	2.52m
	MUSIC Max Amp	0.81m	0.79m	0.89m
	Root-MUSIC	1.06m	1.28m	2.34m
	SSF	1.05m	1.26m	2.32m
	WSF	1.05m	1.27m	2.33m
	ESPRIT	0.98m	1.18m	2.22m
Data set 6	Bartlett Peaks	3.28m	3.66m	4.72m
	Bartlett Mean Amp	3.59m	3.59m	3.59m
	Bartlett Max Amp	1.24m	1.18m	1.22m
	Capon Peaks	4.79m	5.11m	6.02m
	Capon Mean Amp	3.68m	3.68m	3.70m
	Capon Max Amp	1.97m	2.01m	2.20m
	MUSIC Peaks	2.96m	3.31m	4.36m
	MUSIC Mean Amp	2.82m	2.76m	2.74m
	MUSIC Max Amp	1.03m	<b>0.94m</b>	1.08m
	Root-MUSIC	2.15m	2.41m	3.31m
	SSF	2.14m	2.39m	3.29m
	WSF	2.14m	2.39m	3.30m
	ESPRIT	2.15m	2.39m	3.28m

Table 5.7: Mean depth errors for FB-smoothed R-estimation and structured noise correction applied to data sets 5 & 6

Table 5.8 shows the mean depth errors for data sets 7 and 8. These data sets are deep water sets with rough variation obtained from the normal simulator. These results are, in absolute terms, the worst obtained in this research. However, at a mean water depth of  $2000m$ , these errors are in fact in the neighbourhood of 1% of the water depth.

As was the case with data sets 5 and 6, the Capon and MUSIC beamformers produce the best results with maximum amplitude TOA detection for data sets 7 and 8 respectively. SSF and WSF exhibit a slight improvement over root-MUSIC for both data sets, although this improvement is less than  $5cm$ . We also note that ESPRIT outperforms the other parametric high resolution beamformers, and AIC outperforms MDL and KN.

	Methods	AIC	MDL	KN
Data set 7	Bartlett Peaks	19.66m	20.86m	24.84m
	Bartlett Mean Amp	14.00m	14.00m	13.97m
	Bartlett Max Amp	11.33m	11.33m	11.31m
	Capon Peaks	18.08m	19.18m	22.63m
	Capon Mean Amp	11.86m	11.87m	12.00m
	Capon Max Amp	<b>5.41m</b>	5.48m	6.21m
	MUSIC Peaks	19.59m	20.95m	25.37m
	MUSIC Mean Amp	7.70m	7.74m	8.14m
	MUSIC Max Amp	6.61m	6.71m	6.58m
	Root-MUSIC	17.33m	18.73m	23.19m
	SSF	17.28m	18.70m	23.15m
	WSF	17.30m	18.72m	23.24m
ESPRIT	16.94m	18.34m	22.93m	
Data set 8	Bartlett Peaks	20.42m	21.55m	24.55m
	Bartlett Mean Amp	13.87m	13.88m	13.86m
	Bartlett Max Amp	11.53m	11.47m	11.47m
	Capon Peaks	20.57m	21.47m	24.34m
	Capon Mean Amp	13.01m	12.90m	13.02m
	Capon Max Amp	9.91m	9.55m	10.40m
	MUSIC Peaks	19.57m	20.68m	23.61m
	MUSIC Mean Amp	8.57m	8.62m	8.79m
	MUSIC Max Amp	7.15m	<b>7.13m</b>	7.37m
	Root-MUSIC	17.69m	18.92m	21.92m
	SSF	17.63m	18.89m	21.89m
	WSF	17.66m	18.93m	21.95m
ESPRIT	17.44m	18.65m	21.80m	

Table 5.8: Mean depth errors for FB-smoothed R-estimation and structured noise correction applied to data sets 7 & 8

### 5.3.2 Discussion

In all the data sets examined in this Section, we see the following trends emerging. The Capon mean amplitude beamformer results in depth estimates with the lowest mean errors in all the IPS data sets, while the Capon maximum amplitude beamformer produces the best results for data sets 5 and 7. The MUSIC maximum amplitude beamformer produced the best results for data sets 6 and 8.

The peak detection methods generally result in the highest depth estimate errors. This suggests that the Bartlett and Capon beamforming methods do not benefit from signal enumeration, at least under the suggested peak-finding scheme. Interestingly, neither does the MUSIC beamforming method, beyond the division of the signal and noise subspaces.

The SSF and WSF methods failed to improve on the initial estimates provided by root-MUSIC to any statistically significant degree. As these methods are highly computationally expensive due

to the multidimensional global optimisation involved in both, it seems that, in this application, they do not add value.

ESPRIT produces results comparable to those of root-MUSIC via a subspace fitting approach that does not involve expensive optimisation procedures. In data sets 3, 4, 5, 7 and 8, ESPRIT's estimates were more accurate than those of root-MUSIC, albeit to a small degree.

When exposed to data sets 5-8 (those data sets created with the normal simulator), we see larger errors than those of data sets 1-4. There are central differences between these two groups of data sets that may account for this. Firstly, data sets 1-4 simulate a perfectly flat seafloor, while data sets 5-8 simulate seafloors with micro-scale and macro-scale variation. It may be that beamforming methods simply work best for flat surfaces. This may indeed be the case for those methods relying on time of arrival estimation (namely, the conventional beamformers employing mean and maximum amplitude detection), but since the parametric high-resolution beamformers process each time sample independently, there is no reason to suspect they would perform better for flat surfaces.

The second major difference between the two groups of data sets is in how they are made. Data sets 1-4 are created by the ideal ping simulator, which perfectly corresponds to the assumed signal model, wherein discrete sources (or, in active sonar, ensonified scatterers) broadcast signals that are picked up simultaneously (but in different phases) by every element of the hydrophone array. With a finite ping duration, this is an impossibility, as each hydrophone will be receiving returns from a slightly different continuous Section of seafloor at any moment in time. This is the situation modelled by the normal simulator to produce data sets 5-8.

It may be that it is this violation of the assumed signal model that produces the higher errors seen in Tables 5.7 and 5.8.

## 5.4 Profile Density Experiment

In this Section, we examine the number of accepted (in-envelope) soundings reported for a variety of beamformers, using the AIC, MDL and KN signal enumeration methods, combined with FB-smoothed covariance estimation and structured noise correction. In all Tables in this Section, the number of soundings is averaged across SNRs of  $-5$ ,  $0$ ,  $5$ ,  $10$  and  $20$ . The full results for each SNR value can be found in appendix B.

As the spectral beamformers (Bartlett, Capon and MUSIC) were run on a uniform grid of 210 angles, the mean and maximum amplitude methods report exactly 210 soundings. These results are thus excluded from this Section. In the deep sea data sets (3, 4, 7 and 8), we require at least 6928 equally spaced soundings to obtain a resolution of  $1m$ .

### 5.4.1 Results

In Table 5.9, we see the average number of accepted soundings for data sets 1 and 2. We see that the Bartlett peak-finding method combined with KN signal enumeration produced the highest number of accepted soundings. Moreover, the KN method uniformly produced more soundings than AIC and MDL, for any beamforming method. It is interesting to compare this Table with Table 5.5, wherein we see that the Bartlett peak-finding method combined with KN produced the largest mean depth errors for data set 1, and the KN method uniformly produced larger mean depth errors generally.

We note that, as was the case with the mean depth errors, the SSF and WSF methods have not improved the number of accepted soundings over root-MUSIC. We note too that the number of accepted soundings uniformly decreases in the presence of structured noise.

Table 5.10 shows the number of accepted soundings for deep sea IPS data sets 3 and 4. Again, Bartlett peak-finding under KN produces the largest number of accepted soundings, coupled with the highest depth error for data set 3. We also see that KN uniformly results in more accepted soundings, with larger mean depth errors (as shown in Table 5.6). Again, SSF and WSF do not exhibit any marked improvement over root-MUSIC.

Table 5.11 shows the number of accepted soundings for data sets 5 and 6, the shallow water data sets produced by the normal simulator. Here, we see the largest number of accepted soundings resulting from ESPRIT beamforming and KN signal enumeration for both data sets. As before, KN signal enumeration results in uniformly higher numbers of soundings, at the cost of higher mean depth errors (Table 5.7).

We see that the number of accepted signals is uniformly lower for data set 6 than for data set 5. Again, SSF and WSF have not improved on the results of root-MUSIC. It is interesting to note how many more soundings are obtained for data sets 5 and 6 when compared to the other shallow water sets, 1 and 2.

	Methods	AIC	MDL	KN
Data set 1	Bartlett Peaks	2497	2594	3119
	Capon Peaks	2493	2585	2911
	MUSIC Peaks	2496	2587	2995
	Root-MUSIC	2495	2585	2967
	SSF	2495	2585	2967
	WSF	2495	2585	2967
	ESPRIT	2495	2585	2966
Data set 2	Bartlett Peaks	2554	2635	2901
	Capon Peaks	2013	2079	2267
	MUSIC Peaks	2436	2499	2717
	Root-MUSIC	2458	2524	2712
	SSF	2459	2523	2711
	WSF	2458	2524	2711
	ESPRIT	2450	2517	2704

Table 5.9: Number of soundings for FB-smoothed R-estimation and structured noise correction applied to data sets 1 & 2

	Methods	AIC	MDL	KN
Data set 3	Bartlett Peaks	4514	4669	5167
	Capon Peaks	4511	4662	5002
	MUSIC Peaks	4514	4665	5091
	Root-MUSIC	4514	4665	5077
	SSF	4514	4665	5077
	WSF	4514	4665	5078
	ESPRIT	4514	4665	5070
Data set 4	Bartlett Peaks	4592	4730	5063
	Capon Peaks	3312	3422	3629
	MUSIC Peaks	4489	4627	4930
	Root-MUSIC	4523	4659	4938
	SSF	4525	4662	4942
	WSF	4525	4662	4941
	ESPRIT	4523	4659	4930

Table 5.10: Number of soundings for FB-smoothed R-estimation and structured noise correction applied to data sets 3 & 4

	Methods	AIC	MDL	KN
Data set 5	Bartlett Peaks	3838	4184	5253
	Capon Peaks	3675	3967	4832
	MUSIC Peaks	3855	4209	5284
	Root-MUSIC	3916	4290	5389
	SSF	3916	4290	5390
	WSF	3916	4290	5389
	ESPRIT	3918	4294	5397
Data set 6	Bartlett Peaks	3736	4051	4626
	Capon Peaks	3312	3578	4088
	MUSIC Peaks	3656	3937	4486
	Root-MUSIC	3744	4047	4603
	SSF	3745	4049	4603
	WSF	3745	4049	4604
	ESPRIT	3764	4074	4629

Table 5.11: Number of soundings for FB-smoothed R-estimation and structured noise correction applied to data sets 5 & 6

Finally, in Table 5.12 we see the number of accepted soundings for deep water data sets 7 and 8. We see again that the largest number of soundings obtained is for the ESPRIT beamforming method using KN signal enumeration, and the KN enumeration method generally produces more accepted soundings. We note that, as with previous data sets, the presence of structured noise results in fewer accepted soundings.

SSF and WSF both exhibit improvements in the number of soundings over root-MUSIC in these two data sets, which is of interest due to their slight improvements in the mean depth error, too. It should be noted however that the largest improvement in the number of soundings is 23 soundings (between KN root-MUSIC and SSF for data set 8), an improvement of less than 0.5%.

#### 5.4.2 Discussion

Examining all data sets, we see that there appears to be a trade-off between the number of accepted soundings, and the mean depth error. The results suggest that the AIC signal enumeration method, while producing fewer accepted soundings than either MDL or KN, give the lowest mean depth errors for the parametric methods when used in conjunction with root-MUSIC or ESPRIT. KN would then appear to produce more soundings at the cost of some accuracy.

We will conclude that the AIC signal enumeration method gives better results than either MDL or KN, when applied to parametric high resolution beamformers. We will also conclude that SSF and WSF provide neither a significant increase in accuracy nor more accepted soundings over root-MUSIC, within the context of this research. ESPRIT produces results highly similar to root-MUSIC, although more accurate for most data sets. We therefore pick the combination of ESPRIT beamforming and AIC signal enumeration, along with the previous choices of FB-smoothed covari-

	Methods	AIC	MDL	KN
Data set 7	Bartlett Peaks	3881	4090	4720
	Capon Peaks	3907	4099	4665
	MUSIC Peaks	4088	4340	5038
	Root-MUSIC	4655	4999	5944
	SSF	4661	5010	5965
	WSF	4661	5009	5961
	ESPRIT	4701	5061	6033
Data set 8	Bartlett Peaks	3631	3807	4193
	Capon Peaks	2883	3043	3406
	MUSIC Peaks	3745	3914	4318
	Root-MUSIC	4138	4363	4822
	SSF	4153	4380	4845
	WSF	4154	4383	4840
	ESPRIT	4173	4404	4884

Table 5.12: Number of soundings for FB-smoothed R-estimation and structured noise correction applied to data sets 7 & 8

ance estimation and structured noise correction as the best example of parametric high resolution beamforming.

While the peak-finding methods provide the largest number of accepted sounds for data sets 1-4, they also produce mean depth errors uniformly larger than those of any other method. This peak-finding approach is, in some senses, a hybrid of conventional beamforming and high resolution approaches, combining signal enumeration via eigenanalysis with standard power spectrum estimation. It is interesting to note that the conventional beamforming methods do not benefit from signal enumeration, at least within this implementation.

We note that, while the Capon and MUSIC maximum amplitude beamforming methods resulted in the smallest mean depth errors, these were obtained for a grid of 210 DOAs. We must thus investigate the performance of both these beamforming methods on a grid comparable in size to the number of soundings obtained by the high resolution methods. The Capon beamforming method, while not a high resolution method, provides better results than the Bartlett method by suppressing energy contribution outside the look direction. MUSIC is a high resolution method, but is pseudospectral in nature. We select both the Capon maximum amplitude method and the MUSIC maximum amplitude method for further investigation.

## 5.5 Further Investigation

For further investigation of the three selected method combinations, we will use data sets 7 and 8 exclusively. These data sets most closely resemble the circumstances described in the problem definition. These methods will be compared to the Bartlett mean amplitude beamforming method.

The Bartlett mean amplitude, Capon maximum amplitude and MUSIC maximum amplitude methods were rerun on grids matching the number of valid soundings obtained for ESPRIT beamforming with AIC signal enumeration for each SNR value. As covariance estimation using spatial smoothing reduces the effective aperture of the array, and the resolution of the Bartlett beamforming method is explicitly dependent on the array length, we will also examine a Bartlett beamformer operating at full aperture by using

$$\mathbf{R} = \bar{\mathbf{x}}\bar{\mathbf{x}}^H$$

as its covariance estimate, without noise correction.

The resulting mean depth errors are reported in Table 5.13, and plotted in Figures 5.1 and 5.2. Under the assumption that the soundings obtained are equally spaced, we require at least 6928 soundings to obtain a resolution of  $1m$ .

We see that the presence of structured noise results in a slight increase in the mean depth error for all the methods except the noise corrected Bartlett beamformer, and a marked decrease in the number of soundings for SNRs above 5.

Curiously, we see that the MUSIC and ESPRIT methods exhibit an increase in mean depth error as the SNR increases. This may be attributable to an increase in the number of spurious soundings (that is, an overestimate of the number of signals). This is in contrast to the results of Section 5.2, which suggested that the AIC signal enumeration method would perform best at high SNR values.

Despite this behaviour, the MUSIC maximum amplitude beamformer uniformly outperforms the parametric ESPRIT beamformer, while matching its average resolution. The best performance at each SNR value is obtained by Capon maximum amplitude beamforming for data set 7, and MUSIC maximum amplitude beamforming for data set 8, although we should note that MUSIC does not suffer significant performance degradation in the presence of structured noise.

The Bartlett beamformers outperform ESPRIT at SNR values greater than or equal to 5, but both Capon and MUSIC beamforming outperform both Bartlett beamformers at all tested SNR values. We observe that the Bartlett beamformer operating at full aperture outperforms the Bartlett beamformer with spatial smoothing, even in the presence of structured noise. We observe that at SNRs of 10 and below, none of the methods have enough soundings to resolve a  $1m$  target.

Based on these results, we test the full aperture Bartlett beamformer, Capon beamformer and MUSIC beamformer further. We set a fixed grid of 7000 points for all SNR values. Both the Capon and MUSIC beamformers used forward backward-smoothed covariance estimation and structured noise correction. The AIC signal enumeration method was used with MUSIC. The full aperture



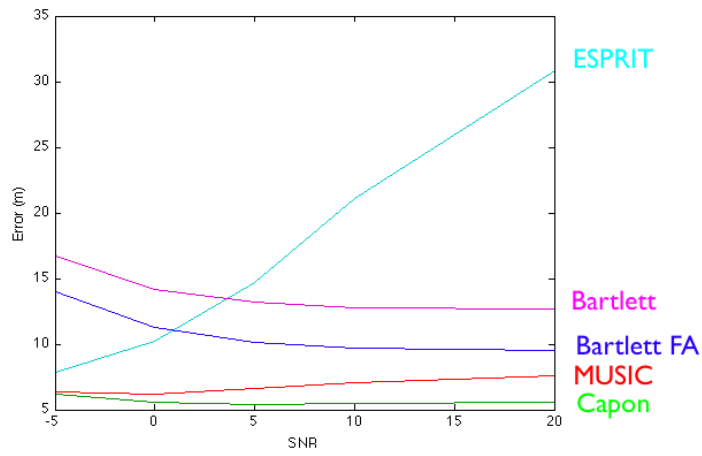


Figure 5.1: Mean depth errors for selected beamforming methods on data set 7

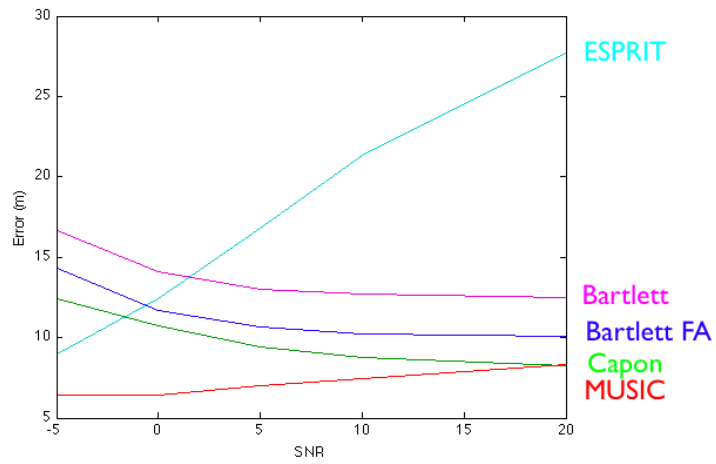


Figure 5.2: Mean depth errors for selected beamforming methods on data set 8

	Methods	SNR				
		-5	0	5	10	20
Data set 7	Bartlett F.A.	14.02m	11.27m	10.11m	9.72m	9.56m
	Bartlett Mean Amp	16.74m	14.20m	13.16m	12.79m	12.66m
	Capon Max Amp	<b>6.15m</b>	<b>5.57m</b>	<b>5.41m</b>	<b>5.49m</b>	<b>5.60m</b>
	MUSIC Max Amp	6.37m	6.19m	6.65m	7.02m	7.55m
	ESPRIT	7.84m	10.22m	14.69m	21.11m	30.84m
	Number of soundings	1537	2695	4041	5915	9316
Data set 8	Bartlett F.A.	14.36m	11.70m	10.65m	10.26m	10.11m
	Bartlett Mean Amp	16.68m	14.10m	13.03m	12.68m	12.52m
	Capon Max Amp	12.43m	10.75m	9.44m	8.79m	<b>8.24m</b>
	MUSIC Max Amp	<b>6.40m</b>	<b>6.44m</b>	<b>7.04m</b>	<b>7.43m</b>	8.33m
	ESPRIT	8.98m	12.43m	16.78m	21.31m	27.71m
	Number of soundings	1600	2728	3946	5325	7266

Table 5.13: Mean depth errors for five selected methods performed on data sets 7 and 8

Bartlett beamformer did not make use of spatial smoothing or noise correction. These results are shown in Table 5.14, and plotted in Figures 5.3 and 5.4.

	Methods	SNR				
		-5	0	5	10	20
Data set 7	Bartlett F.A.	14.05m	11.21m	10.11m	9.73m	9.56m
	Capon Max Amp	6.32m	<b>5.47m</b>	<b>5.44m</b>	<b>5.51m</b>	<b>5.62m</b>
	MUSIC Max Amp	<b>6.23m</b>	6.23m	6.65m	6.96m	7.40m
Data set 8	Bartlett F.A.	14.40m	11.61m	10.64m	10.27m	10.10m
	Capon Max Amp	12.75m	10.88m	9.73m	8.85m	<b>8.16m</b>
	MUSIC Max Amp	<b>6.59m</b>	<b>6.31m</b>	<b>6.89m</b>	<b>7.62m</b>	8.49m

Table 5.14: Mean depth error results on a fixed grid of 7000 points

These results do not differ very much from those seen in Table 5.13, although each error is reported for a fixed grid of 7000 points, for an average resolution of less than  $1m$ . We note however that the MUSIC method exhibits a small growth in inaccuracy at high SNR values despite the fixed grid.

It is of interest to note the resolution of the modelled system if an FFT was used to perform Bartlett beamforming. In this case, we would seek solutions to equation 2.4 (reproduced below)

$$\theta_m = \sin^{-1} \left( \frac{\lambda m}{dL} \right)$$

for  $L = 81$  and  $d = \frac{\lambda}{2}$ , giving

$$\theta_m = \sin^{-1} \left( \frac{2m}{81} \right)$$

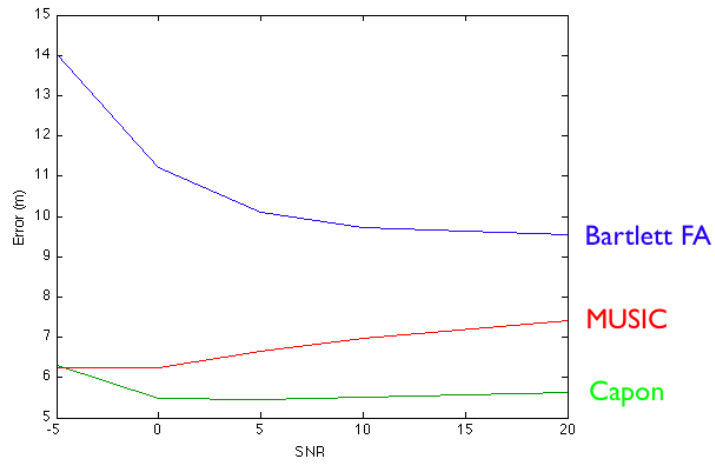


Figure 5.3: Mean depth errors for selected beamforming methods on data set 7 using a fixed grid

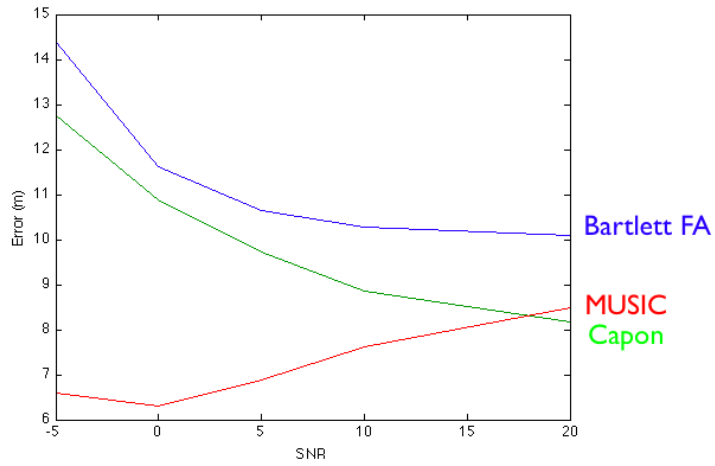


Figure 5.4: Mean depth errors for selected beamforming methods on data set 8 using a fixed grid

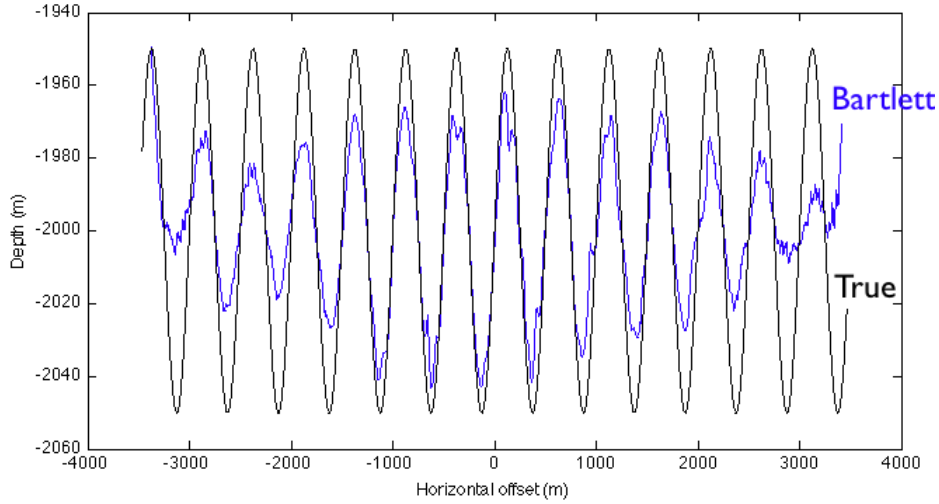


Figure 5.5: Bottom profile obtained by the Bartlett beamformer on data set 8 using a fixed grid

which is satisfied by 81 values of  $m$ , from  $-40$  to  $40$ , far below the capabilities of a high resolution system.

In Figure 5.5 we see a bottom profile obtained by the Bartlett beamformer on data set 8 using a fixed grid of 7000 points at an SNR of  $-5$ , compared to the true bottom profile for data set 8. From a qualitative perspective, we see that both the Capon and MUSIC bottom profiles (shown in Figures 5.6 and 5.7 respectively) produce results closer to the true profile. Interestingly, we observe substantial errors in the Capon profile around the location of the structured noise source. The MUSIC profile is clearer than both, perhaps indicating that this method is more robust to structured and incoherent noise.

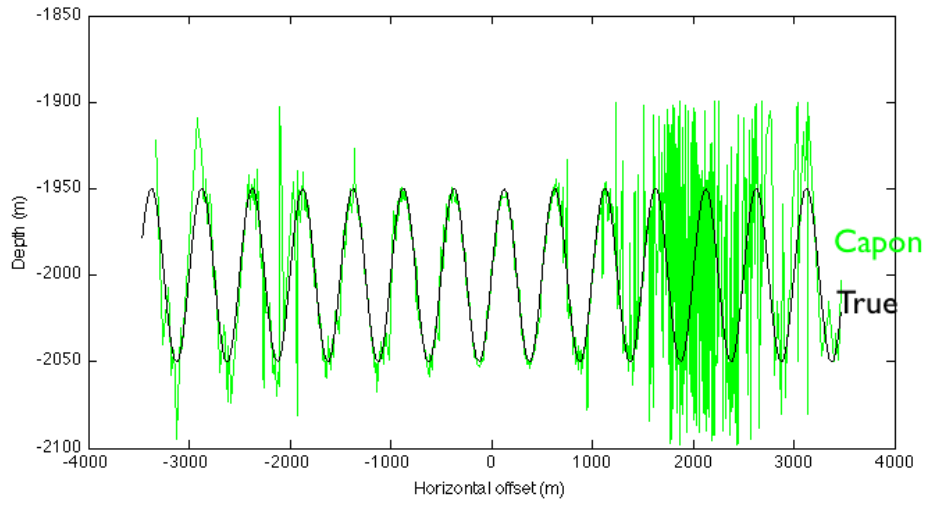


Figure 5.6: Bottom profile obtained by the Capon beamformer on data set 8 using a fixed grid

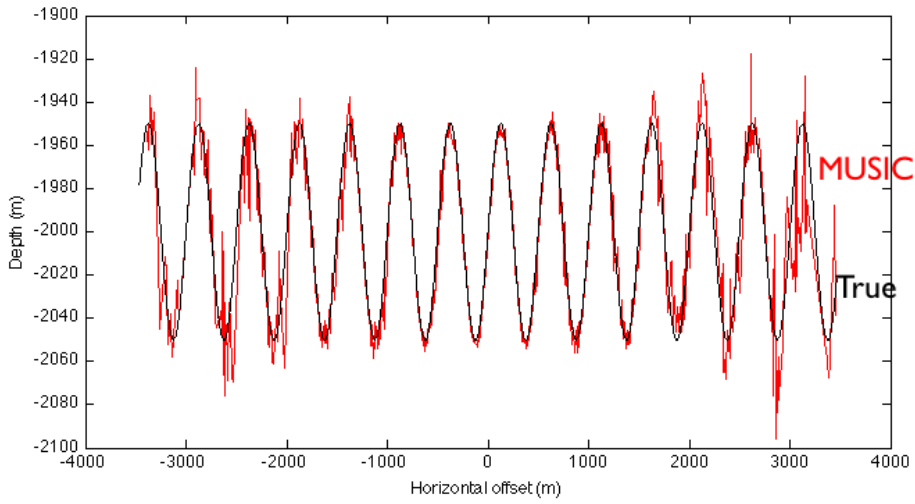


Figure 5.7: Bottom profile obtained by the MUSIC beamformer on data set 8 using a fixed grid

## 5.6 Discussion

We now discuss the results shown in this Chapter with specific reference to the hypotheses of Section 3.3, reproduced below for the reader's convenience.

1. A model of the noise field can be estimated using out-of-envelope measurements. We can then correct incoming signals for both structured and incoherent noise to obtain more accurate soundings.
2. An appropriate signal subspace cutoff threshold can be chosen through information theoretic methods.
3. A bathymetric profile with a better resolution and higher accuracy than that of the Bartlett beamformer can be obtained through correction for noise and high resolution techniques.

With respect to hypothesis one, it has been demonstrated that signal enumeration with the AIC, MDL and KN methods is more accurate when correcting for structured noise, but only the method of Ronhovde improved when correcting for both structured and incoherent noise. We thus claim that hypothesis one is partly verified, that is, we can correct incoming signals for structured noise to obtain more accurate soundings. It would appear that the method used to correct for both structured and incoherent noise results in highly inaccurate signal enumeration, although it is possible that a better noise correction method exists.

We have also shown that MDL, AIC and KN signal enumeration all perform better than the method of Ronhovde at low and medium SNR values in the presence of structured noise, and at all SNR values in data without structured noise. In particular, we note the excellent performance of AIC on data sets 1 and 3 at high SNR. We therefore verify hypothesis two. That is, an appropriate signal subspace cutoff threshold can be chosen through information theoretic methods. We note however that the use of full noise correction severely degraded the performance of these methods.

The results of Section 5.5 indicate that hypothesis three can be verified, in the form of the MUSIC maximum amplitude method. This method is a pseudospectral high resolution method which can be run on an arbitrary grid. With noise correction, this method is robust to the presence of structured noise. This method was seen to produce more accurate bathymetric profiles on grids matching those of parametric high resolution methods in density, as well as a grid of 7000 points. We note that the grid sizes tested in Section 5.5 are far denser than would be obtained using FFT-based Bartlett beamforming. We note however that parametric high resolution beamforming methods such as ESPRIT did not result in more accurate bathymetric profiles generally.

We thus claim that, with respect to the problem definition given in Section 3.2, a sonar beamforming method exists that will facilitate the detection of SMS chimneys of  $1m$  diameter at a depth of  $2km$ .

## 5.7 Relation to Other Work

Pantartzis *et al.* [1993] discuss the application of Capon and high resolution techniques to multi-beam sonar data. In their work, it was found that MUSIC outperformed the conventional Fourier transform-based beamformer, producing data with a higher resolution and slightly improved accuracy. It was also found that parametric high resolution methods produced results comparable to those of MUSIC. These tests were performed on a simulated flat seafloor with  $100m$  between the seafloor and the array. Gaussian noise was added at an SNR greater than  $10dB$ .

Our results extend the results seen in Pantartzis *et al.* [1993] in that more beamforming techniques are applied to more data sets under more SNR values. The results of Pantartzis *et al.* [1993] agree with the results obtained in this research.

Ronhovde [1999] applied several high resolution beamforming techniques to real sonar data obtained from a shallow water Simrad system. Only full noise correction was investigated in this thesis, and the best parameter combinations were given for each beamforming method. It was found that generally forward-backward smoothed covariance estimation produced the best results, and some methods (notably, MUSIC and root-MUSIC) performed better with full noise correction. Ronhovde [1999] in addition also investigated the optimal number of subarrays for each method.

In our research, the smallest number of subarrays required to bring the covariance matrix to full rank was used. It was also found that full noise correction only improved signal enumeration when used with the method of Ronhovde. It was found that FB-smoothing produced slightly more accurate signal enumeration, agreeing with Ronhovde [1999].

Comparing the various methods, Ronhovde [1999] found that quantitatively, Capon, MUSIC, root-MUSIC and ESPRIT all provided similar performance (under the performance measures used in that research). Under qualitative testing, it was found that Capon beamforming and root-MUSIC produced results slightly noisier than those of MUSIC, while ESPRIT gave similar performance to MUSIC. These results are slightly different to the ones shown here, wherein we found that ESPRIT and root-MUSIC give similar results, and the results of Capon and MUSIC are better than both.

This difference may be a result of the maximum amplitude method performing well when the seafloor has uniform reflectivity, as it does in our simulated data sets.

## Chapter 6

# Conclusion

Multibeam echo sounders provide a relatively inexpensive means for obtaining bathymetric profiles that could potentially be used to find SMS chimney fields. Conventional beamforming methods, such as the Bartlett and Capon methods explored here are used by many sonar bathymetric systems to maximise hydrophone array sensitivity in a particular direction. Commonly, this is accomplished through hardware-based fast Fourier transforms for online data processing.

High resolution beamforming methods (such as MUSIC, SSF and ESPRIT covered in this document) provide a way around the inherent aperture-based resolution limitations of conventional beamformers but require estimation of additional parameters. It is possible to correct these methods for incoming noise in addition to estimating the direction of arrival of incoming signals at each time instant.

It was hypothesised that a method with greater accuracy and resolution than a conventional Bartlett beamformer could be found. To test this in a quantitative manner, two novel simulators were developed, and eight different data sets each modelling a single ping cycle were created with known ground truth. It was found that spatial smoothing using forward-backward covariance estimation, combined with persistent noise correction resulted in the most accurate signal enumeration. It was also found that the AIC signal enumeration method often produced the lowest mean depth estimation errors for each of the thirteen beamforming methods tested.

Both the Capon and MUSIC beamforming methods outperformed the conventional Bartlett beamforming method in terms of accuracy at matched resolutions. The MUSIC method in particular did not suffer major performance degradation in the presence of structured noise. As it produces more accurate bathymetric profiles at arbitrary resolution levels, and in particular at levels wherein SMS chimneys could be resolved, it is this MUSIC method that verifies the hypothesis.

This implies that a switch from FFT-based to MUSIC-based beamforming (and a corresponding switch from online to offline processing) may result in the detection of SMS chimney fields using a conventional multibeam sonar system at sea level.

This conjecture could be tested with raw data from the system from an area known to contain an SMS chimney field, although such data was not available for this research. A larger study into



different beamforming methods may yield a more suitable beamformer than MUSIC. It would also be necessary to investigate aspects of sonar bathymetry that were not covered in this project, such as correction for errors, sound velocity profile correction and visualisation of soundings.

# Appendix A

## Full Depth Profile Results

Methods	SNR				
	-5	0	5	10	20
Bartlett Peaks	0.20m	0.24m	0.27m	0.31m	0.30m
Bartlett Mean Amp	0.32m	0.39m	0.45m	0.48m	0.51m
Bartlett Max Amp	0.82m	0.69m	0.60m	0.59m	0.66m
Capon Peaks	0.21m	0.24m	0.27m	0.31m	0.31m
Capon Mean Amp	0.26m	0.23m	0.20m	0.15m	0.09m
Capon Max Amp	0.62m	0.44m	0.29m	0.16m	0.08m
MUSIC Peaks	0.20m	0.24m	0.27m	0.31m	0.30m
MUSIC Mean Amp	1.42m	1.22m	0.79m	0.52m	0.34m
MUSIC Max Amp	0.94m	0.78m	0.31m	0.15m	0.08m
Root-MUSIC	0.13m	0.15m	0.16m	0.17m	0.12m
SSF	0.13m	0.15m	0.16m	0.17m	0.12m
WSF	0.13m	0.15m	0.16m	0.17m	0.12m
ESPRIT	0.13m	0.14m	0.15m	0.17m	0.11m

Table A.1: Mean depth errors for F-smoothed R-estimation, AIC signal enumeration and coherent noise correction performed on data set 1

Methods	SNR				
	-5	0	5	10	20
Bartlett Peaks	0.25m	0.28m	0.32m	0.36m	0.32m
Bartlett Mean Amp	0.32m	0.39m	0.45m	0.49m	0.51m
Bartlett Max Amp	0.80m	0.69m	0.65m	0.63m	0.65m
Capon Peaks	0.26m	0.28m	0.31m	0.34m	0.31m
Capon Mean Amp	0.26m	0.24m	0.19m	0.15m	0.09m
Capon Max Amp	0.66m	0.39m	0.28m	0.19m	0.09m
MUSIC Peaks	0.26m	0.28m	0.31m	0.34m	0.31m
MUSIC Mean Amp	1.10m	0.92m	0.69m	0.49m	0.33m
MUSIC Max Amp	0.79m	0.59m	0.31m	0.19m	0.07m
Root-MUSIC	0.19m	0.18m	0.19m	0.20m	0.13m
SSF	0.19m	0.18m	0.19m	0.20m	0.13m
WSF	0.19m	0.18m	0.19m	0.20m	0.13m
ESPRIT	0.19m	0.19m	0.19m	0.20m	0.12m

Table A.2: Mean depth errors for F-smoothed R-estimation, MDL signal enumeration and coherent noise correction performed on data set 1

Methods	SNR				
	-5	0	5	10	20
Bartlett Peaks	0.76m	0.72m	0.88m	0.84m	0.72m
Bartlett Mean Amp	0.31m	0.39m	0.45m	0.49m	0.51m
Bartlett Max Amp	0.86m	0.70m	0.58m	0.62m	0.65m
Capon Peaks	0.77m	0.67m	0.74m	0.57m	0.50m
Capon Mean Amp	0.28m	0.23m	0.25m	0.16m	0.10m
Capon Max Amp	0.74m	0.47m	0.48m	0.19m	0.13m
MUSIC Peaks	0.80m	0.70m	0.66m	0.58m	0.48m
MUSIC Mean Amp	0.52m	0.40m	0.33m	0.26m	0.18m
MUSIC Max Amp	0.71m	0.50m	0.31m	0.19m	0.10m
Root-MUSIC	0.66m	0.55m	0.51m	0.43m	0.27m
SSF	0.66m	0.55m	0.51m	0.43m	0.27m
WSF	0.66m	0.55m	0.51m	0.43m	0.27m
ESPRIT	0.69m	0.59m	0.54m	0.45m	0.27m

Table A.3: Mean depth errors for F-smoothed R-estimation, KN signal enumeration and coherent noise correction performed on data set 1

Methods	SNR				
	-5	0	5	10	20
Bartlett Peaks	0.27m	0.48m	0.69m	0.85m	1.01m
Bartlett Mean Amp	0.32m	0.40m	0.48m	0.51m	0.54m
Bartlett Max Amp	0.88m	0.72m	0.67m	0.69m	0.72m
Capon Peaks	0.97m	1.19m	1.38m	1.23m	1.03m
Capon Mean Amp	0.39m	0.34m	0.28m	0.22m	0.11m
Capon Max Amp	1.22m	0.96m	0.73m	0.51m	0.14m
MUSIC Peaks	0.27m	0.45m	0.53m	0.61m	0.72m
MUSIC Mean Amp	1.04m	0.70m	0.49m	0.35m	0.17m
MUSIC Max Amp	0.98m	0.65m	0.44m	0.21m	0.09m
Root-MUSIC	0.20m	0.37m	0.44m	0.52m	0.59m
SSF	0.20m	0.37m	0.44m	0.52m	0.59m
WSF	0.20m	0.37m	0.44m	0.52m	0.59m
ESPRIT	0.20m	0.34m	0.47m	0.58m	0.76m

Table A.4: Mean depth errors for F-smoothed R-estimation, AIC signal enumeration and coherent noise correction performed on data set 2

Methods	SNR				
	-5	0	5	10	20
Bartlett Peaks	0.38m	0.56m	0.81m	0.87m	1.01m
Bartlett Mean Amp	0.33m	0.40m	0.47m	0.51m	0.54m
Bartlett Max Amp	0.84m	0.74m	0.65m	0.66m	0.71m
Capon Peaks	1.14m	1.32m	1.39m	1.23m	1.03m
Capon Mean Amp	0.37m	0.36m	0.29m	0.23m	0.10m
Capon Max Amp	1.14m	1.04m	0.72m	0.54m	0.13m
MUSIC Peaks	0.38m	0.53m	0.64m	0.62m	0.71m
MUSIC Mean Amp	0.89m	0.61m	0.45m	0.31m	0.15m
MUSIC Max Amp	0.77m	0.59m	0.31m	0.19m	0.09m
Root-MUSIC	0.30m	0.45m	0.56m	0.54m	0.57m
SSF	0.30m	0.45m	0.56m	0.53m	0.58m
WSF	0.30m	0.45m	0.56m	0.53m	0.58m
ESPRIT	0.29m	0.43m	0.59m	0.59m	0.73m

Table A.5: Mean depth errors for F-smoothed R-estimation, MDL signal enumeration and coherent noise correction performed on data set 2

Methods	SNR				
	-5	0	5	10	20
Bartlett Peaks	0.99m	1.06m	1.18m	1.12m	0.81m
Bartlett Mean Amp	0.32m	0.40m	0.47m	0.51m	0.54m
Bartlett Max Amp	0.95m	0.74m	0.70m	0.68m	0.71m
Capon Peaks	1.69m	1.67m	1.46m	1.34m	1.09m
Capon Mean Amp	0.39m	0.42m	0.31m	0.24m	0.10m
Capon Max Amp	1.22m	1.15m	0.80m	0.58m	0.14m
MUSIC Peaks	1.02m	0.95m	0.86m	0.76m	0.55m
MUSIC Mean Amp	0.42m	0.38m	0.33m	0.26m	0.19m
MUSIC Max Amp	0.70m	0.48m	0.31m	0.23m	0.14m
Root-MUSIC	0.89m	0.84m	0.77m	0.68m	0.43m
SSF	0.89m	0.84m	0.77m	0.67m	0.42m
WSF	0.89m	0.84m	0.77m	0.67m	0.41m
ESPRIT	0.91m	0.86m	0.81m	0.72m	0.60m

Table A.6: Mean depth errors for F-smoothed R-estimation, KN signal enumeration and coherent noise correction performed on data set 2

Methods	SNR				
	-5	0	5	10	20
Bartlett Peaks	5.68m	7.52m	6.65m	5.77m	5.44m
Bartlett Mean Amp	2.07m	2.37m	2.61m	2.74m	2.82m
Bartlett Max Amp	11.33m	8.79m	7.46m	6.42m	5.40m
Capon Peaks	5.75m	7.67m	6.77m	5.81m	5.43m
Capon Mean Amp	1.89m	1.42m	1.12m	0.85m	0.65m
Capon Max Amp	5.93m	3.65m	2.20m	1.37m	0.79m
MUSIC Peaks	5.68m	7.50m	6.65m	5.76m	5.42m
MUSIC Mean Amp	6.24m	3.48m	2.52m	2.15m	2.07m
MUSIC Max Amp	5.58m	3.19m	2.03m	1.33m	0.78m
Root-MUSIC	4.57m	5.71m	4.00m	2.20m	0.72m
SSF	4.57m	5.71m	4.00m	2.20m	0.72m
WSF	4.57m	5.71m	4.00m	2.20m	0.72m
ESPRIT	4.59m	5.71m	3.80m	2.06m	0.66m

Table A.7: Mean depth errors for F-smoothed R-estimation, AIC signal enumeration and coherent noise correction performed on data set 3

Methods	SNR				
	-5	0	5	10	20
Bartlett Peaks	6.81m	7.98m	6.72m	5.87m	5.50m
Bartlett Mean Amp	2.14m	2.36m	2.62m	2.75m	2.82m
Bartlett Max Amp	11.33m	8.84m	7.67m	6.48m	5.36m
Capon Peaks	6.87m	8.15m	6.78m	5.83m	5.43m
Capon Mean Amp	1.85m	1.45m	1.14m	0.86m	0.71m
Capon Max Amp	6.24m	3.46m	2.25m	1.48m	0.80m
MUSIC Peaks	6.84m	7.98m	6.68m	5.81m	5.43m
MUSIC Mean Amp	5.27m	3.32m	2.50m	2.22m	2.00m
MUSIC Max Amp	5.57m	3.38m	2.09m	1.39m	0.80m
Root-MUSIC	5.67m	6.29m	4.04m	2.24m	0.72m
SSF	5.67m	6.28m	4.03m	2.24m	0.72m
WSF	5.68m	6.29m	4.04m	2.24m	0.72m
ESPRIT	5.86m	6.34m	3.84m	2.09m	0.67m

Table A.8: Mean depth errors for F-smoothed R-estimation, MDL signal enumeration and coherent noise correction performed on data set 3

Methods	SNR				
	-5	0	5	10	20
Bartlett Peaks	11.04m	9.56m	8.40m	7.61m	7.35m
Bartlett Mean Amp	2.11m	2.34m	2.62m	2.73m	2.82m
Bartlett Max Amp	10.86m	9.22m	7.79m	6.27m	5.38m
Capon Peaks	11.58m	9.44m	7.53m	6.51m	6.16m
Capon Mean Amp	2.46m	1.50m	1.31m	1.03m	0.77m
Capon Max Amp	10.53m	3.75m	3.03m	1.74m	0.86m
MUSIC Peaks	11.22m	9.43m	7.32m	6.42m	6.08m
MUSIC Mean Amp	3.16m	2.24m	1.51m	1.40m	1.23m
MUSIC Max Amp	5.73m	3.48m	2.08m	1.51m	0.98m
Root-MUSIC	9.87m	7.69m	4.57m	2.78m	1.31m
SSF	9.87m	7.69m	4.57m	2.78m	1.31m
WSF	9.88m	7.69m	4.59m	2.77m	1.35m
ESPRIT	11.09m	7.99m	4.33m	2.65m	1.26m

Table A.9: Mean depth errors for F-smoothed R-estimation, KN signal enumeration and coherent noise correction performed on data set 3

Methods	SNR				
	-5	0	5	10	20
Bartlett Peaks	6.56m	8.86m	8.11m	8.25m	10.90m
Bartlett Mean Amp	2.73m	3.14m	3.38m	3.55m	3.64m
Bartlett Max Amp	11.57m	10.23m	8.48m	7.63m	6.95m
Capon Peaks	10.31m	11.55m	9.11m	7.93m	7.75m
Capon Mean Amp	3.29m	2.78m	2.14m	1.83m	0.86m
Capon Max Amp	12.54m	10.08m	6.90m	4.67m	1.40m
MUSIC Peaks	6.55m	8.67m	7.61m	6.68m	7.01m
MUSIC Mean Amp	5.78m	3.28m	2.05m	1.58m	1.08m
MUSIC Max Amp	6.37m	3.96m	2.50m	1.68m	0.93m
Root-MUSIC	5.45m	7.02m	5.37m	3.66m	3.60m
SSF	5.45m	7.02m	5.36m	3.66m	3.93m
WSF	5.45m	7.02m	5.36m	3.66m	3.93m
ESPRIT	5.31m	6.71m	4.72m	3.32m	4.01m

Table A.10: Mean depth errors for F-smoothed R-estimation, AIC signal enumeration and coherent noise correction performed on data set 4

Methods	SNR				
	-5	0	5	10	20
Bartlett Peaks	8.00m	9.47m	8.31m	8.42m	10.95m
Bartlett Mean Amp	2.67m	3.11m	3.43m	3.57m	3.64m
Bartlett Max Amp	11.93m	10.18m	8.72m	7.59m	6.86m
Capon Peaks	11.51m	11.86m	9.47m	7.97m	7.80m
Capon Mean Amp	3.67m	2.77m	2.05m	1.60m	0.89m
Capon Max Amp	12.72m	9.67m	6.60m	4.55m	1.62m
MUSIC Peaks	7.93m	9.30m	7.65m	6.66m	7.02m
MUSIC Mean Amp	5.13m	3.00m	2.02m	1.49m	1.14m
MUSIC Max Amp	6.07m	3.82m	2.62m	1.67m	0.94m
Root-MUSIC	6.94m	7.71m	5.38m	3.77m	3.67m
SSF	6.93m	7.72m	5.36m	3.76m	3.95m
WSF	6.93m	7.72m	5.36m	3.76m	3.96m
ESPRIT	6.95m	7.52m	4.68m	3.43m	4.05m

Table A.11: Mean depth errors for F-smoothed R-estimation, MDL signal enumeration and coherent noise correction performed on data set 4

Methods	SNR				
	-5	0	5	10	20
Bartlett Peaks	12.29m	10.82m	9.75m	9.36m	8.99m
Bartlett Mean Amp	2.74m	3.13m	3.44m	3.56m	3.64m
Bartlett Max Amp	12.52m	10.00m	8.66m	7.87m	6.60m
Capon Peaks	14.79m	13.32m	10.06m	8.31m	8.16m
Capon Mean Amp	3.23m	3.51m	2.56m	1.68m	1.05m
Capon Max Amp	12.46m	11.59m	8.49m	4.57m	1.78m
MUSIC Peaks	12.21m	10.19m	7.98m	7.01m	6.45m
MUSIC Mean Amp	3.01m	1.99m	1.74m	1.48m	1.47m
MUSIC Max Amp	6.50m	4.10m	2.69m	2.08m	1.64m
Root-MUSIC	11.10m	8.78m	5.82m	4.09m	2.44m
SSF	11.11m	8.79m	5.80m	4.11m	2.42m
WSF	11.12m	8.80m	5.81m	4.13m	2.44m
ESPRIT	11.78m	8.61m	5.02m	3.41m	2.27m

Table A.12: Mean depth errors for F-smoothed R-estimation, KN signal enumeration and coherent noise correction performed on data set 4

Methods	SNR				
	-5	0	5	10	20
Bartlett Peaks	0.63m	0.98m	1.62m	2.84m	5.60m
Bartlett Mean Amp	4.40m	3.77m	3.40m	3.20m	3.06m
Bartlett Max Amp	1.28m	1.18m	1.07m	1.06m	1.08m
Capon Peaks	0.55m	0.82m	1.45m	2.74m	5.43m
Capon Mean Amp	4.98m	4.14m	3.37m	2.83m	2.35m
Capon Max Amp	1.15m	0.81m	0.56m	0.50m	0.53m
MUSIC Peaks	0.53m	0.80m	1.38m	2.61m	5.39m
MUSIC Mean Amp	5.36m	3.92m	2.72m	2.00m	1.81m
MUSIC Max Amp	1.38m	1.18m	0.49m	0.52m	0.49m
Root-MUSIC	0.35m	0.47m	0.71m	1.17m	2.57m
SSF	0.35m	0.47m	0.71m	1.16m	2.53m
WSF	0.35m	0.47m	0.71m	1.16m	2.55m
ESPRIT	0.36m	0.46m	0.68m	1.08m	2.33m

Table A.13: Mean depth errors for FB-smoothed R-estimation, AIC signal enumeration and structured noise correction performed on data set 5



Methods	SNR				
	-5	0	5	10	20
Bartlett Peaks	0.80m	1.13m	1.96m	3.35m	6.33m
Bartlett Mean Amp	4.39m	3.75m	3.39m	3.19m	3.06m
Bartlett Max Amp	1.63m	1.24m	1.08m	1.08m	1.07m
Capon Peaks	0.71m	0.96m	1.72m	3.22m	5.98m
Capon Mean Amp	4.97m	4.11m	3.36m	2.82m	2.35m
Capon Max Amp	1.36m	0.98m	0.56m	0.48m	0.52m
MUSIC Peaks	0.67m	0.96m	1.72m	3.16m	6.06m
MUSIC Mean Amp	4.74m	3.69m	2.65m	1.92m	1.81m
MUSIC Max Amp	1.39m	0.97m	0.63m	0.44m	0.51m
Root-MUSIC	0.47m	0.57m	0.87m	1.41m	3.08m
SSF	0.47m	0.57m	0.87m	1.39m	3.03m
WSF	0.47m	0.57m	0.87m	1.39m	3.05m
ESPRIT	0.48m	0.56m	0.82m	1.28m	2.78m

Table A.14: Mean depth errors for FB-smoothed R-estimation, MDL signal enumeration and structured noise correction performed on data set 5

Methods	SNR				
	-5	0	5	10	20
Bartlett Peaks	2.33m	2.41m	3.25m	4.74m	7.40m
Bartlett Mean Amp	4.42m	3.77m	3.37m	3.19m	3.06m
Bartlett Max Amp	1.49m	1.26m	1.05m	1.07m	1.07m
Capon Peaks	2.65m	2.25m	3.13m	4.67m	6.71m
Capon Mean Amp	5.02m	4.15m	3.40m	2.91m	2.37m
Capon Max Amp	1.90m	1.20m	0.95m	0.89m	0.55m
MUSIC Peaks	2.25m	2.27m	3.11m	4.64m	7.10m
MUSIC Mean Amp	3.63m	2.86m	2.23m	1.94m	1.93m
MUSIC Max Amp	1.68m	1.02m	0.69m	0.57m	0.50m
Root-MUSIC	1.84m	1.59m	1.82m	2.41m	4.04m
SSF	1.84m	1.59m	1.81m	2.38m	3.97m
WSF	1.84m	1.59m	1.82m	2.40m	4.01m
ESPRIT	1.88m	1.58m	1.74m	2.23m	3.68m

Table A.15: Mean depth errors for FB-smoothed R-estimation, KN signal enumeration and structured noise correction performed on data set 5

Methods	SNR				
	-5	0	5	10	20
Bartlett Peaks	1.12m	2.03m	3.16m	4.29m	5.80m
Bartlett Mean Amp	4.40m	3.79m	3.43m	3.23m	3.09m
Bartlett Max Amp	1.63m	1.34m	1.06m	1.08m	1.08m
Capon Peaks	3.15m	4.20m	4.73m	5.34m	6.52m
Capon Mean Amp	5.00m	4.23m	3.57m	3.03m	2.57m
Capon Max Amp	2.77m	2.54m	2.09m	1.50m	0.98m
MUSIC Peaks	0.97m	1.81m	2.85m	3.89m	5.28m
MUSIC Mean Amp	4.10m	3.16m	2.65m	2.24m	1.97m
MUSIC Max Amp	1.76m	1.58m	0.63m	0.51m	0.69m
Root-MUSIC	0.80m	1.51m	2.30m	2.81m	3.34m
SSF	0.80m	1.51m	2.30m	2.79m	3.28m
WSF	0.80m	1.51m	2.30m	2.80m	3.29m
ESPRIT	0.81m	1.52m	2.34m	2.82m	3.24m

Table A.16: Mean depth errors for FB-smoothed R-estimation, AIC signal enumeration and structured noise correction performed on data set 6

Methods	SNR				
	-5	0	5	10	20
Bartlett Peaks	1.42m	2.41m	3.60m	4.65m	6.21m
Bartlett Mean Amp	4.41m	3.79m	3.43m	3.22m	3.09m
Bartlett Max Amp	1.43m	1.21m	1.08m	1.08m	1.07m
Capon Peaks	3.74m	4.42m	5.04m	5.60m	6.75m
Capon Mean Amp	5.03m	4.28m	3.52m	2.96m	2.60m
Capon Max Amp	3.14m	2.68m	2.10m	1.20m	0.93m
MUSIC Peaks	1.28m	2.16m	3.28m	4.22m	5.62m
MUSIC Mean Amp	3.87m	3.07m	2.63m	2.23m	2.00m
MUSIC Max Amp	1.59m	1.24m	0.56m	0.54m	0.76m
Root-MUSIC	1.08m	1.82m	2.61m	2.97m	3.57m
SSF	1.08m	1.82m	2.60m	2.94m	3.51m
WSF	1.08m	1.82m	2.60m	2.95m	3.52m
ESPRIT	1.10m	1.84m	2.64m	2.93m	3.45m

Table A.17: Mean depth errors for FB-smoothed R-estimation, MDL signal enumeration and structured noise correction performed on data set 6

Methods	SNR				
	-5	0	5	10	20
Bartlett Peaks	3.55m	3.89m	4.51m	5.28m	6.39m
Bartlett Mean Amp	4.41m	3.80m	3.43m	3.22m	3.09m
Bartlett Max Amp	1.52m	1.28m	1.15m	1.06m	1.07m
Capon Peaks	6.02m	5.59m	5.65m	6.02m	6.84m
Capon Mean Amp	5.06m	4.28m	3.53m	3.05m	2.57m
Capon Max Amp	3.33m	2.71m	2.32m	1.66m	0.98m
MUSIC Peaks	3.39m	3.65m	4.18m	4.79m	5.79m
MUSIC Mean Amp	3.80m	3.06m	2.51m	2.23m	2.07m
MUSIC Max Amp	2.09m	1.20m	0.73m	0.67m	0.71m
Root-MUSIC	3.03m	3.13m	3.28m	3.38m	3.75m
SSF	3.03m	3.12m	3.27m	3.35m	3.66m
WSF	3.03m	3.12m	3.28m	3.37m	3.70m
ESPRIT	3.07m	3.13m	3.29m	3.30m	3.60m

Table A.18: Mean depth errors for FB-smoothed R-estimation, KN signal enumeration and structured noise correction performed on data set 6

Methods	SNR				
	-5	0	5	10	20
Bartlett Peaks	10.29m	13.60m	18.19m	24.58m	31.63m
Bartlett Mean Amp	16.86m	14.25m	13.25m	12.91m	12.75m
Bartlett Max Amp	11.64m	11.68m	11.08m	11.11m	11.13m
Capon Peaks	9.13m	11.82m	16.37m	23.03m	30.05m
Capon Mean Amp	18.04m	13.45m	10.54m	9.13m	8.15m
Capon Max Amp	5.98m	5.41m	5.15m	5.22m	5.31m
MUSIC Peaks	9.71m	12.35m	17.10m	24.97m	33.84m
MUSIC Mean Amp	9.16m	7.73m	6.96m	6.93m	7.74m
MUSIC Max Amp	6.17m	5.87m	6.65m	6.87m	7.49m
Root-MUSIC	7.81m	10.48m	15.09m	21.93m	31.36m
SSF	7.81m	10.47m	15.06m	21.84m	31.23m
WSF	7.81m	10.47m	15.06m	21.85m	31.29m
ESPRIT	7.84m	10.22m	14.69m	21.11m	30.84m

Table A.19: Mean depth errors for FB-smoothed R-estimation, AIC signal enumeration and structured noise correction performed on data set 7

Methods	SNR				
	-5	0	5	10	20
Bartlett Peaks	11.32m	14.65m	19.55m	26.17m	32.59m
Bartlett Mean Amp	16.79m	14.28m	13.26m	12.91m	12.75m
Bartlett Max Amp	11.60m	11.36m	11.33m	11.18m	11.17m
Capon Peaks	10.12m	12.93m	17.90m	24.38m	30.57m
Capon Mean Amp	17.99m	13.46m	10.56m	9.21m	8.13m
Capon Max Amp	6.00m	5.37m	5.34m	5.38m	5.27m
MUSIC Peaks	10.77m	13.44m	18.68m	26.78m	35.08m
MUSIC Mean Amp	9.45m	7.99m	6.91m	7.08m	7.26m
MUSIC Max Amp	6.52m	6.15m	6.56m	7.00m	7.35m
Root-MUSIC	8.76m	11.50m	16.61m	23.78m	32.99m
SSF	8.75m	11.50m	16.58m	23.76m	32.93m
WSF	8.75m	11.51m	16.59m	23.77m	32.97m
ESPRIT	8.64m	11.30m	16.17m	23.05m	32.53m

Table A.20: Mean depth errors for FB-smoothed R-estimation, MDL signal enumeration and structured noise correction performed on data set 7

Methods	SNR				
	-5	0	5	10	20
Bartlett Peaks	16.27m	19.50m	24.97m	29.63m	33.84m
Bartlett Mean Amp	16.69m	14.26m	13.27m	12.90m	12.75m
Bartlett Max Amp	11.56m	11.30m	11.19m	11.28m	11.21m
Capon Peaks	15.47m	17.50m	21.82m	27.11m	31.23m
Capon Mean Amp	18.02m	13.62m	10.95m	9.19m	8.24m
Capon Max Amp	7.33m	5.63m	6.38m	5.76m	5.94m
MUSIC Peaks	15.86m	18.64m	24.93m	30.95m	36.47m
MUSIC Mean Amp	10.59m	8.37m	7.16m	7.26m	7.34m
MUSIC Max Amp	6.88m	6.00m	6.67m	6.72m	6.62m
Root-MUSIC	13.65m	16.42m	22.42m	28.25m	35.22m
SSF	13.65m	16.39m	22.34m	28.18m	35.18m
WSF	13.66m	16.40m	22.41m	28.23m	35.48m
ESPRIT	13.93m	16.48m	21.77m	27.55m	34.90m

Table A.21: Mean depth errors for FB-smoothed R-estimation, KN signal enumeration and structured noise correction performed on data set 7

Methods	SNR				
	-5	0	5	10	20
Bartlett Peaks	11.42m	15.39m	20.10m	25.15m	30.05m
Bartlett Mean Amp	16.75m	14.15m	13.11m	12.74m	12.60m
Bartlett Max Amp	12.03m	11.69m	11.45m	11.22m	11.26m
Capon Peaks	13.89m	17.29m	19.88m	23.51m	28.31m
Capon Mean Amp	19.09m	14.61m	11.82m	10.15m	9.40m
Capon Max Amp	12.76m	10.21m	9.52m	8.75m	8.30m
MUSIC Peaks	11.08m	14.14m	18.53m	24.04m	30.04m
MUSIC Mean Amp	10.14m	8.98m	7.80m	7.65m	8.26m
MUSIC Max Amp	6.65m	6.42m	6.84m	7.65m	8.21m
Root-MUSIC	9.02m	12.54m	16.85m	21.81m	28.22m
SSF	9.01m	12.52m	16.84m	21.74m	28.04m
WSF	9.01m	12.52m	16.84m	21.80m	28.10m
ESPRIT	8.98m	12.43m	16.78m	21.31m	27.71m

Table A.22: Mean depth errors for FB-smoothed R-estimation, AIC signal enumeration and structured noise correction performed on data set 8

Methods	SNR				
	-5	0	5	10	20
Bartlett Peaks	12.98m	16.68m	21.53m	26.07m	30.48m
Bartlett Mean Amp	16.78m	14.13m	13.12m	12.75m	12.60m
Bartlett Max Amp	11.95m	11.52m	11.22m	11.37m	11.32m
Capon Peaks	14.84m	18.13m	21.25m	24.52m	28.64m
Capon Mean Amp	19.00m	14.35m	11.82m	10.10m	9.21m
Capon Max Amp	10.99m	10.98m	9.57m	8.46m	7.73m
MUSIC Peaks	12.26m	15.45m	20.01m	25.03m	30.67m
MUSIC Mean Amp	10.46m	8.93m	7.85m	7.74m	8.11m
MUSIC Max Amp	6.73m	6.36m	6.85m	7.68m	8.06m
Root-MUSIC	10.50m	13.64m	18.36m	22.88m	29.23m
SSF	10.49m	13.64m	18.34m	22.82m	29.18m
WSF	10.49m	13.65m	18.37m	22.88m	29.28m
ESPRIT	10.46m	13.60m	18.06m	22.39m	28.73m

Table A.23: Mean depth errors for FB-smoothed R-estimation, MDL signal enumeration and structured noise correction performed on data set 8

Methods	SNR				
	-5	0	5	10	20
Bartlett Peaks	18.67m	20.96m	24.92m	27.76m	30.45m
Bartlett Mean Amp	16.69m	14.13m	13.09m	12.76m	12.60m
Bartlett Max Amp	11.88m	11.45m	11.33m	11.41m	11.27m
Capon Peaks	21.90m	21.80m	23.28m	25.97m	28.75m
Capon Mean Amp	18.80m	14.67m	11.93m	10.24m	9.47m
Capon Max Amp	14.04m	11.21m	10.18m	8.56m	8.02m
MUSIC Peaks	17.94m	19.76m	23.12m	26.77m	30.44m
MUSIC Mean Amp	11.41m	8.94m	7.81m	7.83m	7.97m
MUSIC Max Amp	7.34m	6.26m	7.00m	7.74m	8.50m
Root-MUSIC	15.97m	18.10m	21.42m	24.90m	29.22m
SSF	15.94m	18.09m	21.42m	24.82m	29.15m
WSF	15.92m	18.13m	21.49m	24.93m	29.28m
ESPRIT	16.44m	18.10m	21.19m	24.47m	28.78m

Table A.24: Mean depth errors for FB-smoothed R-estimation, KN signal enumeration and structured noise correction performed on data set 8

## Appendix B

# Full Sounding Density Results

Methods	SNR				
	-5	0	5	10	20
Bartlett Peaks	1287	1879	2463	3041	3816
Bartlett Mean Amp	210	210	210	210	210
Bartlett Max Amp	210	210	210	210	210
Capon Peaks	1284	1876	2459	3035	3812
Capon Mean Amp	210	210	210	210	210
Capon Max Amp	210	210	210	210	210
MUSIC Peaks	1287	1878	2461	3037	3815
MUSIC Mean Amp	210	207	210	210	210
MUSIC Max Amp	210	210	210	210	210
Root-MUSIC	1286	1878	2460	3036	3815
SSF	1286	1878	2460	3036	3815
WSF	1286	1878	2460	3036	3815
ESPRIT	1286	1878	2460	3036	3815

Table B.1: Number of soundings for F-smoothed R-estimation, AIC signal enumeration and coherent noise correction performed on data set 1

Methods	SNR				
	-5	0	5	10	20
Bartlett Peaks	1404	2006	2567	3163	3830
Bartlett Mean Amp	210	210	210	210	210
Bartlett Max Amp	210	210	210	210	210
Capon Peaks	1403	2002	2563	3143	3813
Capon Mean Amp	210	210	210	210	210
Capon Max Amp	210	210	210	210	210
MUSIC Peaks	1405	2004	2564	3149	3814
MUSIC Mean Amp	210	210	210	210	210
MUSIC Max Amp	210	210	210	210	210
Root-MUSIC	1402	2003	2564	3145	3813
SSF	1402	2003	2564	3145	3813
WSF	1402	2003	2564	3145	3813
ESPRIT	1401	2003	2564	3145	3813

Table B.2: Number of soundings for F-smoothed R-estimation, MDL signal enumeration and coherent noise correction performed on data set 1

Methods	SNR				
	-5	0	5	10	20
Bartlett Peaks	1944	2525	3251	3759	4114
Bartlett Mean Amp	210	210	210	210	210
Bartlett Max Amp	210	210	210	210	210
Capon Peaks	1914	2449	2707	3556	3927
Capon Mean Amp	210	210	210	210	210
Capon Max Amp	210	210	210	210	210
MUSIC Peaks	1921	2467	3096	3564	3926
MUSIC Mean Amp	210	210	210	210	210
MUSIC Max Amp	210	210	210	210	210
Root-MUSIC	1886	2435	3051	3543	3918
SSF	1886	2435	3051	3543	3918
WSF	1886	2436	3050	3543	3920
ESPRIT	1884	2432	3049	3542	3922

Table B.3: Number of soundings for F-smoothed R-estimation, KN signal enumeration and coherent noise correction performed on data set 1



Methods	SNR				
	-5	0	5	10	20
Bartlett Peaks	1373	1867	2445	3072	4015
Bartlett Mean Amp	210	210	210	210	210
Bartlett Max Amp	210	210	210	210	210
Capon Peaks	1064	1544	1914	2328	3214
Capon Mean Amp	210	210	210	210	210
Capon Max Amp	210	210	210	210	210
MUSIC Peaks	1374	1843	2340	2876	3745
MUSIC Mean Amp	210	210	210	210	210
MUSIC Max Amp	210	210	210	210	210
Root-MUSIC	1374	1842	2343	2909	3823
SSF	1374	1842	2344	2911	3822
WSF	1374	1842	2344	2910	3820
ESPRIT	1374	1848	2346	2897	3786

Table B.4: Number of soundings for F-smoothed R-estimation, AIC signal enumeration and coherent noise correction performed on data set 2

Methods	SNR				
	-5	0	5	10	20
Bartlett Peaks	1463	1999	2574	3139	4000
Bartlett Mean Amp	210	210	210	210	210
Bartlett Max Amp	210	210	210	210	210
Capon Peaks	1152	1659	2005	2415	3166
Capon Mean Amp	210	210	210	210	210
Capon Max Amp	210	210	210	210	210
MUSIC Peaks	1461	1973	2437	2923	3703
MUSIC Mean Amp	210	210	210	210	210
MUSIC Max Amp	210	210	210	210	210
Root-MUSIC	1460	1971	2449	2952	3786
SSF	1460	1971	2452	2953	3781
WSF	1460	1971	2452	2953	3782
ESPRIT	1460	1977	2449	2941	3758

Table B.5: Number of soundings for F-smoothed R-estimation, MDL signal enumeration and coherent noise correction performed on data set 2

Methods	SNR				
	-5	0	5	10	20
Bartlett Peaks	1936	2428	3040	3341	3761
Bartlett Mean Amp	210	210	210	210	210
Bartlett Max Amp	210	210	210	210	210
Capon Peaks	1653	1994	2238	2579	2872
Capon Mean Amp	210	210	210	210	210
Capon Max Amp	210	210	210	210	210
MUSIC Peaks	1952	2311	2774	3048	3499
MUSIC Mean Amp	210	210	210	210	210
MUSIC Max Amp	210	210	210	210	210
Root-MUSIC	1904	2295	2773	3065	3521
SSF	1904	2296	2772	3063	3520
WSF	1904	2295	2773	3062	3520
ESPRIT	1905	2302	2760	3049	3502

Table B.6: Number of soundings for F-smoothed R-estimation, KN signal enumeration and coherent noise correction performed on data set 2

Methods	SNR				
	-5	0	5	10	20
Bartlett Peaks	2079	4487	5334	5336	5335
Bartlett Mean Amp	210	210	210	210	210
Bartlett Max Amp	210	210	210	210	210
Capon Peaks	2079	4481	5331	5333	5331
Capon Mean Amp	210	210	210	210	210
Capon Max Amp	210	210	210	210	210
MUSIC Peaks	2080	4487	5334	5334	5334
MUSIC Mean Amp	210	210	210	210	210
MUSIC Max Amp	210	210	210	210	210
Root-MUSIC	2080	4487	5334	5334	5334
SSF	2080	4487	5334	5334	5334
WSF	2080	4487	5334	5334	5334
ESPRIT	2080	4486	5334	5334	5334

Table B.7: Number of soundings for F-smoothed R-estimation, AIC signal enumeration and coherent noise correction performed on data set 3

Methods	SNR				
	-5	0	5	10	20
Bartlett Peaks	2502	4818	5341	5341	5342
Bartlett Mean Amp	210	210	210	210	210
Bartlett Max Amp	210	210	210	210	210
Capon Peaks	2496	4817	5333	5333	5333
Capon Mean Amp	210	210	210	210	210
Capon Max Amp	210	210	210	210	210
MUSIC Peaks	2501	4819	5335	5335	5335
MUSIC Mean Amp	210	210	210	210	210
MUSIC Max Amp	210	210	210	210	210
Root-MUSIC	2501	4819	5335	5335	5335
SSF	2501	4819	5335	5335	5335
WSF	2501	4819	5335	5335	5335
ESPRIT	2500	4819	5336	5335	5335

Table B.8: Number of soundings for F-smoothed R-estimation, MDL signal enumeration and coherent noise correction performed on data set 3

Methods	SNR				
	-5	0	5	10	20
Bartlett Peaks	3972	5286	5500	5528	5549
Bartlett Mean Amp	210	210	210	210	210
Bartlett Max Amp	210	210	210	210	210
Capon Peaks	3912	5257	5397	5204	5241
Capon Mean Amp	210	210	210	210	210
Capon Max Amp	210	210	210	210	210
MUSIC Peaks	3983	5268	5403	5401	5401
MUSIC Mean Amp	210	210	210	210	210
MUSIC Max Amp	210	210	210	210	210
Root-MUSIC	3962	5254	5395	5385	5390
SSF	3962	5254	5395	5386	5390
WSF	3962	5254	5395	5385	5392
ESPRIT	3931	5247	5394	5385	5391

Table B.9: Number of soundings for F-smoothed R-estimation, KN signal enumeration and coherent noise correction performed on data set 3

Methods	SNR				
	-5	0	5	10	20
Bartlett Peaks	2135	4382	5298	5397	5747
Bartlett Mean Amp	210	210	210	210	210
Bartlett Max Amp	210	210	210	210	210
Capon Peaks	1324	2896	3832	4030	4477
Capon Mean Amp	210	210	210	210	210
Capon Max Amp	210	210	210	210	210
MUSIC Peaks	2138	4390	5258	5267	5392
MUSIC Mean Amp	210	210	210	210	210
MUSIC Max Amp	210	210	210	210	210
Root-MUSIC	2137	4393	5271	5290	5524
SSF	2137	4393	5273	5292	5528
WSF	2137	4393	5273	5292	5529
ESPRIT	2137	4386	5269	5290	5535

Table B.10: Number of soundings for F-smoothed R-estimation, AIC signal enumeration and coherent noise correction performed on data set 4

Methods	SNR				
	-5	0	5	10	20
Bartlett Peaks	2606	4622	5277	5415	5728
Bartlett Mean Amp	210	210	210	210	210
Bartlett Max Amp	210	210	210	210	210
Capon Peaks	1604	3045	3877	4088	4497
Capon Mean Amp	210	210	210	210	210
Capon Max Amp	210	210	210	210	210
MUSIC Peaks	2614	4626	5230	5267	5397
MUSIC Mean Amp	210	210	210	210	210
MUSIC Max Amp	210	210	210	210	210
Root-MUSIC	2615	4625	5240	5296	5520
SSF	2615	4626	5242	5301	5526
WSF	2615	4626	5242	5301	5525
ESPRIT	2615	4613	5239	5300	5528

Table B.11: Number of soundings for F-smoothed R-estimation, MDL signal enumeration and coherent noise correction performed on data set 4

Methods	SNR				
	-5	0	5	10	20
Bartlett Peaks	3724	5097	5439	5524	5531
Bartlett Mean Amp	210	210	210	210	210
Bartlett Max Amp	210	210	210	210	210
Capon Peaks	2521	3336	4005	4221	4063
Capon Mean Amp	210	210	210	210	210
Capon Max Amp	210	210	210	210	210
MUSIC Peaks	3742	5053	5267	5301	5287
MUSIC Mean Amp	210	210	210	210	210
MUSIC Max Amp	210	210	210	210	210
Root-MUSIC	3717	5063	5289	5325	5297
SSF	3718	5066	5292	5334	5299
WSF	3718	5066	5290	5333	5299
ESPRIT	3684	5034	5293	5332	5305

Table B.12: Number of soundings for F-smoothed R-estimation, KN signal enumeration and coherent noise correction performed on data set 4

Methods	SNR				
	-5	0	5	10	20
Bartlett Peaks	1450	2300	3212	4457	7773
Bartlett Mean Amp	210	210	210	210	210
Bartlett Max Amp	210	210	210	210	210
Capon Peaks	1449	2284	3155	4282	7206
Capon Mean Amp	210	210	210	210	210
Capon Max Amp	210	210	210	210	210
MUSIC Peaks	1454	2307	3220	4457	7838
MUSIC Mean Amp	210	210	210	210	210
MUSIC Max Amp	210	210	210	210	210
Root-MUSIC	1454	2307	3226	4509	8084
SSF	1454	2307	3226	4509	8083
WSF	1454	2307	3226	4509	8083
ESPRIT	1454	2307	3226	4511	8094

Table B.13: Number of soundings for FB-smoothed R-estimation, AIC signal enumeration and structured noise correction performed on data set 5

Methods	SNR				
	-5	0	5	10	20
Bartlett Peaks	1639	2492	3460	4865	8464
Bartlett Mean Amp	210	210	210	210	210
Bartlett Max Amp	210	210	210	210	210
Capon Peaks	1637	2466	3370	4644	7716
Capon Mean Amp	210	210	210	210	210
Capon Max Amp	210	210	210	210	210
MUSIC Peaks	1647	2502	3464	4897	8536
MUSIC Mean Amp	210	210	210	210	210
MUSIC Max Amp	210	210	210	210	210
Root-MUSIC	1646	2501	3476	4962	8867
SSF	1646	2501	3476	4962	8866
WSF	1646	2501	3476	4962	8867
ESPRIT	1646	2501	3477	4966	8879

Table B.14: Number of soundings for FB-smoothed R-estimation, MDL signal enumeration and structured noise correction performed on data set 5

Methods	SNR				
	-5	0	5	10	20
Bartlett Peaks	2438	3314	4433	6165	9916
Bartlett Mean Amp	210	210	210	210	210
Bartlett Max Amp	210	210	210	210	210
Capon Peaks	2423	3237	4253	5470	8776
Capon Mean Amp	210	210	210	210	210
Capon Max Amp	210	210	210	210	210
MUSIC Peaks	2459	3342	4447	6180	9992
MUSIC Mean Amp	210	210	210	210	210
MUSIC Max Amp	210	210	210	210	210
Root-MUSIC	2406	3290	4450	6299	10499
SSF	2406	3290	4450	6300	10502
WSF	2405	3290	4450	6298	10504
ESPRIT	2406	3293	4457	6303	10525

Table B.15: Number of soundings for FB-smoothed R-estimation, KN signal enumeration and structured noise correction performed on data set 5

Methods	SNR				
	-5	0	5	10	20
Bartlett Peaks	1535	2444	3457	4640	6602
Bartlett Mean Amp	210	210	210	210	210
Bartlett Max Amp	210	210	210	210	210
Capon Peaks	1268	2166	3096	4151	5881
Capon Mean Amp	210	210	210	210	210
Capon Max Amp	210	210	210	210	210
MUSIC Peaks	1538	2456	3398	4514	6375
MUSIC Mean Amp	210	210	210	210	210
MUSIC Max Amp	210	210	210	210	210
Root-MUSIC	1536	2457	3425	4616	6685
SSF	1536	2457	3425	4616	6689
WSF	1536	2457	3424	4616	6690
ESPRIT	1536	2459	3440	4639	6744

Table B.16: Number of soundings for FB-smoothed R-estimation, AIC signal enumeration and structured noise correction performed on data set 6

Methods	SNR				
	-5	0	5	10	20
Bartlett Peaks	1771	2715	3787	5001	6979
Bartlett Mean Amp	210	210	210	210	210
Bartlett Max Amp	210	210	210	210	210
Capon Peaks	1497	2392	3370	4459	6171
Capon Mean Amp	210	210	210	210	210
Capon Max Amp	210	210	210	210	210
MUSIC Peaks	1775	2703	3697	4812	6697
MUSIC Mean Amp	210	210	210	210	210
MUSIC Max Amp	210	210	210	210	210
Root-MUSIC	1774	2704	3740	4963	7056
SSF	1774	2705	3741	4961	7063
WSF	1774	2705	3741	4962	7062
ESPRIT	1775	2709	3758	4996	7131

Table B.17: Number of soundings for FB-smoothed R-estimation, MDL signal enumeration and structured noise correction performed on data set 6

Methods	SNR				
	-5	0	5	10	20
Bartlett Peaks	2693	3524	4457	5540	6914
Bartlett Mean Amp	210	210	210	210	210
Bartlett Max Amp	210	210	210	210	210
Capon Peaks	2284	3184	4016	4937	6020
Capon Mean Amp	210	210	210	210	210
Capon Max Amp	210	210	210	210	210
MUSIC Peaks	2703	3478	4325	5278	6648
MUSIC Mean Amp	210	210	210	210	210
MUSIC Max Amp	210	210	210	210	210
Root-MUSIC	2641	3456	4398	5496	7025
SSF	2641	3456	4397	5496	7026
WSF	2641	3453	4399	5497	7028
ESPRIT	2647	3458	4420	5532	7089

Table B.18: Number of soundings for FB-smoothed R-estimation, KN signal enumeration and structured noise correction performed on data set 6

Methods	SNR				
	-5	0	5	10	20
Bartlett Peaks	1510	2641	3785	5015	6454
Bartlett Mean Amp	210	210	210	210	210
Bartlett Max Amp	210	210	210	210	210
Capon Peaks	1517	2644	3817	5086	6472
Capon Mean Amp	210	210	210	210	210
Capon Max Amp	210	210	210	210	210
MUSIC Peaks	1524	2661	3870	5272	7114
MUSIC Mean Amp	210	210	210	210	210
MUSIC Max Amp	210	210	210	210	210
Root-MUSIC	1537	2694	4032	5892	9118
SSF	1537	2694	4032	5898	9144
WSF	1537	2694	4033	5897	9143
ESPRIT	1537	2695	4041	5915	9316

Table B.19: Number of soundings for FB-smoothed R-estimation, AIC signal enumeration and structured noise correction performed on data set 7



Methods	SNR				
	-5	0	5	10	20
Bartlett Peaks	1717	2836	4057	5211	6628
Bartlett Mean Amp	210	210	210	210	210
Bartlett Max Amp	210	210	210	210	210
Capon Peaks	1716	2828	4074	5314	6565
Capon Mean Amp	210	210	210	210	210
Capon Max Amp	210	210	210	210	210
MUSIC Peaks	1736	2861	4162	5564	7375
MUSIC Mean Amp	210	210	210	210	210
MUSIC Max Amp	210	210	210	210	210
Root-MUSIC	1749	2893	4383	6348	9623
SSF	1749	2894	4387	6366	9655
WSF	1749	2894	4387	6365	9649
ESPRIT	1747	2898	4397	6409	9853

Table B.20: Number of soundings for FB-smoothed R-estimation, MDL signal enumeration and structured noise correction performed on data set 7

Methods	SNR				
	-5	0	5	10	20
Bartlett Peaks	2438	3563	4833	5844	6924
Bartlett Mean Amp	210	210	210	210	210
Bartlett Max Amp	210	210	210	210	210
Capon Peaks	2429	3575	4842	5808	6669
Capon Mean Amp	210	210	210	210	210
Capon Max Amp	210	210	210	210	210
MUSIC Peaks	2481	3655	5042	6310	7702
MUSIC Mean Amp	210	210	210	210	210
MUSIC Max Amp	210	210	210	210	210
Root-MUSIC	2472	3754	5542	7543	10407
SSF	2470	3754	5550	7589	10464
WSF	2470	3754	5553	7570	10459
ESPRIT	2458	3749	5565	7650	10743

Table B.21: Number of soundings for FB-smoothed R-estimation, KN signal enumeration and structured noise correction performed on data set 7

Methods	SNR				
	-5	0	5	10	20
Bartlett Peaks	1568	2669	3705	4612	5603
Bartlett Mean Amp	210	210	210	210	210
Bartlett Max Amp	210	210	210	210	210
Capon Peaks	1022	1844	2762	3831	4957
Capon Mean Amp	210	210	210	210	210
Capon Max Amp	210	210	210	210	210
MUSIC Peaks	1588	2680	3770	4751	5937
MUSIC Mean Amp	210	210	210	210	210
MUSIC Max Amp	210	210	210	210	210
Root-MUSIC	1600	2733	3933	5275	7151
SSF	1600	2732	3935	5289	7208
WSF	1600	2732	3935	5294	7207
ESPRIT	1600	2728	3946	5325	7266

Table B.22: Number of soundings for FB-smoothed R-estimation, AIC signal enumeration and structured noise correction performed on data set 8

Methods	SNR				
	-5	0	5	10	20
Bartlett Peaks	1765	2905	3887	4736	5743
Bartlett Mean Amp	210	210	210	210	210
Bartlett Max Amp	210	210	210	210	210
Capon Peaks	1144	2009	2971	3957	5136
Capon Mean Amp	210	210	210	210	210
Capon Max Amp	210	210	210	210	210
MUSIC Peaks	1779	2923	3968	4876	6026
MUSIC Mean Amp	210	210	210	210	210
MUSIC Max Amp	210	210	210	210	210
Root-MUSIC	1801	2965	4188	5463	7400
SSF	1801	2965	4193	5476	7467
WSF	1801	2966	4195	5475	7479
ESPRIT	1801	2979	4190	5502	7548

Table B.23: Number of soundings for FB-smoothed R-estimation, MDL signal enumeration and structured noise correction performed on data set 8

Methods	SNR				
	-5	0	5	10	20
Bartlett Peaks	2526	3508	4283	4992	5658
Bartlett Mean Amp	210	210	210	210	210
Bartlett Max Amp	210	210	210	210	210
Capon Peaks	1846	2585	3421	4178	5002
Capon Mean Amp	210	210	210	210	210
Capon Max Amp	210	210	210	210	210
MUSIC Peaks	2579	3565	4372	5139	5935
MUSIC Mean Amp	210	210	210	210	210
MUSIC Max Amp	210	210	210	210	210
Root-MUSIC	2596	3638	4710	5900	7267
SSF	2594	3637	4722	5922	7349
WSF	2591	3640	4722	5912	7335
ESPRIT	2581	3633	4744	5989	7475

Table B.24: Number of soundings for FB-smoothed R-estimation, KN signal enumeration and structured noise correction performed on data set 8

# References

- [Asada and Yabuki 2001] Akira Asada and Tetsuichiro Yabuki. Synthetic aperture technique applied to multi-beam echo sounder. *Earth Planets Space*, 53:321–326, 2001.
- [Barabell 1983] A. J. Barabell. Improving the resolution performance of eigenstructure-based direction-finding algorithms. In *Proc. ICASSP*, pages 336–339, 1983.
- [Bartlett 1948] M. S. Bartlett. Smoothing periodograms from time series with continuous spectra. *Nature*, 161:686–687, 1948.
- [Bienvenu and Kopp 1980] G. Bienvenu and L. Kopp. Adaptivity to background noise spatial coherence for high resolution passive methods. In *Int. Conf. on Acoustics, speech and signal processing*, pages 307–310, 1980.
- [Bienvenu and Kopp 1983] Georges Bienvenu and Laurent Kopp. Optimality of high resolution array processing using the eigensystem approach. *IEEE Transactions on acoustics, speech, and signal processing*, 31:1235–1248, October 1983.
- [Birney *et al.* 2008] Kristi Birney, Amber Griffin, Jonathan Gwiazda, Johnny Kefauver, Takehiko Nagai, and Douglas Varchol. *Potential Deep-Sea Mining of Seafloor Massive Sulfides: A Case Study in Papua New Guinea*. Technical report, University of California at Santa Barbara, 2008.
- [Brown *et al.* 2010] Craig J. Brown, Brian J. Todd, Vladimir E. Kostylev, and Richard A. Pickrill. Image-based classification of multibeam sonar backscatter data for objective surficial sediment mapping of Georges Bank, Canada. *Continental Shelf Research*, 2010.
- [Calder and Mayer 2001] B. R. Calder and L. A. Mayer. Robust automatic multi-beam bathymetric processing. In *U.S. Hydrographic Conference*, pages 21–24, 2001.
- [Calder and Mayer 2003] B. R. Calder and L. A. Mayer. Automatic processing of high-rate, high-density multibeam echosounder data. *Geochemistry Geophysics Geosystems*, 4(6):1, 2003.
- [Calder 2003] B. R. Calder. Automatic statistical processing of multibeam echosounder data. *International Hydrographic Review*, 4(1):53–68, 2003.
- [Canepa *et al.* 2003] Gaetano Canepa, Oddbjorn Bergem, and Nicholas G. Pace. A new algorithm for automatic processing of bathymetric data. *IEEE Journal of oceanic engineering*, 28(1):62–77, January 2003.

- [Capon 1969] J. Capon. High-resolution frequency-wavenumber spectrum analysis. *Proceedings of the IEEE*, 57(8):1408–1418, 1969.
- [Caress *et al.* 2008] David W. Caress, Hans Thomas, William J. Kirkwood, Rob McEwen, Richard Henthorn, David A. Clague, Charles K. Paull, and Jenny Paduan. High-resolution multibeam, sidescan, and subbottom surveys using the MBARI AUV D. Allan B. In Jennifer R. Reynolds and H. Gary Greene, editors, *Marine Habitat Mapping Technology for Alaska*, chapter 4, pages 47–69. Alaska Sea Grant, 2008.
- [Cazenave *et al.* 2008] Pierre W. Cazenave, David O. Lambkin, and Justin K. Dix. Quantitative bedform analysis using decimetre resolution swath bathymetry. In *CARIS 2008*, 2008.
- [Chen and Gershman 2008] Haihua Chen and Alex B. Gershman. Robust adaptive beamforming for general-rank signal models using positive semi-definite covariance constraint. In *IEEE International Conference on Acoustics, Speech and Signal Processing*, pages 2341–2344, 2008.
- [Chrisofilakis *et al.* 2008] Vasilis N. Chrisofilakis, Panos Kostarakis, Antonis A. Alexandridis, Fotis Lazarakis, and Kostas Dangakis. Increasing direction-of-transmission resolution in digital time-delay beamformers. *International Journal of Electronics and Communications*, pages 49–56, 2008.
- [Church and Warren 2008] Robert A. Church and Daniel J. Warren. Sound methods: the necessity of high-resolution geophysical data for planning deepwater archaeological projects. *International Journal of Historical Archaeology*, 12:103–119, 2008.
- [de Moustier 1988] C. de Moustier. State of the art in swath bathymetry survey systems. *International Hydrographic Review*, 65(2):25–54, 1988.
- [de Paulis *et al.* 2009] R. de Paulis, C. Prati, F. Rocca, S. Scirpoli, and S. Tebaldini. Focusing synthetic aperture sonar (SAS) data with the omega-k technique. In *IGARSS 2009*, pages I/68–I/71, 2009.
- [Diederer 2009] André Diederer. <http://europe.theoil drum.com/node/5239>, May 2009.
- [Ellingson and Cazemier 2003] Steven W. Ellingson and Willem Cazemier. Efficient multibeam synthesis with interference nulling for large arrays. *IEEE Transactions on antennas and propagation*, 51(3):503–511, March 2003.
- [Elmore and Steed 2008] Paul A. Elmore and Chad A. Steed. *Algorithm design study for bathymetry fusion - review of current state-of-the-art and recommended design approach*. Technical report, Naval Research Laboratory, 2008.
- [Fonseca and Mayer 2007] Luciano Fonseca and Larry Mayer. Remote estimation of surficial seafloor properties through the application angular range analysis to multibeam sonar data. *Marine Geological Researches*, 8(2):119–126, 2007.
- [Geng and Zielinski 1999] Xueyi Geng and Adam Zielinski. Precise multibeam acoustic bathymetry. *Marine Geodesy*, 22:157–167, 1999.
- [Gough and Hayes 2008] P. T. Gough and M. Hayes. Ten key papers in synthetic aperture sonar. In *Acoustics 08 Paris*, pages 5305–5308, 2008.

- [Helene *et al.* 2009] Ondreas Helene, Cannat M., Fouquet Yves, Normand Alain, Sarradin Pierre-Marie, and Sarrazin Jozee. Recent volcanic events and the distribution of hydrothermal venting at the Lucky Strike hydrothermal field, Mid-Atlantic Ridge. *Geochemistry Geophysics Geosystems*, 10(2):1–18, 2009.
- [Hellequin *et al.* 2003] Laurent Hellequin, Jean-Marc Boucher, and Xavier Lurton. Processing of high-frequency multibeam echo sounder data for seafloor characterization. *IEEE Journal of oceanic engineering*, 28(1):1–12, January 2003.
- [Kammerer *et al.* 1998] E. Kammerer, J. E. Hughes Clarke, J. Locat, N. Doucet, and A. Godin. Monitoring temporal changes in seabed morphology and composition using multibeam sonars: a case study of the 1996 Saguenay River floods. In *Proceedings Canadian Hydrographic Conference*, pages 450–461, 1998.
- [Karoui *et al.* 2009] Imen Karoui, Ronan Fablet, Jean-Marc Boucher, and Jean-Marie Augustin. Seabed segmentation using optimized statistics of sonar textures. *IEEE Transactions on geoscience and remote sensing*, 47(6):1621–1631, June 2009.
- [Kotanchek and Dzielski 1996] M. E. Kotanchek and J. E. Dzielski. Subspace stability in high resolution direction finding and signal enumeration. In *Proceedings of the 1996 Symposium on Autonomous Underwater Vehicle Technology*, pages 192–199, 1996.
- [Krim and Viberg 1996] Hamid Krim and Mats Viberg. Two decades of array signal processing. *IEEE Signal Processing Magazine*, pages 67–94, July 1996.
- [Kritchman and Nadler 2008] Shira Kritchman and Boaz Nadler. Determining the number of components in a factor model from limited noisy data. *Chemometrics and Intelligent Laboratory Systems*, 94(1):19–32, 2008.
- [L-3 2000] L-3 Communications SeaBeam Instruments, 141 Washington Street East Walpole, MA 02032-1155. *Multibeam Sonar Theory of Operation*, 2000.
- [Li *et al.* 2005] Jian Li, Zhisong Wang, and Petre Stoica. *Robust Capon Beamforming*, pages 91–200. John Wiley Sons, Inc., 2005.
- [Lipton 2008] Ian Lipton. *Mineral Resource Estimate Solwara 1 Project Bismarck Sea Papua New Guinea*. Technical report, Golder Associates, 2008.
- [Magoon *et al.* 2009] Jonathan R. Pearson Magoon, Matthew A. Nelson, and Daniel D. Sternlicht. Frequency domain beamforming for a 3-d sediment volume imaging synthetic aperture sonar. In *Oceans 2009*, pages 1–4, 2009.
- [Mallace and Robertson 2007] Duncan Mallace and Paul Robertson. Alternative use of CUBE: how to fit a square peg in a round hole. In *US Hydro Conference 2007*, 2007.
- [Marks and Smith 2008] K. M. Marks and W. H. F. Smith. An uncertainty model for deep ocean single beam and multibeam echo sounder data. *Marine Geophysical Researches*, 29:239–250, 2008.

- [Marsh and Brown 2009] Ivor Marsh and Colin Brown. Neural network classification of multibeam backscatter and bathymetry data from Stanton Bank (Area IV). *Applied Acoustics*, 70:1269–1276, 2009.
- [Mayer 2006] L. A. Mayer. Frontiers in seafloor mapping and visualization. *Marine Geophysical Researches*, 27(1):7–17, 2006.
- [Mitchell 1996] Neil C. Mitchell. Processing and analysis of Simrad multibeam sonar data. *Marine Geophysical Researches*, 18:729–739, 1996.
- [Moses 2005] Randolph Moses. <http://www2.ece.ohio-state.edu/~randy/SAtext/>, 2005.
- [Nielsen 1991] Richard O. Nielsen. *Sonar Signal Processing*. Artech House Publishers, 1991.
- [Pan *et al.* 2009] Xiang Pan, Wen Xu, Jianlong Li, and Xianyi Gong. Combination of time reversal and synthetic aperture beamforming for active detection of small bottom objects in waveguide environments. *Applied Acoustics*, 70:1406–1411, 2009.
- [Pantartzis *et al.* 1993] D. Pantartzis, C. de Moustier, and D. Alexandrou. Application of high-resolution beamforming to multibeam swath bathymetry. In *OCEANS 93*, pages II/77 – II/82, 1993.
- [Pinto *et al.* 2004] Marc Pinto, Andrea Bellettini, Lian Sheng Wang, Peter Munk, Vincent Myers, and Lucie Pautet. A new synthetic aperture sonar design with multipath mitigation. In *AIP Conference Proceedings*, volume 728, pages 489–496, 2004.
- [Preston and Biffard 2007] Jon M. Preston and Ben R. Biffard. Acoustic classification with sounder echoes: isolating effects of the seabed on the echo. In *Proceedings of Underwater Acoustics Measurements: Technologies Results*, 2007.
- [Pujol *et al.* 2008] Gerard Llord Pujol, Christophe Sintès, and Xavier Lurton. Improving spatial resolution of interferometric bathymetry in multibeam echosounders. In *Acoustics 08 Paris*, 2008.
- [Pujol *et al.* 2010] Gerard Llord Pujol, Christophe Sintès, Thierry Chonavel, Didier Gueriot, and Rene Garello. Simulation on large scale of acoustic signals for array processing. In *Oceans 2010*, 2010.
- [Pujol 2007] Gerard Llord Pujol. *Improvement of the Spatial Resolution for Multibeam Echosounders*. PhD thesis, Université de Rennes I, 2007.
- [Ranade 2006] Govind Ranade. *Impact of bathymetric system advances on hydrography*. Technical report, National Institute of Oceanography, 2006.
- [Ronhovde *et al.* 1999] Are Ronhovde, Luren Yang, Torfinn Taxt, and Sverre Holm. High-resolution beamforming for multibeam echo sounders using raw EM3000 data. In *Oceans 1999*, volume 2, pages 923 – 930, 1999.
- [Ronhovde 1999] Are Ronhovde. *High Resolution Beamforming of Simrad EM3000 Bathymetric Multibeam Sonar data*. PhD thesis, University of Oslo, 1999.

- [Roy and Kailath 1989] R. Roy and T. Kailath. ESPRIT - estimation of signal parameters via rotational invariance techniques. *IEEE Transactions on acoustics, speech, and signal processing*, 37(7):984–995, July 1989.
- [Savini and Corselli 2010] A. Savini and C. Corselli. High-resolution bathymetry and acoustic geophysical data from Santa Maria di Leuca Cold Water coral province (Northern Ionian sea - Apulian continental slope). *Deep-Sea Research II*, 57:326–344, 2010.
- [Schmidt 1981] R. O. Schmidt. *A signal subspace approach to multiple emitter location and spectral estimation*. PhD thesis, Stanford University, 1981.
- [Stoica and Sharman 1990] P. Stoica and K. Sharman. A novel eigenanalysis method for direction estimation. *Proceedings of the IEEE*, pages 19–26, February 1990.
- [Tarlet *et al.* 2007] O. Tarlet, A. LouSSERT, and C. Sintes. Sonar images from well-known simulated raw data. In *IEEE Int. Conf. on Signal Processing and Communications*, pages 1423–1426, 2007.
- [Tian *et al.* 2009] Biao Tian, Haining Huang, and Yu Li. Direction of arrival estimation using nonlinear function of sum and difference beam. In *IEEE Youth Conference on Information, Computing and Telecommunication*, pages 311–314, 2009.
- [van Vossen *et al.* 2009] Robbert van Vossen, Lianke te Raa, and Gerrit Blacchiere. Acquisition concepts for MIMO sonar. In *Underwater Acoustic Measurements Proceedings*, 2009.
- [Viberg *et al.* 1991] M. Viberg, B. Ottersten, and T. Kailath. Detection and estimation in sensor arrays using weighted subspace fitting. *IEEE Transactions on signal processing*, 39:2436–2449, November 1991.
- [Waite 2002] A. D. Waite. *Sonar for Practising Engineers*. Wiley, 3 edition, 2002.
- [Ware *et al.* 1991] Colin Ware, William Knight, and David Wells. Memory intensive statistical algorithms for multibeam bathymetric data. *Computers and Geosciences*, 17(7):985–993, 1991.
- [Yang and Taxt 1997] Luren Yang and Torfinn Taxt. Multibeam sonar bottom detection using multiple subarrays. In *Oceans 1997*, volume 2, pages 932–938, 1997.
- [Yang *et al.* 2007] Fanlin Yang, Jiabiao Li, Fengyou Chu, and Ziyin Wu. Automatic detecting outliers in multibeam sonar based on density of points. In *Oceans 2007*, 2007.
- [Zhu and Sala-Diakanda 2007] Yanshen Zhu and Serge Sala-Diakanda. Integration of underwater sonar simulation with a geographical information system. In *Proceedings of the 2007 winter simulation conference*, pages 1378–1386, 2007.
- [Zhu *et al.* 2008] Yanshen Zhu, Maria Bull, and Haluk Akin. Information fusion in underwater sonar simulation. In *Proceedings of the 2008 winter simulation conference*, pages 1250–1258, 2008.